Electronic ISSN: 1309-0267

International Journal of Engineering & Applied Sciences

IJEAS

I J E A S

Volume 9, Issue 4
2017

Published by Akdeniz University

Honorary Editors

(in Alphabetical)

Editor in Chief:

Ömer Civalek – Akdeniz University *civalek@yahoo.com*

Associate Editors:

Asst. Prof. Ibrahim AYDOĞDU -Akdeniz University *aydogdu@akdeniz.edu.tr*

Asst. Prof. Sevil Köfteci -Akdeniz University *skofteci@akdeniz.edu.tr*

R.A. Kadir MERCAN -Akdeniz University *mercankadir@akdeniz.edu.tr*

Editorial Board

(The name listed below is not Alphabetical or any title scale)

Abstracting & Indexing

IJEAS provides unique **DOI** link to every paper published.

Editorial Scope

The journal presents its readers with broad coverage across some branches of engineering and science of the latest development and application of new solution algorithms, artificial intelligent techniques innovative numerical methods and/or solution techniques directed at the utilization of computational methods in solid and nano-scaled mechanics.

International Journal of Engineering & Applied Sciences (IJEAS) is an Open Access Journal

International Journal of Engineering & Applied Sciences (IJEAS) publish original contributions on the following topics:

Numerical Methods in Solid Mechanics

Nanomechanic and applications

Microelectromechanical systems (MEMS)

Vibration Problems in Engineering

Higher order elasticity (Strain gradient, couple stress, surface elasticity, nonlocal elasticity)

Applied Mathematics

CONTENTS

International Journal of Engineering & Applied Sciences (IJEAS)
Vol.9, Issue 4 (2017)1-16
http://dx.doi.org/10.24107/ijeas.335697
Int J Eng Appl Sci 9(4) (2017) 1-16

A User Friendly Software for Rigid Pavement Design

Aydın Kıcı [a], *Mesut Tığdemir* [b*]

Department of Civil Engineering, Faculty of Engineering, Suleyman Demirel University, Cunur, Isparta, Turkey
[*]*E-mail address*: mtigdemir.acd@yahoo.com

ORCID numbers of authors:
0000-0001-9741-4995[a], *0000-0002-5303-2722*[b]

Received date: August 2017
Accepted date: November 2017

Abstract

Concrete pavements as concrete road slab, appear as a strong alternative for flexible superstructures especially because of their low cost for maintenance and repair and the high performance they show under heavy axle loads. The design of these concrete road slabs is quite different from the traditional concrete and reinforced concrete structures' design. In the design for this kind of pavements, traffic conditions should be defined properly and considered an addition to the concrete and platform properties. There have been designing methods developed based on both experimental and mechanic foundations for concrete pavements. The most important ones of these methods are AASHTO (1993) and PCA (1984). In both design methods, it's significant to know the maximum deflections and maximum strains the vehicles' loads cause on the pavement. The calculation of this maximum deflections and maximum strains can be done via the finite element method or the closed formulas which have been developed by Westergaard. In this study, a user-friendly software has been developed based on AASHTO 1993, PCA 1984 design methods and Westergaard formulas. Thanks to this software, the user who wants to design the concrete pavement as concrete road slab can obtain the essential parameters automatically by entering the required data for the design.

Keywords: PCA1984, AASHTO 1993, Rigid pavement, Westergaard Analysis, Visual Programming

1. Introduction

Rigid pavements are built with Portland Cement Concrete. The first concrete pavement was built in Bellefontaine, Ohio in 1891 and the pavement was only 3 m wide and 67.1 m long. [1] From the first time they were built in Ohio their use is increasing day by day and only in the USA the concrete pavement's length has exceeded 100.000 km. Concrete pavements which meet both public and private institutions' needs with being strong and its durability being high, is a versatile paving implementation. Thanks to the high rigidity of the concrete, concrete pavements can transmit the applied loads to the sub-grade in larger and homogeneous areas. By this means, it forms an alternative for the flexible superstructure [2-3].

Concrete pavements are extensively used as a superstructure element as road slab for highways, airports, industrial grounds, streets, parking areas etc. If designed correctly and constructed well, they are capable to service for dozens of years without any maintenance cost [2]. In terms of cost, concrete pavement's initial cost is higher than pavement but it needs less maintenance throughout its lifetime [3].

Sound engineering is considerably important at this point. Because if the pavement's thickness is designated more than it should be, its initial manufacturing cost will increase. [2,3,4] In contrast, if the thickness of the pavement is thinner than it should be, its maintenance cost will increase. Therefore, maximum effort should be shown for the design of concrete roads.

Design methods which are used for concrete pavement design are generally based on mechanical and experimental sources. Another criterion used in concrete pavement designs is experience. Therefore, because of the criteria of concrete pavement designs that have to be taken into consideration come from different sources, it's more complicated than expected. To facilitate this complication, design methods that have an experimental and mechanic infrastructure which have been developed by several organizations have been presented [6-9]. AASHTO 1993 and PCA 1984 methods are the first of these methods. Both methods have been used for long years by both designers and researchers.

Design methods are intensively based on experimental findings and mechanistic fundamentals. Mechanically it is important to know the maximum deflection in vertical direction and maximum stress happening in pavement under axle loads and thermal loads in concrete pavements [11,12]. This deflection and stress may be found by using the finite element method and also be calculated using the closed-form formulation. Westergaard equations which are formed of center, corner, and edge loadings according to critical loadings, have still survived until today and are used extensively [1,2,3]

As a result of edge loading while maximum stress takes place in the pavement, maximum deflection occurs when the load is near the corner. It is the key element for design to know the deflections and stresses under wheel loads. [9,10,13]

2. Thickness Design in PCA 1984 Method

The Portland Cement Association's (PCA) thickness-design method for concrete pavements was published in 1984. This method can be applied to jointed plain concrete pavement (JPCP), jointed reinforced concrete pavement (JRCP) and continuously reinforced concrete pavement (CRCP). The PCA 1984 method is a design methodology which has a mechanical and experimental infrastructure and is based on according to the maximum deflection which occur at vertical direction and the maximum stresses which the vehicles' load creates on the pavement. The maximum stresses and deflections which are obtained via mechanical methods are closely associated with the design tables and charts which are made by PCA. Fig 1 shows PCA design method's steps.

PCA 1984 method consists of erosion and fatigue analysis. For fatigue analysis, the ratio of maximum tensile stress of the pavement under repetitive traffic loads and the concrete's modulus of rupture are used. Cumulative damage concept (CDF) is used for the fatigue analysis and if CDF exceeds 1.00, it is assumed that the pavement thickness is not sufficient. [8,9]

In eq. (1) D_r is the cumulative damage ratio which will be caused throughout its lifespan 's design referring to all load groups, is the predicted number of repetitions for each load group and is the allowable number of repetitions for each load group.

$$D_r = \sum \frac{n_i}{N_i} \tag{1}$$

The Cumulative damage concept is used for both fatigue and erosion analysis.

Fatigue analysis which is based on edge loading, is the most critical loading situation in terms of stress. The maximum stresses that occur for each axle group and the modulus of rupture of the concrete are compared and with the help of charts the allowable repetition numbers are specified. Fig 2 shows PCA fatigue analysis chart.

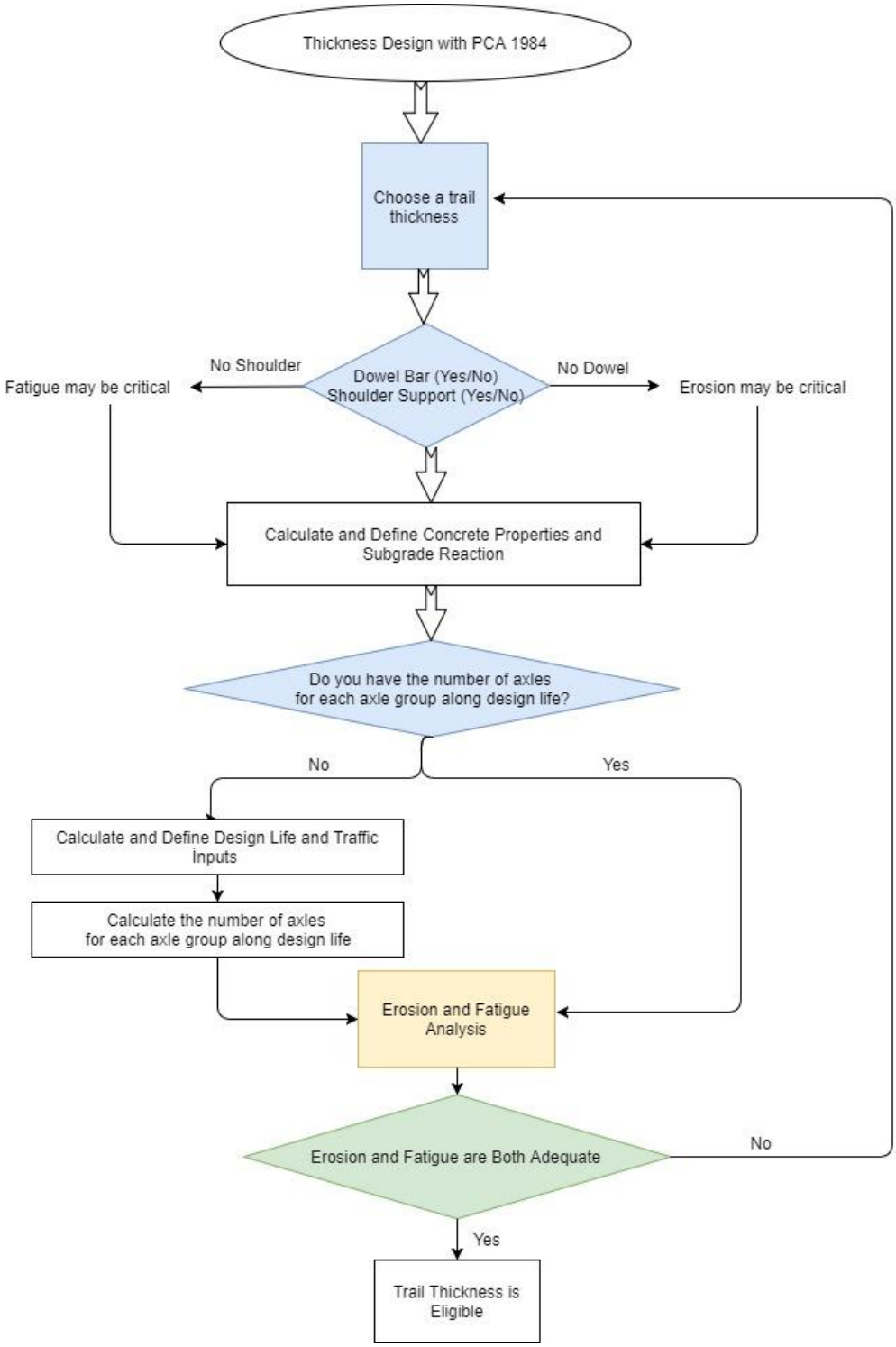

Fig. 1. PCA Flow Chart

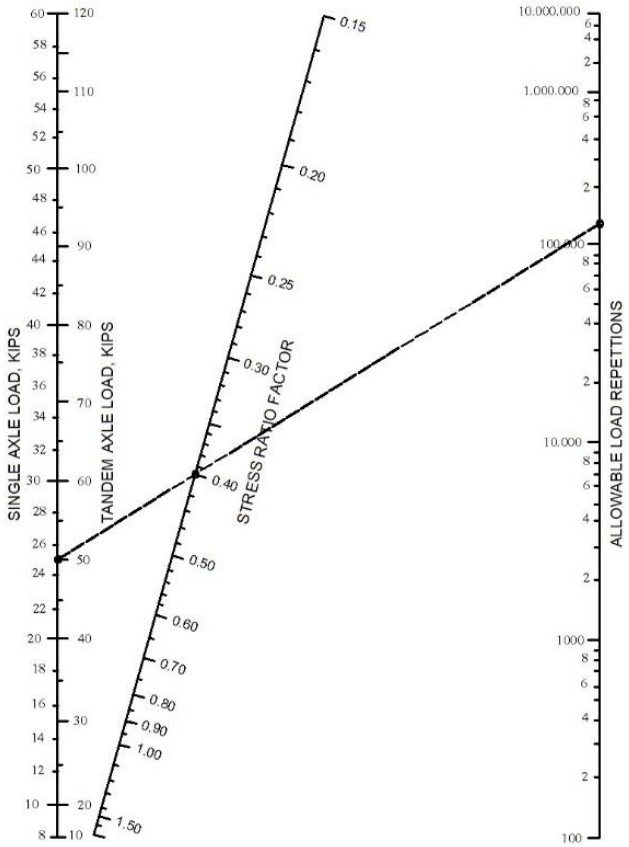

Fig. 2. PCA fatigue analysis chart (PCA, 1984)

The situation of corner loading is the most critical style of loading in terms of the deformation which occur in vertical direction. For this reason, deformation which occurs in the situation of corner loading, is used for erosion analysis. In the PCA method whether the dowel bars on the joints is important because it blocks the ground erosion and joint deterioration. Also in the tables presented in PCA 1984 have been prepared considering dowel bar and shoulder support.

Axle loads depending on fatigue, it's place and effect in erosion of every load group in the design of the PCA 1984 method should be found by looking at the charts one by one. In this situation, as a result of a single change in design, the analyses have to be repeated. And this causes a great waste of time for designers. Furthermore, the difficulty of using charts and how making a small mistake will have a massive effect on the design, makes it harder for designers.

The details of the PCA method haven't been specified clearly in literature. For this reason, designers have to use the tables and charts that the PCA 1984 design method presents. Lee and the others have analyzed the PCA method to eliminate this obligation in their study that they have carried out. As a result of this study, they have created several formula sets instead of tables and charts [5].

$$\sigma_{eq} = \frac{6 * M_e}{h^2} * f_1 * f_2 * f_3 * f_4 \tag{2}$$

$$M_e = \begin{cases} = -1600 + 2525 * \log(\ell) + 24.42 * \ell + 0.204 * \ell^2 & SA/NS \\ = 3029 - 2966.8 * \log(\ell) + 133.69 * \ell - 0.0632 * \ell^2 & TA/NS \\ = (-970.4 + 1202.6 * \log(\ell) + 53.587 * \ell) * (0.8742 + 0.0108 * k^{0.447}) & SA/WS \\ = (2005.4 - 1980.9 * \log(\ell) + 99.008 * \ell) * (0.8742 + 0.01088 * k^{0.447}) & TA/WS \end{cases}$$

$$f_1 = \begin{cases} (24/SAL)^{0.06} * (SAL/18) & SA \\ (48/TAL)^{0.06} * (TAL/36) & TA \end{cases}$$

$$f_2 = \begin{cases} 0.892 + h/85.71 - h^2 3000 & NS \\ 1 & WS \end{cases}$$

$$f_3 = 0.894 \qquad \text{for \%6 truck at the slab edge}$$

In Eq. (2) σ_{eq} is the equivalent stress (psi), h is the thickness of the pavement (in), ℓ is the relative stiffness of the subgrade system (in), k is the modulus of subgrade reaction (pci) f1, f2, f3 and f4 are the correction factors, SAL is single axle load, TAL is tandem axle load, WS means with shoulder, NS means no shoulder, TA and SA means tandem and single axle respectively.

$$\log N_f = 11.737 - 12.077 * (\sigma_{eq}/S_C) \qquad \sigma_{eq}/S_C \geq 0.55 \tag{3}$$

$$N_f = \left(\frac{4.2577}{\sigma_{eq}/S_C - 0.4325} \right)^{3.268} \qquad 0.45 < \sigma_{eq}/S_C < 0.55$$

$$N_f = \text{Unlimited} \qquad \sigma_{eq}/S_C \leq 0.45$$

In Eq. (3) N_f is the allowable load repetitions S_c is the concrete modulus of rapture.

3. Thickness Design in AASHTO 1993

In the instrument of the AASHTO 1993 method, the thickness of the slab and the reinforcement can be calculated for the concrete pavement. Either for its rigid superstructure design or its flexible superstructure design, AASHTO has constituted one of the most accepted design specifications by superstructure engineers and scientists. Because this constituted design is based on both experimental and mechanic foundations, this ensures it to get better results in design.

The AASHTO design method has published guides in the years 1972, 1986, 1993, 1998 and 2004. These guides were formed based on road tests and the data that was attained was stated with empirical formula. All these published guides, along with having the same concept with each other, each guide was developed with new additions. AASHTO 1993 method uses ESAL (Equivalent Single Axle Load) approach which is highly using approach by designers [14]. Figure 3 shows AASHTO design method's steps.

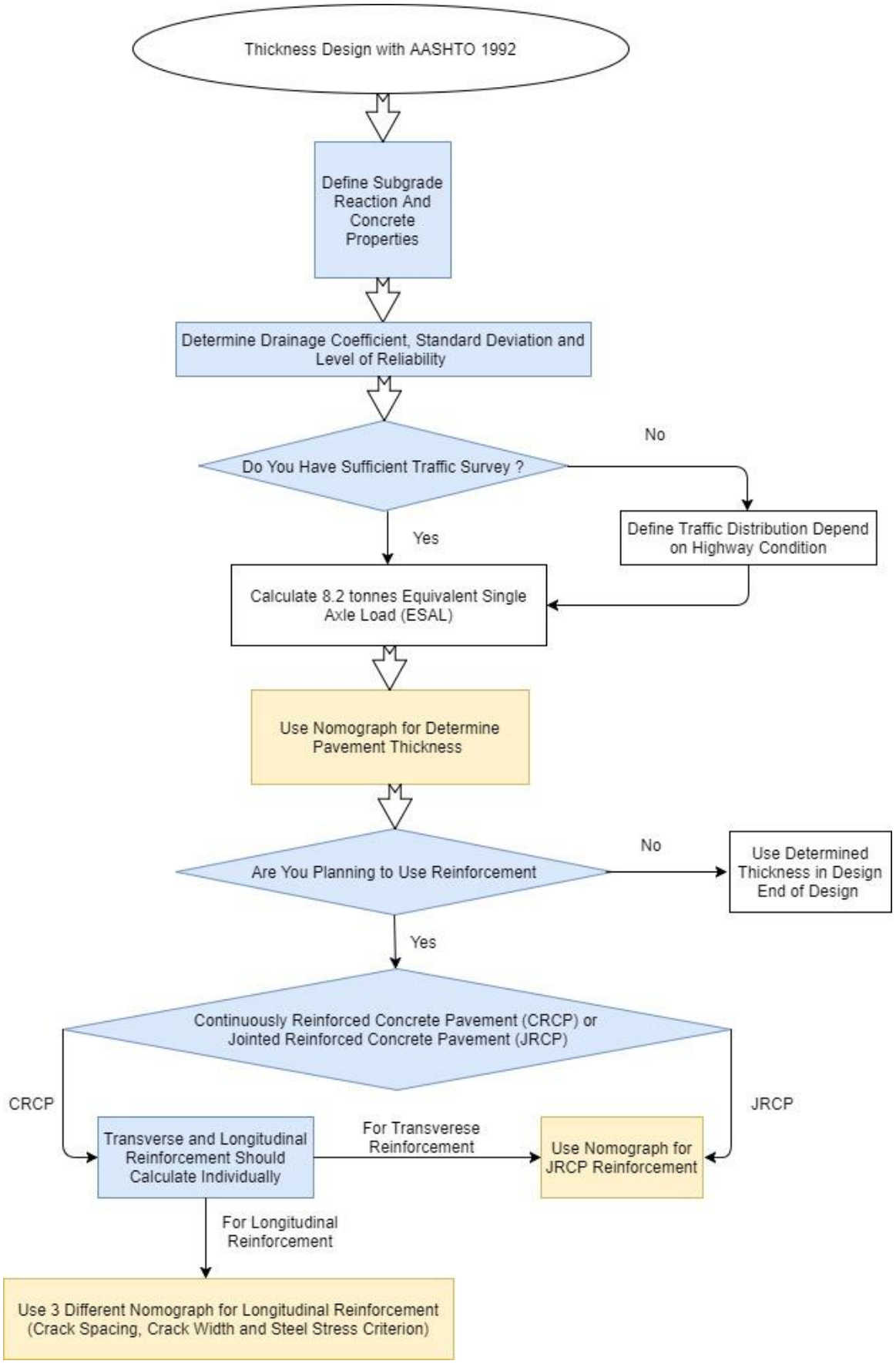

Fig. 3. AASHTO Flow Chart

As in PCA 1984, in the AASHTO 1993 method a trail thickness is also not wanted. According to the equation prepared by AASHTO, the calculation of the thickness of the slab can be done by entering the required parameters.

In the equation of the calculation of thickness presented in the AASHTO 1993 method, the value of the thickness of the slab (D) both affects the other values and also is affected from them. To calculate the thickness of the slab by using this formula, can only be done by doing iteration. For this reason, the solution for this formula is quite difficult. Because of the difficulty of calculating the equation by hand, some charts have been developed for designers to make it easy for them.

According to AASHTO's 1993 design method, for the calculation of the thickness of the slab, as a result of experimental studies, the empirical formula on Eq 4 was obtained and doing the calculation of the thickness according to this formula was predicted.

In Eq (4) S_0 is the standard deviation, Z_R is the reliability, W_{18} the 18 kip equivalent single axle loads, D is the pavement thickness, P_t is the terminal serviceability index, C_d is the level of drainage, k is the effective module of subgrade reaction, E_c is the modulus of elasticity of concrete, J is the load transfer coefficient, S_c is the flexural strength of concrete ΔPSI is the total change in serviceability index.

$$\log_{10} W_{18} = S_0 Z_R + 7.35\log_{10}(D+1) - 0.06 + \frac{\log_{10}\left[\frac{\Delta PSI}{4.5-1.5}\right]}{1+\frac{1.642x10^7}{(D+1)^{8.46}}} + \ldots \quad (4)$$

$$\ldots + (4.22 - 0.32P_t)\log\left[\frac{C_d S_c'\left[D^{0.75} - 1.132\right]}{215.63J\left[D^{0.75} - \frac{18.42}{\left(\frac{E_c}{k}\right)^{0.25}}\right]}\right]$$

Critical stresses may occur between concrete pavements especially in joint areas during the passage of vehicles and due to environmental factors. Because of its concrete structure, it is more prone to cracks. These cracks increase with the passage of vehicles and environmental factors and reduces the lifespan of the road. Therefore, especially in joint areas, it has a great importance in terms of reinforcement crack inspection.

In the AASHTO 1993 design method, reinforcement designs were prepared separately for continuously reinforced concrete pavement and jointed reinforced concrete pavement. Once again based on experience, experimental studies and mechanic examinations, several formulas and chats were created to calculate the amount of reinforcement to be used in the design and the reinforcement measurements.

The calculation of transverse reinforcement for continuously reinforced concrete pavements and the reinforcement calculations used for jointed reinforced concrete pavements are exactly the same. For the reinforcement calculation, the formula in Eq. 5 can be used.

$$P_S = \frac{LF}{2f_s} x100 \tag{5}$$

In Eq (5) L is the length of pavement, F is the friction factor, fs is the steel working stress, Ps is the percent steel reinforcement for JRCP and transverse reinforcement in CRCP.

There are 3 different criteria in the longitudinal reinforcement calculation of CRCP. These criteria are the criterion of distance between cracks, the criterion of crack width and the criterion of allowable reinforcement stress. According to all three criteria, the required reinforcement ratio should be calculated and the highest donate ratio should be selected.

In Eq. (6), Eq. (7) and Eq. (8) $\bar{X}$ is the crack spacing, f_t is the concrete tensile strength, α_s and α_c are steel and concrete thermal expansion coefficient respectively, ϕ is the bar diameter, σ_w is the tensile stress due to wheel load, P is the steel percentage, Z is the concrete shrinkage at 28 days.

$$\bar{X} = \frac{1.32\left(1+\frac{f_t}{1000}\right)^{6.70} x\left(1+\frac{\alpha_s}{2\alpha_c}\right)^{1.15} x(1+\phi)^{2.19}}{\left(1+\frac{\sigma_W}{1000}\right)^{5.20} x(1+P)^{4.60} x(1+1000Z)^{1.79}} \tag{6}$$

In Eq (7) CW is the crack width.

$$CW = \frac{0.00932\left(1+\frac{f_t}{1000}\right)^{6.53} x(1+\phi)^{2.20}}{\left(1+\frac{\sigma_W}{1000}\right)^{4.91} x(1+P)^{4.55}} \tag{7}$$

In Eq. (8) σ_s is the steel stress.

$$\sigma_S = \frac{1.32\left(1+\frac{f_t}{1000}\right)^{6.70} x\left(1+\frac{\alpha_s}{2\alpha_c}\right)^{1.15} x(1+\phi)^{2.19}}{\left(1+\frac{\sigma_W}{1000}\right)^{5.20} x(1+P)^{4.60} x(1+1000Z)^{1.79}} \quad (8)$$

3. Maximum Principle Stress and Maximum Deflection with Westergaard

In the studies that Westergaard (1926) has carried out, he developed formulas for the stress and deflections which will occur on the result of interior, edge and corner loading applied on the slab along with formulas that can also calculate deflections and stresses that will occur with the change of temperature. In the analysis of Westergaard, while the pressure between the slab and the ground is proportional with the deflection at that point, it is independent from the deflection at the other points. It is assumed that the ground and the slab are in full contact and the response of the ground to the slab is equal everywhere. This simplified acceptation is named liquid ground or the Winkler Foundation. [13]

For the analysis of the slabs, Westergaard equations, have been used to widely for a very long time to calculate the stresses which occur because of traffic loads and thermal loading. AASHTO and including PCA methods have also been used in many design methods.

Westergaard identified the corner, edge and interior loadings as critical loadings and tried to calculate the critical stresses which will occur on the slabs according to all three loading situations mathematically. Accordingly, considering all three loading situations he formulized the maximum stress and maximum deflections. Fig 4 shows critical load positions.

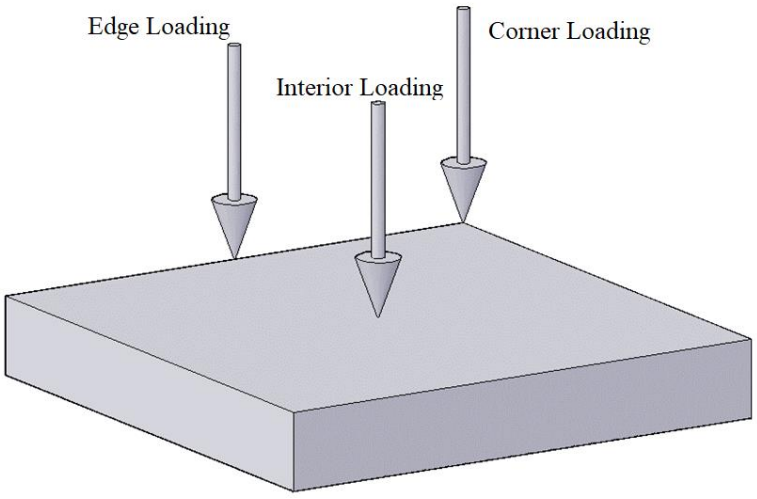

Fig. 4. Critical load positions

For the corner loading situation, after Westergaard the maximum stresses and deflection equations which occur in the situation of corner loading were updated by Ioannides (1985).

In Eq. 9, Eq. 10, Eq. 11, Eq. 12, Eq. 13 and Eq. 14 σ_c and Δ_c are the maximum tensile stress and maximum deflection due to corner loading respectively, a is the radius of loading area, D is the pavement thickness, P is the wheel load, l is the radius of relative stiffness, k is the modulus of subgrade reaction.

$$\sigma_c = \frac{3P}{D^2}\left[1-\left(\frac{1.772a}{l}\right)^{0.72}\right] \tag{9}$$

$$\Delta_c = \frac{P}{kl^2}\left[1.205-0.69\left(\frac{1.772a}{l}\right)\right] \tag{10}$$

In Eq. 11 and 12 σ_c and Δ_c are the maximum tensile stress and maximum deflection due to edge loading respectively.

$$\sigma_e = \frac{0.803P}{D^2}\left[4\log\left(\frac{l}{a}\right)+0.666\left(\frac{a}{l}\right)-0.034\right] \tag{11}$$

$$\Delta_e = \frac{0.431P}{kl^2}\left[1-0.82\left(\frac{a}{l}\right)\right] \tag{12}$$

In Eq.13 and 14 σ_c and Δ_c are the maximum tensile stress and maximum deflection due to interior loading respectively.

$$\sigma_i = \frac{0.316P}{D^2}\left[4\log\left(\frac{l}{b}\right)+1.069\right] \tag{13}$$

$$\Delta_i = \frac{P}{8kl^2}\left[1+\frac{1}{2\pi}\left[\ln\left(\frac{a}{2l}\right)-0.673\right]\left(\frac{a}{l}\right)^2\right] \tag{14}$$

b may be written as,

$$\begin{aligned} b &= a && \text{when } a \geq 1.724D \\ b &= \sqrt{1.6a^2+D^2}-0.75h && \text{when } a < 1.724D \end{aligned} \tag{15}$$

When looked at all three loading situations in terms of deflection, the most critical loading situation occurs as a result of corner loading. For this reason, deflections which are attained by corner loading are used in erosion analysis in the PCA method. Because of edge loading, maximum principle stresses occur. Because stresses that occur by edge loading brings forth maximum stresses, the corner loading situation is considered in fatigue analyses.

4. SDU.Pave.R Software

The slab thickness design for concrete roads are affected from many properties such as the properties of the concrete, traffic loads and expectations from the design. For this reason, different scenarios being established and analyses being done for different circumstances are important in terms of finding the right thickness of the slab. While slabs which are thicker than they should be increase the cost, concrete slabs which are designed thinner than they should be deteriorate earlier, nevertheless causing economic loss. For this reason, it is quite important to determine the right thickness of the slab.

Although design programs which are presented for concrete roads guide the designer with the instructions they give, identifying different scenarios to determine the right thickness of the slab and making a design of the thickness of the slab according to these scenarios are not always possible. Because there are too many detailed calculations in the formulas of the presented design methods. Furthermore, charts which are used to determine the thickness and reinforcement, are often misread. Designers who do these calculations by hand either have difficulty or make mistakes in determining the thickness of the slab.

In this study, a user-friendly software was developed for overcoming the difficulties of the calculations of reinforcements and the thickness of the concrete roads. With the help of this user-friendly software, the solutions of the Westergaard equation can be easily done with PCA 1984 and AASHTO 1993. The home page of SDU.Pave.R have been shown in Fig 5.

Fig. 5 Home page of SDU.Pave.R

Through this software both the thickness analysis and donate calculations can be done using AASHTO 1993. The donate calculation is done separately for continuously reinforced concrete pavements and separately for jointed reinforced concrete pavements. Moreover, you can see the recommended values for the selected input when you click on the question marks buttons in the software. In this way, the user can make a more accurate design by getting information about inputs he doesn't know of.

For calculate slab thickness and steel percentage according to AASHTO design method with SDU.Pave.R software, we used example parameters given in Table 1. Steel percentage calculated for JRCP (Jointed Reinforced Concrete Pavement). The results of analyzes which made with SDU.Pave.R also given in Table 1 as output. When the results compare with the results obtained from the charts given in AASHTO Design Guide, we may see the results are totally overlapping. Instead of using AASHTO charts, thickness and steel percentage can easily calculate with SDU.Pave.R.

Table 1. AASHTO Design Example Inputs and Outputs

Input	**Value**
Modulus of Sub. Reaction (MN/m^3)	20
Standard Deviation	0.3
Drainage Coefficient	1
Elastic Modulus of Concrete (MPa)	35000
Number of Axle Load (million)	6
Initial Serviceability Index	4.20
Terminal Serviceability Index	2.6
Concrete Modulus of Rupture (MPa)	4.5
Load Transfer Coefficient	3.2
Slab Length (m)	12
Friction Factor	1.5
Steel Working Stress (MPa)	2000
Output	
Slab Thickness (cm)	25.7
Steel Percentage (%)	0.1

In the PCA 1984 method, fatigue and erosion analyses should be done for each axle type and axle weight separately. In these analyses, the analyses should be repeated one by one for each load by looking at the table and charts. This process is a long and troublesome process. The SDU.Pave.R software allows these analyses to be done quite easily and without errors. Furthermore, future traffic and truck quantities can be calculated with the help of the traffic option in the PCA 1984 module. The AASHTO thickness and reinforcement design page of SDU.Pave.R has been shown in Fig 6.

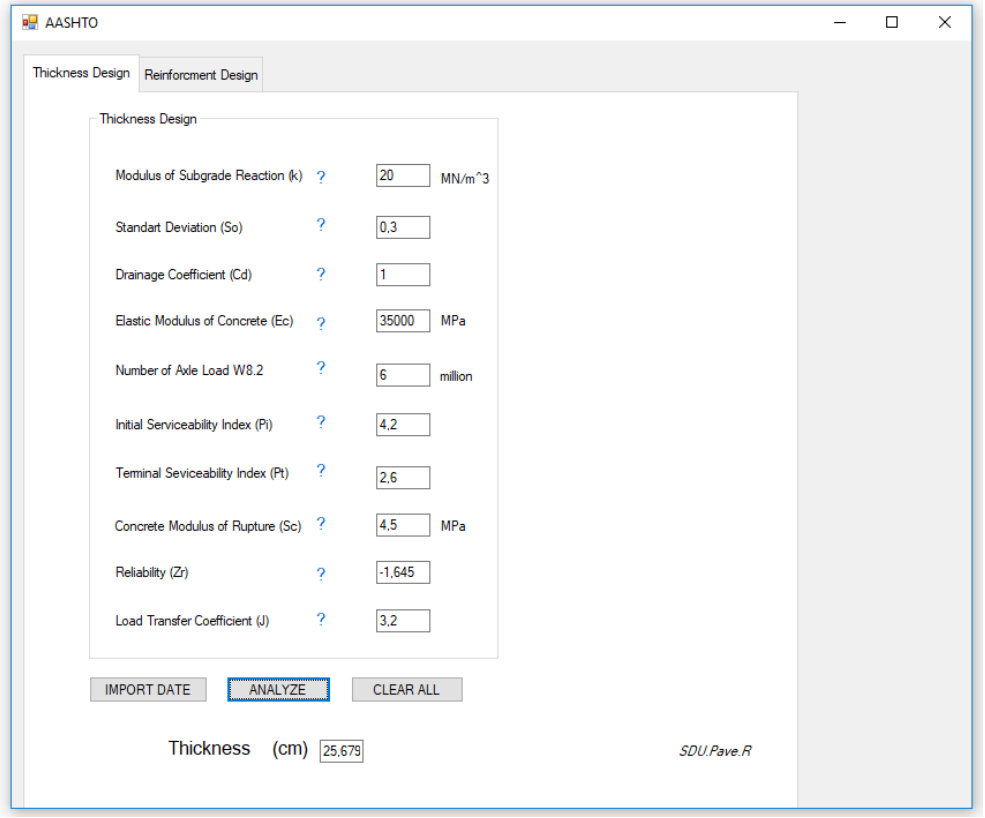

Fig. 6. AASHTO Thickness and Reinforcement Design with SDU.Pave.R

SDU.Pave.R PCA module also can help designers and researchers. Instead of using PCA method's tables and charts, fatigue and erosion analyzes may run easily with SDU.Pave.R software. For an example we chose trail pavement thickness as 25.5 cm. We considered doweled joint and no shoulder situation. The parameters using for this example presented Table 2. Fatigue analyze result with SDU.Pave.R software has been shown in Fig 7. End of the analyzes made with SDU.Pave.R fatigue and erosion were calculated as %84.92 and %18.71 respectively.

Table 2. PCA Design Example Inputs and Outputs

Input	**Value**
Trail Pavement Thickness (cm)	25.5
Modulus of Sub. Reaction (MN/m^3)	20
Concrete Modulus of Rupture (MPa)	4.5
Elastic Modulus of Concrete (MPa)	35000
Poisson Ratio of Concrete	0.13
Load Safety Factor	1.1
Average Daily Traffic (Both Direction)	3500
Proportion of Trucks in Right Line	0.75
Design Period (Years)	30

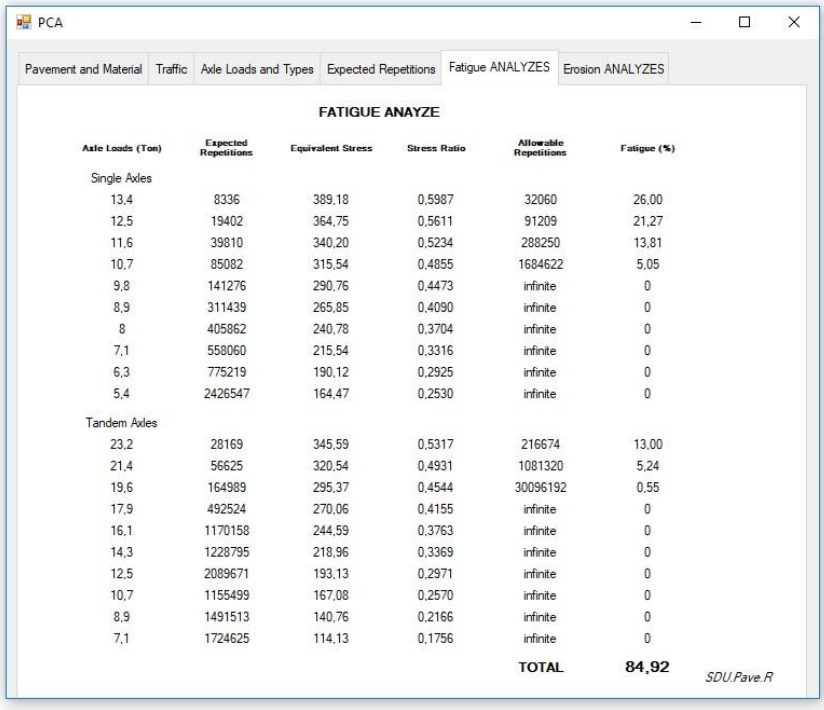

Fig. 7. PCA Fatigue Analyses with SDU.Pave.R

The formulas used in Westergaard analyses are quite complex. Therefore, it takes a long time to repeat the analysis according to different loading scenarios. With the SDU.Pave.R software, analyses can be performed according to the three critical loading situations (interior, edge, corner). Furthermore, the loading format is visualized according to the selected situation, making it easier for users (Fig 8).

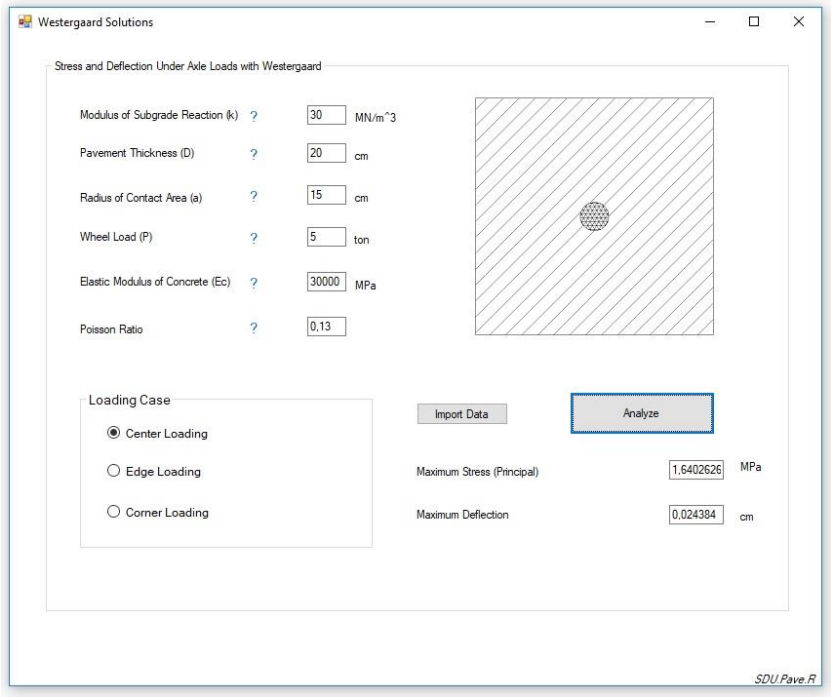

Fig. 8. Westergaard Solution with SDU.Pave.R

5. Concluding Remarks

In this study, a user-friendly software including the AASHTO 1993 and PCA 1984 methods which are the most used methods for concrete slab design and the Westergaard equations has been developed. Thanks to this software named SDU.Pave.R, it has been ensured that the design of the concrete slab thickness and reinforcement can be done quickly and easily without depending on charts and equations. There is no other software offering design methods under the same software. The SDU.Pave.R has bridged the gap and has allowed users who want to calculate the concrete slab thickness with different design methods. Furthermore, the fact that the software offers both Turkish and English language support makes the program easier to use from different countries. In addition, with the choice of the American and SI unit system in the software, it allows extensive usage for users in countries using a different unit system.

Acknowledgements

The financial support of the ÖYP Unit of Süleyman Demirel University is gratefully acknowledged.

References

[1] Fitch, *M. Bellefontaine, Ohio: Home of America's Oldest Concrete Pavement.* 1996

[2] Delatte, N. J., Concrete Pavement Design, Construction, and Performance. Crc Press, 2014.

[3] Huang, Y. H., Pavement Analysis and Design. Pearson Education Inc. 2004.

[4] Yoder, E. J., Witczak, *M. W., Principles of Pavement Design*. John Wiley and Sons. 1975.

[5] Lee, Ying-Haur, et al. Modified Portland cement association stress analysis and thickness design procedures. *Transportation Research Record Journal of the Transportation Research Board,* 1568: 77-88. 1997.

[6] AASHTO, Guide for Design of Pavement Structures. Washington DC, American Association of State Highway and Transportation Official, 1986.

[7] AASHTO, Guide for Design of Pavement Structures. Washington DC, American Association of State Highway and Transportation Official, 1993.

[8] Portland Cement Association, Thickness Design for Concrete Pavements. Skokie, IL: Portland Cement Association, 1966.

[9] Portland Cement Association, Thickness Design for Concrete Highway and Street Pavements, Engineering *Bulletin EB109P. Skokie, IL: Portland Cement Association*, 1984.

[10] Maitra, S. R., Reddy, K. S., Ramachandra, L. S., Estimation of Critical Stress in Jointed Concrete Pavement. *Procedia-Social and Behavioral Sciences*, 104, 208-217, 2013.

[11] Choi, S., Na, B. U., Won, M. C., Mesoscale Analysis of Continuously Reinforced Concrete Pavement Behavior Subjected to Environmental Loading. Construction and Building Materials, 112, 447-456, 2016.

[12] Sabih, G., Tarefder, R. A., Impact of Variability of Mechanical and Thermal Properties of Concrete on Predicted Performance of Jointed Plain Concrete Pavements. *International Journal of Pavement Research and Technology*, 9(6), 436-444, 2016.

[13] Westergaard, H. M ., Analysis of Stresses in Concrete Pavement Due to Variations of Temperature. *Proceedings, Highway Research Board, Vol. 6, pp. 201–215,* 1926.

[14] Bordelon, A. C., Hiller, J. E., Roesler, J. R., Cervantes, V. G., Investigation of ESALs versus Load Spectra for Rigid Pavement Design. *Airfield and Highway Pavements* 488-499, 2015.

International Journal of Engineering & Applied Sciences (IJEAS)
Vol.9, Issue 4 (2017) 17-27
http://dx.doi.org/10.24107/ijeas.336034
Int J Eng Appl Sci 9(4) (2017) 17-27

Comparison of Linear and Nonlinear Seismic Behavior of 2D and 3D RC Buildings

Esra Özer [a], Muhammet Kamal [b], Mehmet İnel [c]*

Pamukkale University, Faculty of Engineering, Civil Engineering Department
[*]E-mail address: esrao@pau.edu.tr

ORCID numbers of authors:
0000-0002-7778-0119[a], 0000-0001-6648-2346[b], 0000-0002-8323-259X[c]

Received date: August 2017
Accepted date: December 2017

Abstract

This study compared displacement demands obtained from linear and nonlinear time history analyses of 2D and 3D models to investigate how 2D models reflect 3-D models. Estimates of 2D and 3D linear and 2D nonlinear models were also compared to that of 3D nonlinear model to visualize success of linear and 2D nonlinear models in seismic displacement estimates of RC buildings. A total of 288 dynamic analyses were performed with 12 different records taking into account two principal directions of 10-, 15- and 20-storey buildings. Outcomes of the current study imply that 2D representation of 3D models needs careful modelling. Buildings are usually designed according to related earthquake code considering both gravity and seismic loads. Then, an interior frame is used for 2D modelling. The periods of 3D and 2D models need to be closer for proper representation. Another observation is that the 2D linear elastic models do not properly represent the 3D nonlinear models. Thus, it is recommended to use 3D models when linear modelling is preferred. Since 2D nonlinear models represent reasonably well their 3D nonlinear ones, 2D modelling can be preferred for buildings with no irregularity due to extensive labor and time required for 3D nonlinear models.

Keywords: displacement demands, 2D and 3D frame models, linear and nonlinear analyses, time history analysis, ground motions with forward directivity effects.

1. Introduction

Displacement demand estimates of building stock in earthquake prone countries are essential for seismic performance evaluation. Static or dynamic analysis can be used in estimating displacement demands of structures. Although nonlinear time history analysis provides precise estimates, it may cause labor and time loss. Therefore static (pushover) analyses or nonlinear time-history analyses of "equivalent" SDOF system reflecting 3D models are preferred for their simplicity in estimating displacement demands of structures. Also, linear time history analyses are used for estimates of seismic displacement demands.

In this study, three structures selected as 10-, 15- and 20-storey are considered to represent mid-rise reinforced concrete buildings. These buildings are modelled as three dimensional (3D) frame elements without shear walls in SAP2000 [1]. In addition, two dimensional (2D) models were derived from the interior frames in two principal directions of 3D models. In total, 27 models as three 3D and six 2D models for each building were created. 12 past earthquakes records with forward directivity are selected for using linear and nonlinear time-history analysis. In part 1 of the study, displacement demands obtained from linear and nonlinear time history analyses of 2D and 3D

models were compared to investigate how 2D models reflect 3-D models. In part 2 of the study, the estimates of 2D and 3D linear and 2D nonlinear models were compared to that of 3D nonlinear model in order to visualize success of linear and 2D nonlinear models in seismic displacement estimates of RC buildings. A total of 288 dynamic analyses were performed with 12 different earthquakes records taking into account the two principal directions of 10-, 15- and 20-storey buildings. The outcomes and findings of the study are useful to better understand the consequences and issues in implication of 2D and 3D linear and 2D nonlinear models.

2. Description of buildings and modeling approach

10, 15 and 20-storey reinforced concrete buildings were taken into consideration as mid-rise buildings for this study. Building models have double symmetry axis; consists of a typical beam-column RC frame system with no shear walls. The plan view of the 3D models and the 2D models derived from the inner axes of this model were given in Fig 1. The selected buildings are designed according to modern Turkish Earthquake Code (TEC-2007) considering both gravity and seismic loads [2]. A design ground acceleration of 0.40g assuming the highest seismicity zone and soil class Z3 that is similar to the class C soil of FEMA-356 is assumed [3]. Compressive concrete strength value of 35 MPa is considered while the yield strength of both longitudinal and transverse reinforcement is assumed to be 420 MPa. The period values of the dominant vibration mode of the models are given in Table 1. Nonlinear models have been developed to investigate how the linear models reflect the nonlinear models. Nonlinear behavior was achieved through plastic hinges defined at both ends of beams and columns. The plastic hinge length in the critical sections was calculated as half (h / 2) of the cross section height in the relevant direction as specified in TEC-2007 for the Mander confined concrete model [4-5]. The software SEMAp is used for moment-curvature analyses of RC sections reflecting their material properties longitudinal and transverse steel content, and axial load level of the critical sections [6]. Using the curvature values obtained as a result of the analyses, the rotation values of the critical points given in Figure 2 were calculated [7]. SAP2000 is used for linear and nonlinear analyses [1]. Newmark mean acceleration method is used for linear and nonlinear time history analyses in SAP2000. Effective stiffness values for all linear and nonlinear models are obtained per 2007 Turkish Earthquake Code; 0.4EI for beams and values between 0.4EI and 0.8EI depending on axial load level for column elements [2, 8, 9]

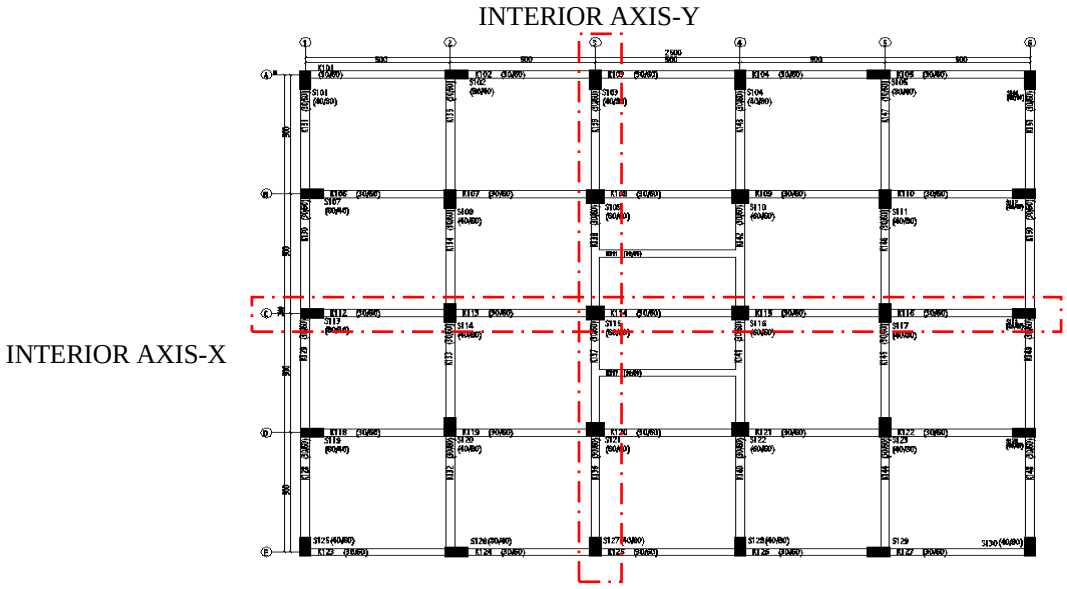

Fig.1. Plan view of the considered buildings (Selected frame models are also marked.)

Table 1. The dominant vibration periods in the relevant direction of the models used in the study (T_1)

Models	T_1 (s)	Models	T_1 (s)	Models	T_1 (s)
10S-2D-X	1.37	15S-2D-X	2.11	20S-2D-X	2.35
10S-2D-Y	1.31	15S-2D-Y	1.97	20S-2D-Y	2.15
10S-3D-X	1.35	15S-3D-X	1.76	20S-3D-X	1.97
10S-3D-Y	1.31	15S-3D-Y	1.71	20S-3D-Y	1.87

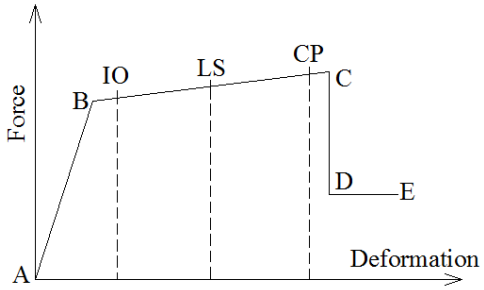

Fig.2. Typical strength-deformation relation

3. Ground motions

A total of 12 earthquake records with forward directivity effect were used in the study. Forward directivity produces ground motion which contains large amplitudes and short durations [10-11]. Because of this, acceleration records with forward directivity can cause very serious demand increases in structures near the fault, as they carry relatively large velocity pulse effects [8, 9, 12]. Such acceleration records take part in some sources as earthquakes carrying pulse effect "near source" [13].

Table 2. Earthquake acceleration records used in the study and their characteristics

No	Earthquake	Date	Station	Component	PGA (g)	PGV (mm/s)	Vs30 (m/s)
1	Cape Men.	25.04.1992	Petrolia	090	0.662	897	712.8
2	Duzce	12.11.1999	Bolu	090	0.822	621	326.0
3	Erzincan	13.03.1992	Erzincan10	EW	0.496	643	274.5
4	Imperial V.	15.10.1979	Brawley Air	315	0.220	389	208.7
5	Kobe	16.01.1995	Takatori	090	0.616	1207	256.0
6	Kocaeli	17.08.1999	Duzce	270	0.358	464	276.0
7	Kocaeli	17.08.1999	Gebze	000	0.244	503	792.0
8	Landers	28.06.1992	Lucerne	275	0.721	976	684.9
9	Loma Pri.	18.10.1989	Los Gatos Lex	090	0.508	728	1070.3
10	Morgan Hill	24.04.1984	C. Lake Dam	285	1.298	808	597.1
11	Northridge	17.01.1994	Newhall F.	360	0.590	972	269.1
12	Northridge	17.01.1994	Sylmar Ol	090	0.604	782	440.5

The characteristics of earthquake records used in this study are given in Table 2 [14]. Although there is a limited number of records with forward directivity in the literature, ground motion records with considerably large PGA band have been used. Elastic acceleration spectrum for the 5% damping ratio of the selected records are given in Figure 3. In addition, the average of acceleration records and response spectrum provided in Turkish Earthquake Code-2007 according to design earthquake with 10% probability of exceedance in 50 years for Z3 type soil was plotted. Despite the fact that the

selected records have a very broad scatter, it seems that it is very close to the spectrum plotted according to TEC-2007.

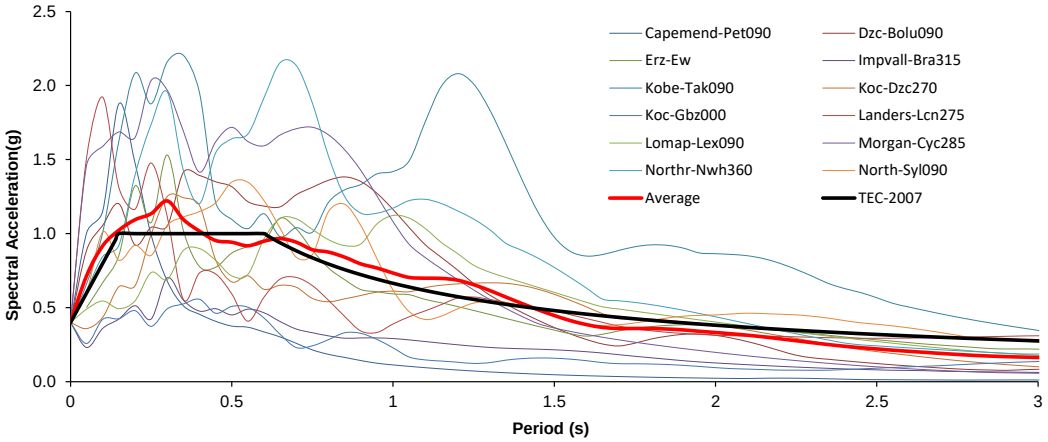

Fig.3. Elastic acceleration spectrum for 5% damping of earthquake acceleration records used in the study

4. Evaluation seismic demand

Seismic demand estimates of 288 linear and nonlinear time history analyses are compared. Building models used in the study are labeled as number of floor, type of model (2D or 3D), type of behavior (L: linear or N: nonlinear), and direction taken into account for analysis. For example, 10S-2DL-X and 10S-2DN-X represent the x-direction analysis result of a 10-storey two-dimensional linear and nonlinear model, respectively. Roof level displacement and interstory drift demands are used as seismic evaluation parameters.

Roof displacements are normalized by building height and called “roof drift ratio” while interstory displacement demands are normalized by story heights and called “interstory drift ratio”. Roof and interstory drift ratio demands are provided Tables 3 and 4, respectively.

Table 3. Roof drift ratio demands of 10-, 15- and 20-storey linear building models (%)

Earthquake	10-storey building				15-storey building				20-storey building			
	2D-L		3D-L		2D-L		3D-L		2D-L		3D-L	
	X	Y	X	Y	X	Y	X	Y	X	Y	X	Y
Cap-Pet090	0.16	0.16	0.15	0.15	0.09	0.09	0.09	0.09	0.07	0.07	0.06	0.07
Dzc-Bolu090	1.03	1.05	1.03	1.05	0.92	0.88	0.55	0.52	0.54	0.61	0.67	0.63
Erz-Ew	0.89	0.86	0.88	0.86	1.18	1.03	0.61	0.58	0.93	0.82	0.77	0.71
Impvall-Bra315	0.50	0.46	0.49	0.46	0.36	0.38	0.31	0.32	0.25	0.28	0.28	0.29
Kobe-Tak090	3.01	3.31	3.12	3.28	2.82	2.47	1.78	1.67	2.02	2.15	1.86	1.80
Koc-Dzc270	1.44	1.32	1.39	1.31	1.05	1.04	0.78	0.76	0.77	0.83	0.80	0.77
Koc-Gbz000	0.34	0.28	0.32	0.28	0.29	0.28	0.23	0.24	0.28	0.23	0.20	0.21
Landers-Lcn275	1.09	1.00	1.07	1.02	1.06	0.92	0.72	0.69	0.91	0.84	0.70	0.65
Lomap-Lex090	1.48	1.40	1.45	1.40	1.33	1.22	0.96	0.92	1.04	0.99	0.91	0.87
Morgan-Cyc285	0.95	0.98	0.97	0.99	0.60	0.62	0.57	0.57	0.41	0.46	0.46	0.47
Northr-Nwh360	2.00	1.86	1.96	1.86	1.19	1.27	1.02	0.99	0.88	0.94	0.95	0.96
Northr-Syl090	1.05	1.07	1.07	1.05	1.59	1.39	0.81	0.73	1.36	1.19	1.04	0.94
Maximum	3.01	3.31	3.12	3.28	2.82	2.47	1.78	1.67	2.02	2.15	1.86	1.80
Minimum	0.16	0.16	0.15	0.15	0.09	0.09	0.09	0.09	0.07	0.07	0.06	0.07
Average	1.16	1.14	1.16	1.14	1.04	0.97	0.70	0.67	0.79	0.78	0.72	0.70

Table 4. Interstory drift ratio demands of 10-, 15- and 20-storey linear building models (%)

Earthquake	10-storey building				15-storey building				20-storey building			
	2D-L		3D-L		2D-L		3D-L		2D-L		3D-L	
	X	Y	X	Y	X	Y	X	Y	X	Y	X	Y
Cap-Pet090	0.37	0.35	0.31	0.29	0.33	0.28	0.22	0.27	0.23	0.21	0.17	0.16
Dzc-Bolu090	1.37	1.48	1.42	1.47	1.46	1.07	0.94	0.96	1.22	1.07	0.94	0.82
Erz-Ew	1.20	1.18	1.18	1.17	1.85	1.82	1.12	0.94	1.39	1.51	1.34	1.19
Impvall-Bra315	0.64	0.57	0.62	0.58	0.56	0.52	0.53	0.53	0.46	0.42	0.38	0.40
Kobe-Tak090	3.93	4.54	4.20	4.49	3.87	3.43	2.44	2.36	2.58	2.72	2.60	2.31
Koc-Dzc270	1.78	1.73	1.79	1.73	1.63	1.66	1.13	1.10	1.11	1.20	1.20	1.10
Koc-Gbz000	0.51	0.43	0.49	0.43	0.48	0.43	0.41	0.38	0.45	0.33	0.33	0.35
Landers-Lcn275	1.49	1.56	1.50	1.23	1.43	1.28	1.01	0.81	1.35	1.05	0.69	0.60
Lomap-Lex090	1.85	1.86	1.87	1.84	1.80	1.67	1.36	1.31	1.48	1.37	1.18	1.12
Morgan-Cyc285	1.37	1.47	1.38	1.43	1.74	1.27	1.27	1.10	1.32	1.16	0.95	0.93
Northr-Nwh360	2.69	2.66	2.68	2.69	2.09	1.70	1.71	1.48	1.40	1.47	1.42	1.34
Northr-Syl090	1.55	1.45	1.52	1.45	2.11	1.81	1.08	1.00	2.00	1.62	1.33	1.21
Maximum	3.93	4.54	4.20	4.49	3.87	3.43	2.44	2.36	2.58	2.72	2.60	2.31
Minimum	0.37	0.35	0.31	0.29	0.33	0.28	0.22	0.27	0.23	0.21	0.17	0.16
Average	1.56	1.61	1.58	1.57	1.61	1.41	1.10	1.02	1.25	1.18	1.04	0.96

Roof drift ratios of each building subjected to 12 earthquake records for linear elastic analyses are plotted in Figure 4. It is obvious that 10-storey models have higher scatters for both 2D and 3D models. The comparison of 3D and 2D models shown in Figures 4a and 4b clearly points out that the 2D models have higher scatters. The ratios of maximum and minimum roof drifts are 21.6, 31.3 and 30.3 for 10-, 15- and 20-storey buildings, respectively. The difference in demands is an indication of different damage levels caused by ground motion records on the same buildings.

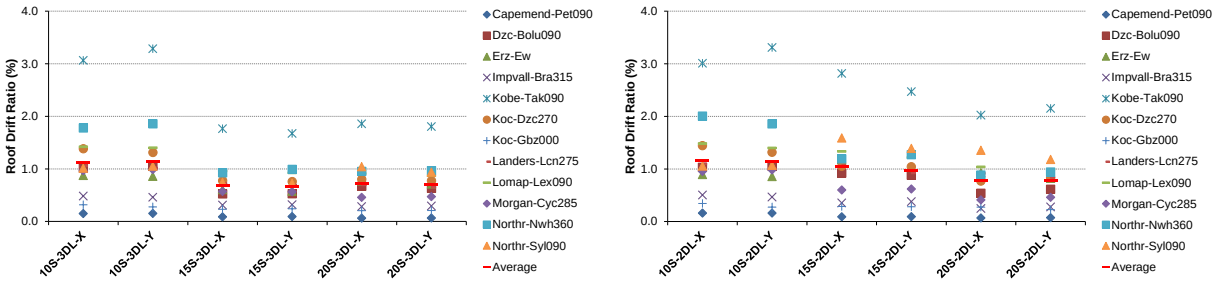

a) b)

Fig.4. Roof drift ratios of 10-, 15- and 20-storey buildings as linear modelled 3D and 2D (%)

When the average roof drift ratios are considered, the highest seismic risk is seen in 10-storey buildings. As shown in Figure 5, the spectral acceleration values corresponding to the period values of 10-storey buildings are higher than that of the other buildings in most of earthquake records, especially for strong ones (for example: Kobe-Tak090, Northr-Nwh360, Lomap-Lex090). The higher seismic acceleration demand for 10-storey buildings explains their higher displacement demands.

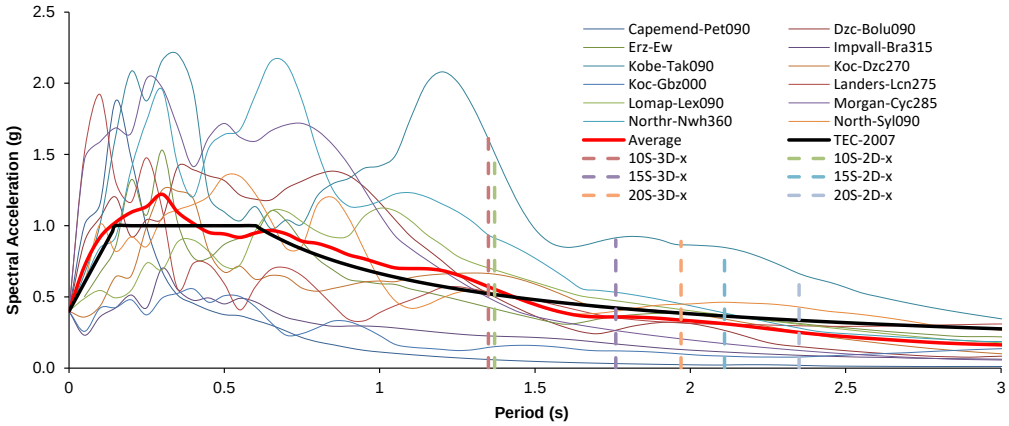

Fig.5. The spectral acceleration values corresponding to the period values of 10-, 15- and 20- storey buildings

Figure 6 plots interstory drift ratios of each building subjected to 12 earthquake records for linear elastic analyses. The scatter in 2D models is more apparent than that of 3D models. Among the building sets, the highest scatter for the interstory drifts is observed in the 10-storey buildings.

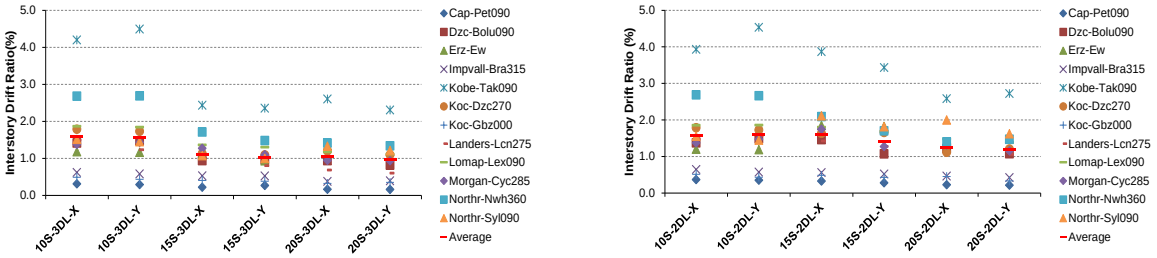

a) b)

Fig.6. Interstory drift ratios of 10-, 15- and 20-storey buildings as linear modelled 3D and 2D (%)

Figure 7 compares the average roof and interstory drift ratios of 2D and 3D models to see how 2D linear models reflect 3D linear models. The figure obviously indicates that the 2D linear models of 10-storey buildings perfectly represent their 3D models. Although the 2D models of 20-storey models are quite reasonable, the 2D models of 15-storey estimate about 40% higher demands compared to the 3D models. The comparison of 2D and 3D model estimates obviously shows that the 2D linear models reflect their 3D models for 10- and 20-storey buildings. However, it is difficult to say similar observation for 15-storey buildings.

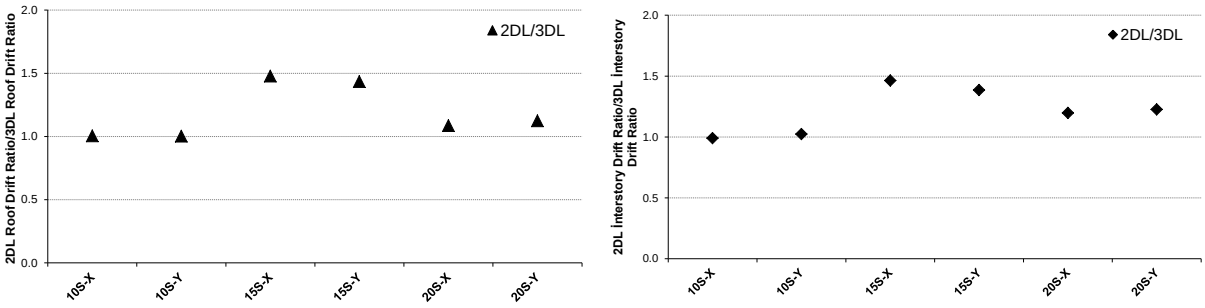

a) b)

Fig.7. Comparison of roof and interstory drift ratios of 10-, 15- and 20-storey buildings for linear 2D and 3D models

The floors at which the maximum interstory drift ratios (IDR) were determined for linear 2D and 3D models of 10-, 15- and 20-storey buildings. In this context, primarily the models were represented by 5-story groups and then the frequency of occurrence for the floor where the maximum IDR occurs is calculated in percent as shown in Figure 8. These values were given as the ratio that the number of occurrences of the maximum relative displacement in the mentioned group to the number of the earthquake records used. Figure 8 illustrates that the 2D and 3D models have similar results indicating good representation of 2D models for their 3D models. When the buildings are evaluated separately, it is seen that the maximum IDR is concentrated in the lower floors of the 10-story buildings, in the middle floors of the 15-story buildings, and in the lower and upper floors of the 20-story buildings. The maximum IDR observed at the upper stories for the buildings with no shear walls can be explained with the reduction in column sizes at the upper stories, the decrease in effective section stiffness due to lower column axial loads and forward directivity effect of the ground motion records used in the study [8, 9].

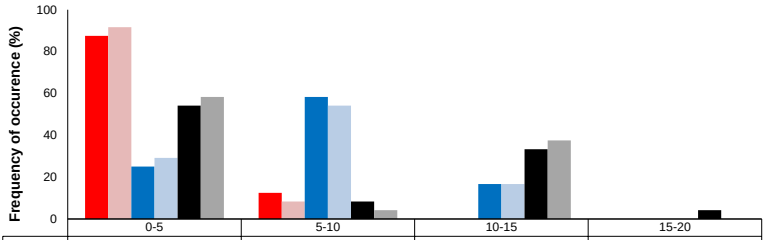

	0-5	5-10	10-15	15-20
10S-2DL	87.50	12.50		
10S-3DL	91.67	8.33		
15S-2DL	25.00	58.33	16.67	
15S-3DL	29.17	54.17	16.67	
20S-2DL	54.16	8.33	33.33	4.17
20S-3DL	58.33	4.17	37.50	

Fig.8. Location of maximum interstory drift ratio for linear 10-, 15- and 20-storey building models

The results of linear and nonlinear time history dynamic analyses are compared for the roof and interstory drift ratios in order to visualize success of linear models in estimating nonlinear demands of RC buildings. Tables 5 and 6 lists nonlinear roof and interstory drift ratio demands for 2D and 3D models. Figure 9a compares the average roof drift ratio of linear and nonlinear models. The average roof drift demands obtained with linear models are normalized by that obtained using corresponding nonlinear models. It is obvious that linear models provide higher demand estimates than their corresponding nonlinear models. The 2D linear 10-storey building model represents reasonably well its nonlinear model while the 3D linear 15- and 20-storey building models provides better demand estimates. It should be kept in mind that the dominant vibration periods of 2D and 3D models of 10-storey building are very close while there are differences in dominant vibration periods of 2D and 3D models of 15- and 20-storey buildings. The better representation of nonlinear model for 10-storey buildings can be attributed to having closer vibration periods. Similar trends are also observed for the interstory drift ratios as seen in Figure 9b.

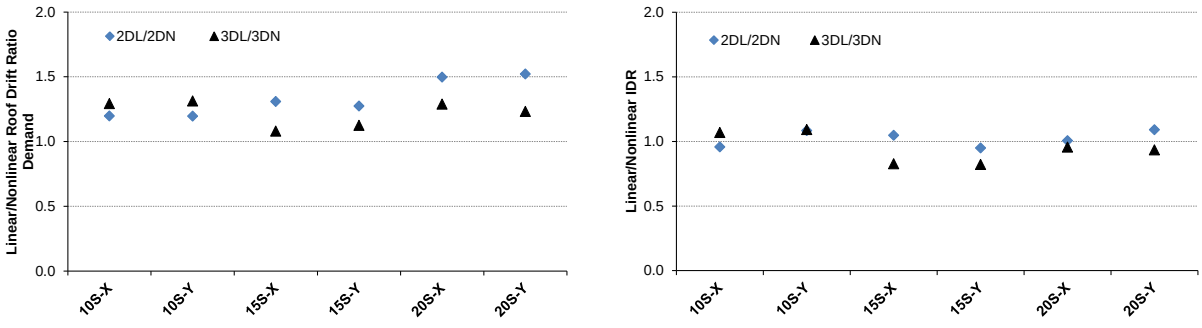

a) b)

Fig.9. Comparison of average roof and interstory drift ratio demands for linear and nonlinear models

The estimates of 2D and 3D linear and 2D nonlinear models were also compared to that of 3D nonlinear model in order to visualize success of linear and 2D nonlinear models in seismic demand estimates of RC buildings as shown in Figure 11. It is obvious that the 2D linear models gives higher demand estimates having 30 to 50% higher estimates compared to the 3D nonlinear models. In general, 2D nonlinear models are the best representation of 3D nonlinear models.

Table 5. Roof drift ratio demands of 10-, 15- and 20-storey nonlinear building models (%)

Earthquake	10-storey building				15-storey building				20-storey building			
	2D-N		3D-N		2D-N		3D-N		2D-N		3D-N	
	X	Y	X	Y	X	Y	X	Y	X	Y	X	Y
Cap-Pet090	0.16	0.16	0.15	0.16	0.09	0.09	0.09	0.09	0.07	0.08	0.06	0.07
Dzc-Bolu090	0.62	0.68	0.66	0.75	0.64	0.61	0.54	0.50	0.32	0.29	0.45	0.43
Erz-Ew	0.92	1.02	0.88	0.84	0.88	0.85	0.60	0.60	0.51	0.52	0.62	0.60
Impvall-Bra315	0.43	0.35	0.46	0.39	0.34	0.35	0.31	0.30	0.24	0.23	0.26	0.28
Kobe-Tak090	1.41	1.39	1.70	1.95	1.19	1.18	1.09	1.03	0.80	0.78	0.87	0.90
Koc-Dzc270	1.24	1.11	1.18	0.87	0.69	0.71	0.76	0.74	0.41	0.46	0.52	0.62
Koc-Gbz000	0.34	0.27	0.32	0.21	0.29	0.28	0.24	0.24	0.19	0.23	0.20	0.21
Landers-Lcn275	1.11	1.07	1.07	0.95	1.12	0.94	0.60	0.57	1.16	0.77	0.81	0.65
Lomap-Lex090	1.68	1.54	1.19	1.20	1.11	1.11	0.99	0.57	0.67	0.80	0.78	0.84
Morgan-Cyc285	0.93	1.12	0.87	0.88	0.59	0.61	0.57	0.56	0.44	0.46	0.44	0.46
Northr-Nwh360	1.18	1.11	0.85	0.86	1.13	1.08	0.84	0.83	0.82	0.75	0.79	0.76
Northr-Syl090	1.57	1.56	0.89	0.92	0.88	0.81	0.95	0.94	0.58	0.51	0.61	0.63
Maximum	1.68	1.56	1.70	1.95	1.19	1.18	1.09	1.03	1.16	0.80	0.87	0.90
Minimum	0.16	0.16	0.15	0.16	0.09	0.09	0.09	0.09	0.07	0.08	0.06	0.07
Average	0.97	0.95	0.85	0.83	0.75	0.72	0.63	0.58	0.52	0.49	0.53	0.54

Table 6. Interstory drift ratio demands of 10-, 15- and 20-storey nonlinear building models (%)

Earthquake	10-storey building				15-storey building				20-storey building			
	2D-N		3D-N		2D-N		3D-N		2D-N		3D-N	
	X	Y	X	Y	X	Y	X	Y	X	Y	X	Y
Cap-Pet090	0.37	0.35	0.31	0.31	0.33	0.29	2.53	2.93	0.17	0.19	0.16	0.16
Dzc-Bolu090	1.52	1.27	1.22	1.38	1.67	1.56	1.21	1.24	0.85	0.74	1.02	0.94
Erz-Ew	1.70	1.66	1.52	1.34	1.90	1.91	1.45	1.38	1.30	1.39	1.45	1.45
Impvall-Bra315	0.62	0.54	0.63	0.58	0.60	0.57	0.53	0.52	0.48	0.39	0.38	0.39
Kobe-Tak090	2.37	2.08	2.63	3.11	2.34	2.37	2.48	2.33	1.83	1.52	1.45	1.63
Koc-Dzc270	1.99	1.63	1.86	1.45	1.42	1.52	1.43	1.44	0.85	0.85	0.86	1.02
Koc-Gbz000	0.56	0.45	0.51	0.29	0.49	0.43	0.40	0.38	0.48	0.33	0.36	0.36
Landers-Lcn275	1.77	1.71	1.73	1.58	1.35	1.21	0.97	0.98	5.98	2.60	3.55	1.54
Lomap-Lex090	2.55	2.19	2.05	1.93	2.39	2.41	1.91	0.98	1.48	1.57	1.29	1.46
Morgan-Cyc285	1.80	1.81	1.55	1.50	1.30	1.34	1.17	1.21	1.18	0.98	0.88	0.85
Northr-Nwh360	1.98	1.60	1.59	1.58	2.37	2.42	1.67	1.73	2.86	2.00	1.85	1.41
Northr-Syl090	2.25	2.37	1.49	1.39	2.17	1.89	1.65	1.71	2.60	1.75	2.29	1.45
Maximum	2.55	2.37	2.63	3.11	2.39	2.42	2.53	2.93	5.98	2.60	3.55	1.63
Minimum	0.37	0.35	0.31	0.29	0.33	0.29	0.40	0.38	0.17	0.19	0.16	0.16
Average	1.62	1.47	1.42	1.37	1.53	1.49	1.45	1.40	1.67	1.19	1.30	1.06

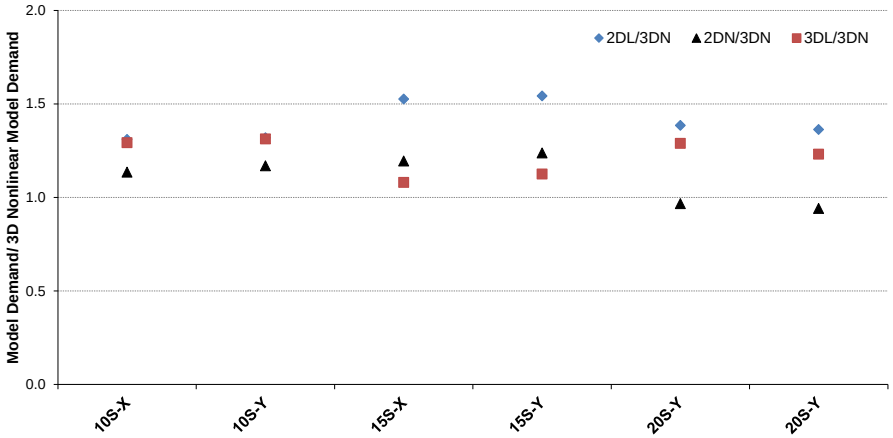

Fig.11. The ratio of displacement demands obtained from models to 3D nonlinear displacement demand

5. Observations and results

This study compared displacement demands obtained from linear and nonlinear time history analyses of 2D and 3D models to investigate how 2D models reflect 3-D models. The estimates of 2D and 3D linear and 2D nonlinear models were also compared to that of 3D nonlinear model in order to visualize success of linear and 2D nonlinear models in seismic displacement estimates of RC buildings. A total of 288 dynamic analyses were performed with 12 different earthquakes records taking into account the two principal directions of 10-, 15- and 20-storey buildings. The observations and outcomes are summarized below:

- The roof and interstory drift demands illustrate that the 10-storey building models have the highest demand ratios and scatter. The comparison of 3D and 2D models clearly points out that the 2D models have higher scatters.
- The comparison of average roof and interstory drift ratios for 2D and 3D models obviously indicates that the 2D linear models reflects their 3D models reasonably well for 10- and 20-storey buildings. However, it is difficult to say similar observation for 15-storey buildings. The differences between 2D and 3D models in demands estimates are about 0%, %50 and 12% for 10-, 15- and 20-storey buildings, respectively.
- The maximum interstory drift ratios were concentrated at lower floors of 10-storey buildings, at the middle floors of 15-storey buildings, and at the lower or upper floors of 20-storey buildings. This observation indicates that as the number of storey increases, it is difficult to estimate location of the floor with maximum interstory drift.
- The results of linear and nonlinear time history dynamic analyses are compared for the roof and interstory drift ratios in order to visualize success of linear models in estimating nonlinear demands of RC buildings. The average roof and interstory drift demands obtained with linear models are normalized by that obtained using corresponding nonlinear models. The results show that linear models provide higher demand estimates than their corresponding nonlinear models. The 2D linear 10-storey building model represents reasonably well its nonlinear model while the 3D linear 15- and 20-storey building models provides better demand estimates. It should be kept in mind that the dominant vibration periods of 2D and 3D models of 10-storey building are very close while there are differences in dominant vibration periods of 2D and 3D models of 15- and 20-storey buildings. The better representation of nonlinear model for 10-storey buildings can be attributed to having closer vibration periods.

In general, the outcomes of the current study imply that 2D representation of 3D models needs careful modelling. The buildings are usually designed according to the related earthquake code considering both gravity and seismic loads. Then, an interior frame is used for 2D modelling. The periods of 3D and 2D models need to be closer in order to have proper representation. Another observation is that the 2D linear elastic models do not properly represent the 3D nonlinear models. Thus, it is recommended to use 3D models when linear modelling is preferred. Since the 2D nonlinear models represent reasonably well their 3D nonlinear ones, the 2D modelling can be preferred for the buildings with no irregularity due to extensive labor and time required for 3D nonlinear models.

References

[1] SAP2000 V-19 CSI. Integrated finite element analysis and design of structures basic analysis reference manual, Berkeley, USA.

[2] DBYBHY-2007, Deprem bölgelerinde yapılacak binalar hakkında yönetmelik, Bayındırlık ve İskan Bakanlığı, Ankara, 2007.

[3] FEMA-356, Prestandard and commentary for seismic rehabilitation of buildings, Report No. FEMA-356, Federal Emergency Management Agency, Washington, D.C., 2000.

[4] Mander, J.B., Priestley, M.J.N. and Park, R., Theoretical stress-strain model for confined concrete. *ASCE*, 114(8), 1804-1826, 1988.

[5] İnel, M., Özmen, Hayri B., Effects of plastic hinge properties in nonlinear analysis of reinforced concrete building, *Engineering Structures*, 28(11):1494-1502, 2006.

[6] SEMAp, Sargı etkisi modelleme analiz programı, 2008, Tubitak proje no: 105M024.

[7] Fardis, M.N., Biskinis D.E., Deformation of RC members, as controlled by flexure or shear, *In: proceedings of the international symposium honoring Shunsuke Otani on performance-based engineering for earthquake resistant reinforced concrete structures*, 2003.

[8] İnel, M., Çelik, S., Özmen, Hayri B., Önür, Ö., İleri yönlenmeli deprem kayıtları etkisindeki mevcut betonarme binaların deplasman taleplerinin doğrusal elastik olmayan zaman tanım alanında analizle değerlendirilmesi, *Yedinci Ulusal Deprem Mühendisliği Konferansı,* İstanbul, Türkiye, 2011.

[9] İnel, M., Önür, Ö., Özmen, Hayri B., Çelik, S., İleri yönlenmeli deprem kayıtları etkisindeki mevcut betonarme binaların deplasman taleplerinin doğrusal elastik zaman tanım alanında analizle değerlendirilmesi, *Yedinci Ulusal Deprem Mühendisliği Konferansı,* İstanbul, Türkiye, 2011.

[10] Bray, Jonathan D., Rodriguez-Marek, A., Characterization of forward-directivity ground motions in the near-fault region, *Soil Dynamics and Earthquake Engineering*, 815-828, 2004.

[11] Cao, V.V. and Ronagh, H.R., Correlation between seismic parameters of pulse-type motions and damage indices of low-rise reinforced concrete frames, *Soil Dynamics and Earthquake Engineering*, 66, 102-112, 2014.

[12] Sommerville, P.G., Engineering characteristics of near fault ground motion, *SMIP Seminar Proceedings,* California, 1989.

[13] Sommerville, P.G., Smith, N.F., Graves, R.W. and Abrahamson N.A, Modifications of empirical strong ground motion attenuation relations to include the amplitude and duration effects of rupture directivity, *Seismological Resarch Letters,* 68(1), 1997.

[14] PEER, http://peer.berkeley.edu

International Journal of Engineering & Applied Sciences (IJEAS)
Vol.9, Issue 4 (2017) 28-41
http://dx.doi.org/10.24107/ijeas.336621
Int J Eng Appl Sci 9(4) (2017) 28-41

Exact Radial Natural Frequencies of Functionally Graded Hollow Long Cylinders

Vebil Yıldırım

Department of Mechanical Engineering, University of Cukurova, 01330, Adana, Turkey
E-mail address: vebil@cu.edu.tr

ORCID numbers of authors:
0000-0001-9955-8423

Received date: August 2017
Accepted date: December 2017

Abstract

In this work the exact free axisymmetric pure radial vibration of hollow infinite cylinders made of hypothetically functionally power-graded materials having identical inhomogeneity indexes for both Young's modulus and the material density is addressed. The equation of motion is obtained as a linear second-order Bessel's ordinary differential equation with constant coefficients based on the axisymmetric linear elasticity theory. For traction free boundaries, a closed form frequency equation is offered. After verifying the present results for cylinders made of both isotropic and homogeneous materials, and isotropic functionally graded materials, an extensive parametric study is carried out to investigate the influences of both the thickness and inhomogeneity indexes on the natural frequencies. Results are presented in both graphical and tabular forms. It was revealed that the fundamental frequency in the radial mode is principally affected from the inhomogeneity parameters than the higher ones. However, the natural frequencies except the fundamental ones are dramatically affected from the thickness of the cylinder. As the thickness decreases, the natural frequencies considerably increase. It is also revealed that, there is a linear relationship between the fundamental frequency and others in higher modes.

Keywords: Free vibration, natural frequency, thick-walled hollow cylinder, functionally graded.

1. Introduction

Vibration of thin/thick-walled cylinders is of great significance in many engineering applications such as pressure vessel, heat exchangers, nuclear reactor containments, various pipes and tubes. Pioneering studies concerning the vibration of cylinders date back late of 1800s. One of the earliest works on the vibration of cylinders was carried out by Chree [1]. Using the linear three dimensional elasticity theory, Greenspon [2] studied the flexural vibrations of infinitely long traction free hollow thick-walled cylinders. Gazis [3] studied the vibration of infinitely long traction free hollow cylinders on the basis of three dimensional elasticity theory. Gladwell and Tahbildar [4] solved the problem of axisymmetric vibrations of cylinders with the help of the finite-element method. Gladwell and Vijay [5] also analyzed the vibration of free finite length circular cylinders based on the finite element approach. Hutchinson [6] first handled the vibrations of finite length rods and solid cylinders on the basis of linear 3D elasticity and offered a semi-analytical highly accurate method to solve the problem. Then, Hutchinson and El-Azhari [7] applied the same method for the vibrations of free hollow finite length circular cylinders. By employing the energy method based on the 3D theory of elasticity, Singal and Williams [8] studied theoretically and experimentally the vibrations of thick hollow cylinders and rings. The axisymmetric stress-free vibration of a thick elastic cylinder has been studied under plane strain conditions by Gosh [9]. Gosh [9] obtained the solution for forced vibration by using the Laplace transform and presented natural frequency and dynamic stresses for various types of loading, Poisson's

ratio and aspect ratios of the cylinder. Leissa and So [10], and So and Leissa [11] studied three-dimensional analysis of the vibrations of free and cantilevered solid cylinders using simple algebraic polynomials in the Ritz method. Liew et al. [12] investigated the free vibrations of stress free hollow cylinders of arbitrary cross-section based on the three dimensional energy displacement expressions. Hung et al. [13] considered the free vibration of cantilevered cylinders. Wang and Williams [14] presented vibrational modes of thick-walled cylinders of finite length based on the finite element method. On the basis of linear 3D theory of elasticity, and by using the Ritz method and Chebyshev polynomials, Zhou et al. [15] worked on the vibration analysis of solid and hollow circular cylinders including rods and curved panels. In this general semi-analytical series solution having high accuracy and good convergence, offered by Zhou et al. [15], the technique of variables separation is developed for various boundary conditions. Mofakhami et al. [16] studied the free vibration of cylinders with finite length under fixed-fixed and free-free boundaries based on the solutions of infinite cylinders and the technique of separation of variables. Abbas [17] treated with the free vibration of a poroelastic hollow cylinder. Yahya and Abd-Alla [18] considered pure radial vibrations in an isotropic elastic hollow cylinder with rotation.

As time progresses and engineers familiarize themselves with new advanced materials such as anisotropic, functionally graded, carbon nanotube composites, studies have focused on the vibration problems of cylinders made of such advanced materials. From those Nelson et al. [19] worked on vibration and waves in laminated orthotropic circular cylinders. Vibration of anisotropic composite cylinders is addresses by Huang and Dong [20]. Yuan and Hsih [21] investigated three dimensional wave propagation in composite cylindrical shells. By using the Ritz method, Kharouf and Heyliger [22] presented a numerical method for finding approximate solutions to static and axisymmetric vibration problems for piezoelectric cylinders, including those composed of more than one material. Markus and Mead [23-24] studied both axisymmetric and asymmetric wave motion in orthotropic cylinders. Ding et al. [25-26] studied elasto-dynamic and thermoelastic-dynamic problems of a non-homogeneous orthotropic hollow cylinders.

As to the functionally graded materials (FGM), Heyliger and Jilani [27] studied the free vibrations of inhomogeneous elastic cylinders and spheres. By using strains-displacement relations from Love's shell theory and the eigenvalue governing equation from Rayleigh-Ritz method, Loy et al. [28] presented a study on the vibration of cylindrical shells made of a functionally graded material (FGM) composed of stainless steel and nickel. The properties are graded in the thickness direction according to a volume fraction power-law distribution in Loy et al's [28] study. Their results showed that the frequency characteristics are similar to that observed for homogeneous isotropic cylindrical shells and the frequencies are affected by the constituent volume fractions and the configurations of the constituent materials. Han et al. [29] presented an analytical-numerical method for analyzing characteristics of waves in a cylinder composed of functionally graded material (FGM) by dividing the FGM cylinder into a number of annular elements with three-nodal-lines in the wall thickness. Han et al. [29] assumed a linear variation of material properties along the thickness direction and used the Hamilton principle to develop the dispersion equations for the cylinder. Their numerical results demonstrated that the ratio of radius to thickness has a stronger influence on the frequency spectra in the circumferential wave than on that in the axial wave. Patel et al. [30] studied the free vibration analysis of functionally graded elliptical cylindrical shells based on the higher-order theory. Pelletier and Vel [31] studied analytically the steady-state thermoelastic response of functionally graded orthotropic cylindrical shells. Arciniega and Reddy [32] considered a large deformation analysis of functionally graded shells. Yang and Shen [33] investigated the free vibration of shear deformable functionally graded cylindrical panels. Jianqiao et al. [34] dealt with wave propagation in non-homogeneous magneto-electro-elastic hollow cylinders. Abd-Alla et al. [35] studied influences of the inhomogeneity on the composite infinite cylinder of isotropic material. Based on the first-order shear

deformation theory and linear elasticity, Tornabene et al. [36] studied the dynamic behavior of functionally graded moderately thick conical, cylindrical shells and annular plates via the generalized differential quadrature (GDQ) method. They considered two different power-law distributions for the ceramic volume fraction. Keleş and Tutuncu [37] analytically performed free and forced vibration analyses of power-law graded hollow cylinders and spheres. Although their subject matters are out of the present study, it may be useful to cite some studies concerning the vibration of cylinders and cylindrical shells which are functionally graded with state-of-the-art technological structural materials [38-40] in the open literature.

As seen from the above literature survey, vibration problems of solid/hollow cylinders made of functionally graded materials are not studied widely over the time. This was the motivation to the author. As a fundamental work, the present study may be thought of as an extension of Gosh's [9] study to traction free cylinders made of isotropic functionally graded materials. In the present study, to achieve an analytical solution for natural frequencies in purely radial modes, the inhomogeneity indexes of both elasticity modulus and Poisson's ratio are assumed to be identical by necessity. As stated in the related section, otherwise, it is not possible to get a closed form solution. In these cases, the employment of any numerical procedure becomes compulsory. One of the aims of the present study is to have a rough idea about the general response of such cylinders to the free vibration before numerically treatment of the problem. In the parametric study, almost all the variables which substantially influence on the natural frequencies are considered except the effect of Poisson's ratio. In Gosh's study [9] the effect of Poisson's ratios on the natural frequencies was clearly disclosed. The numerical results given here may also be served as a benchmark solution to some advanced numerical studies.

2. Clarification of the Problem

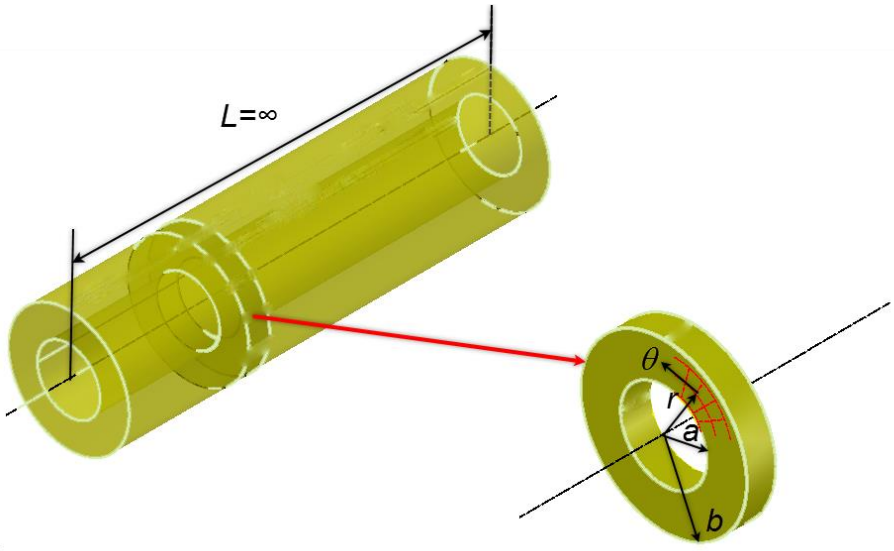

Fig. 1. Geometry of a cylinder

Let's consider a thick-walled hollow cylinder with inner radius a and outer radius b (Fig. 1). Under axisymmetric conditions, relationships between strain and displacement are written in polar coordinates as

$$\varepsilon_r = \frac{du_r}{dr} \quad ; \quad \varepsilon_\theta = \frac{u_r}{r} \tag{1}$$

where the radial unit strain and the circumferential unit strain are symbolized by ε_r , and ε_θ, respectively. In Eq. (1), the radial displacement is represented by u_r. If σ_r , and σ_θ signify the radial stress and the hoop stress, respectively, then Hooke's law for an infinite cylinder made of an isotropic and homogeneous linear elastic material is given by

$$\sigma_r = C_{11}(r)\,\varepsilon_r + C_{12}(r)\,\varepsilon_\theta$$
$$\sigma_\theta = C_{12}(r)\,\varepsilon_r + C_{11}(r)\,\varepsilon_\theta \tag{2}$$

Where under plain strain assumptions

$$C_{11}(r) = E(r)\frac{(1-\nu)}{(1+\nu)(1-2\nu)}$$
$$C_{12}(r) = E(r)\frac{\nu}{(1+\nu)(1-2\nu)} \tag{3}$$

For an isotropic but non-homogeneous FGM material, the material grading rule in the radial direction is assumed to obey the following simple power rule

$$E(r) = E_b\left(\frac{r}{b}\right)^\eta$$
$$\rho(r) = \rho_b\left(\frac{r}{b}\right)^\eta \tag{4}$$

where ρ is the material density. The material inhomogeneity index is denoted by η; E_b and ρ_b are the reference values of the mixture of the material at the outer surface. Poisson's ratios of both graded materials are assumed to be unaffected along the radial direction as in the most of the related realm.

In Eq. (4) those properties do not completely correspond to a physical material since both Young's modulus and density are assumed to have the same inhomogeneity index. To get an analytical solution to the problem, as seen later, taking both inhomogeneity indexes as if they are identical is going to be inevitable because it is not possible to find a closed-form solution in other choices which require exactly numerical solution techniques.

If the body forces are neglected, the equation of motion in the radial direction is written as follows

$$\frac{1}{r}\frac{\partial}{\partial r}(r\sigma_r) - \frac{\sigma_\theta}{r} = \rho\frac{\partial^2 u_r}{\partial t^2} \tag{5}$$

where t is the time. Substitution both Eq. (1) and (2) together with Eq. (4) into Eq. (5) gives

$$\frac{\partial^2 u_r}{\partial r^2} + \left(\frac{1+\eta}{r}\right)\frac{\partial u_r}{\partial r} - \frac{\left(1-\eta\dfrac{C_{12}(r)}{C_{11}(r)}\right)}{r^2}u_r = -\left(\frac{\rho(r)}{C_{11}(r)}\right)\frac{\partial^2 u_r}{\partial t^2} \tag{6}$$

By assuming a harmonic motion, $u_r(r,t) = u_r^*(r)\,e^{i\omega t}$, with an angular velocity $\omega\,(rad/s)$, Eq. (6) gives way to Bessel's differential equations [41-43].

$$-\left(\frac{1-\eta\left(\frac{\nu}{1-\nu}\right)}{r^2}+\Omega^2\right)u_r^*+\left(\frac{1+\eta}{r}\right)\frac{du_r^*}{dr}+\frac{d^2u_r^*}{dr^2}=0 \tag{7}$$

where

$$\Omega=\sqrt{\frac{\rho(r)}{C_{11}(r)}}\omega=\sqrt{\frac{(1-2\nu)(1+\nu)\rho_b}{(1-\nu)E_b}}\omega=\sqrt{\frac{(1-\nu-2\nu^2)\rho_b}{(1-\nu)E_b}}\omega=\frac{\beta}{a} \tag{8}$$

and β is the dimensionless natural frequency. The solution to this equation, Eq. (7), is going to be in the form of [41-43]

$$u_r^*(\mathrm{r})=r^{-\eta/2}\left(C_1J_{\frac{\xi}{2}}(r\Omega)+C_2Y_{\frac{\xi}{2}}(r\Omega)\right) \tag{9}$$

where C_1 and C_2 are arbitrary constants and $J_{\frac{\xi}{2}}(r\Omega)$ and $Y_{\frac{\xi}{2}}(r\Omega)$ denote Bessel's functions of the first and second kind of order $\frac{\xi}{2}$, respectively, and ξ is

$$\xi=\sqrt{4+\eta^2-4\eta\left(\frac{\nu}{1-\nu}\right)}=\sqrt{\frac{(-4-\eta^2+(2+\eta)^2\nu)}{(\nu-1)}} \tag{10}$$

The first derivative of the solution of the radial displacement, u_r^*, and the radial stress, σ_r^*, may be obtained in terms of integration constants, C_1 and C_2, as follows

$$\begin{aligned}\frac{du_r^*}{dr}=&\,r^{-\eta/2}\left(\frac{1}{2}C_1\Omega\left(J_{\frac{\xi}{2}-1}(r\Omega)-J_{\frac{\xi}{2}+1}(r\Omega)\right)+C_2\Omega\left(Y_{\frac{\xi}{2}-1}(r\Omega)-Y_{\frac{\xi}{2}+1}(r\Omega)\right)\right)\\&-\frac{1}{2}\eta r^{-\frac{\eta}{2}-1}\left(C_1J_{\frac{\xi}{2}}(r\Omega)+C_2Y_{\frac{\xi}{2}}(r\Omega)\right)\end{aligned} \tag{11}$$

$$\begin{aligned}\sigma_r^*(r)=&\frac{E_br^{-\frac{\eta}{2}-1}\left(\frac{r}{b}\right)^{\eta}}{2(2\nu^2+\nu-1)}\Big(C_1(\eta-(\eta+2)\nu)J_{\frac{\xi}{2}}(r\Omega)+C_1(\nu-1)r\Omega J_{\frac{\xi-2}{2}}(r\Omega)-C_1(\nu-1)r\Omega J_{\frac{\xi+2}{2}}(r\Omega)\\&+C_2(\eta-(\eta+2)\nu)Y_{\frac{\xi}{2}}(r\Omega)+C_2(\nu-1)r\Omega Y_{\frac{\xi-2}{2}}(r\Omega)-C_2(\nu-1)r\Omega Y_{\frac{\xi+2}{2}}(r\Omega)\Big)\end{aligned}$$

Eqs. (9) and (11) are used when applying the boundary conditions given at both surfaces. The radial displacement vanishes, $u_r^*=0$, at the fixed surface while the radial stress becomes zero, $\sigma_r^*=0$, at the free surface. For instance, if surface-free boundaries are considered then one may obtain

$$\begin{Bmatrix}\sigma_r^*(a)\\ \sigma_r^*(b)\end{Bmatrix}=\begin{bmatrix}A_{1,1} & A_{1,2}\\ A_{2,1} & A_{2,2}\end{bmatrix}\begin{Bmatrix}C_1\\ C_2\end{Bmatrix}=\boldsymbol{A}\begin{Bmatrix}C_1\\ C_2\end{Bmatrix}=\begin{Bmatrix}0\\ 0\end{Bmatrix} \tag{12}$$

To get non-trivial solutions, natural frequencies are determined from the frequencies which make the determinant of the characteristic coefficient matrix, $\boldsymbol{A}$, zero. Considering traction-free boundary conditions for a hollow infinite cylinder made of a hypothetically functionally power-graded material, elements of the coefficient matrices are found in closed forms as follows

$$A_{1,1}=\frac{a^{-\frac{\eta}{2}-1}\left(\frac{a}{b}\right)^{\eta}\left(a(\nu-1)\Omega J_{\frac{\xi-2}{2}}(a\Omega)+(\eta-(\eta+2)\nu)J_{\frac{\xi}{2}}(a\Omega)-a(\nu-1)\Omega J_{\frac{\xi+2}{2}}(a\Omega)\right)E_b}{2(2\nu^2+\nu-1)}$$

$$A_{1,2}=\frac{a^{-\frac{\eta}{2}-1}\left(\frac{a}{b}\right)^{\eta}\left(a(\nu-1)\Omega Y_{\frac{\xi-2}{2}}(a\Omega)+(\eta-(\eta+2)\nu)Y_{\frac{\xi}{2}}(a\Omega)-a(\nu-1)\Omega Y_{\frac{\xi+2}{2}}(a\Omega)\right)E_b}{2(2\nu^2+\nu-1)}$$

$$A_{2,1}=\frac{b^{-\frac{\eta}{2}-1}\left(b(\nu-1)\Omega J_{\frac{\xi-2}{2}}(b\Omega)+(\eta-(\eta+2)\nu)J_{\frac{\xi}{2}}(b\Omega)-b(\nu-1)\Omega J_{\frac{\xi+2}{2}}(b\Omega)\right)E_b}{2(2\nu^2+\nu-1)} \tag{13}$$

$$A_{2,2}=\frac{b^{-\frac{\eta}{2}-1}\left(b(\nu-1)\Omega Y_{\frac{\xi-2}{2}}(b\Omega)+(\eta-(\eta+2)\nu)Y_{\frac{\xi}{2}}(b\Omega)-b(\nu-1)\Omega Y_{\frac{\xi+2}{2}}(b\Omega)\right)E_b}{2(2\nu^2+\nu-1)}$$

3. Authentication of the Formulation

To confirm the present dimensionless frequencies, as a first example, a hollow infinite thin-walled cylinder made of an isotropic and homogeneous material is considered. The first ten natural frequencies are listed in Table 1. As seen from this table there is full agreement with those of Gosh's [9] frequencies.

As a second example a hollow infinite cylinder made of a hypothetically power-law graded material is taken into account. Results, which are all based on the similar procedure, are tabulated in Table 2 in a comparative manner. In this table, $\eta = 0$ corresponds a cylinder made of an isotropic and homogeneous material. It is seen from Table 2 that present results are in good harmony with the others. Figure 2 shows also the determinant-dimensionless frequency curve for $\eta = -5$, and *b/a=2*.

Table 1. Comparison of the present non-dimensional results with the open literature for thin-walled cylinder made of an isotropic and homogeneous material ($\nu = 0.3$; $\frac{b}{a} = 1.02$)

	Present	[9]
β_1	0.894602	0.89
β_2	157.082	157.10
β_3	314.161	314.20
β_4	471.24	471.20
β_5	628.319	628.30
β_6	785.399	785.40
β_7	942.478	942.50
β_8	1099.56	1100.00
β_9	1256.64	1257.00
β_{10}	1413.72	1414.00

Table 2. Comparison of the present FGM results with the open literature (*b/a=2*, $\nu = 0.3$).

	$\eta = -5$		$\eta = -2$		$\eta = 0$			$\eta = 2$		$\eta = 5$	
	Present	[37]	Present	[37]	Present	[9]	[37]	Present	[37]	Present	[37]
β_1	0.752017	0.77435	0.684418	0.69407	0.633263	0.6335	0.63563	0.586987	0.58309	0.537493	0.52547
β_2	3.4389	3.43985	3.20038	3.20181	3.21655	3.218	3.21793	3.3714	3.37244	3.81843	3.81886
β_3	6.44741	6.44802	6.31288	6.31356	6.3193	6.319	6.31999	6.40267	6.40331	6.66528	6.66578
β_4	9.53654	9.53698	9.44462	9.44508	9.44864	9.449	9.44910	9.50494	9.50538	9.6854	9.68579
β_5	12.6508	12.65115	12.5813	12.58161	12.5842	12.58	12.58455	12.6266	12.62695	12.7634	12.76368
β_6	15.7758	15.77602	15.7199	15.72016	15.7222	15.72	15.72249	15.7562	15.75647	15.8661	15.86638
β_7	18.9062	18.90638	18.8595	18.85972	18.8614	18.86	18.86165	18.8898	18.89000	18.9816	18.98183
β_8	22.0397	22.03991	21.9997	21.99987	22.0013	22.00	22.00151	22.0256	22.02583	22.1045	22.10466
β_9	25.1753	25.17544	25.1402	25.14037	25.1416	25.14	25.14180	25.1629	25.16309	25.232	25.23214
β_{10}	28.3122	28.31231	28.281	28.28112	28.2822	28.28	28.28239	28.3012	28.30131	28.3626	28.36273

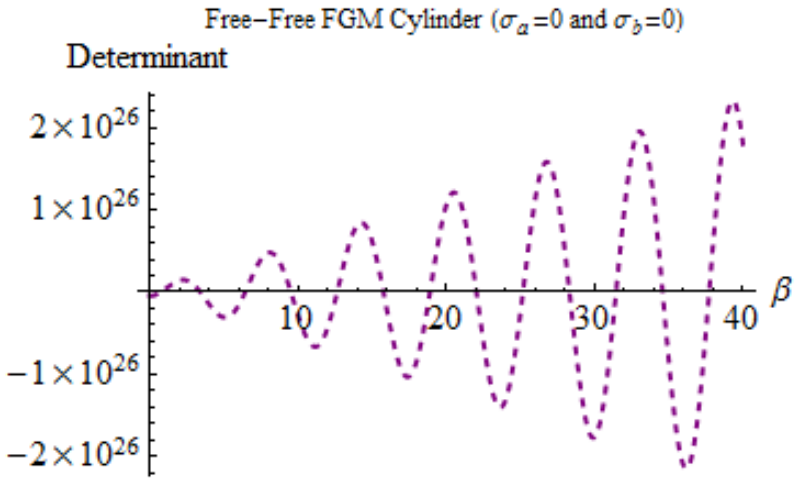

Fig. 2. Determinant-dimensionless frequency curve for $\eta = -5$, and *b/a=2*

4. Effects of the Aspect Ratios and Material Gradients on the Natural Frequencies

In this section a FGM cylinder of $\nu = 0.3$ is considered. The functionally graded material (FGM) is taken to be a hypothetical one exhibiting significant inhomogeneity.

Variation of the natural frequencies with the aspect ratio, which is defined as the ratio of the outer and inner radii, and inhomogeneity indexes is presented in Tables 3 and 4. Table 3 indicates the influence of the aspect ratios and inhomogeneity indexes, which is defined in Eq. (4), on the first ten natural frequencies of a FGM free-free infinite cylinder for $\eta = -5$, $\eta = 0$, $\eta = 7$, and $\eta = 10$. Table 4 shows the influence of the aspect ratios and inhomogeneity indexes on the first three natural frequencies of a FGM free-free infinite cylinder for some inhomogeneity indexes whose values are changed from $\eta = -4$ to $\eta = 5$ with an increase by the unit, except $\eta = 0$.

Table 3. The influence of the aspect ratios and inhomogeneity indexes on the first ten natural frequencies of a FGM free-free infinite cylinder ($\nu = 0.3$) for $\eta = -5,\ \eta = 0, \eta = 7$, and $\eta = 10$

b/a	1.02	1.03	1.04	1.05	1.075	1.10	1.25	1.50	1.75	2.00
					$\eta = -5$					
β_1	0.894748	0.890568	0.886514	0.882583	0.873263	0.864622	0.82422	0.785036	0.764088	0.752017
β_2	157.093	104.74	78.566	62.8643	41.9354	31.4778	12.7008	6.49988	4.45582	3.4389
β_3	314.166	209.449	157.093	125.68	83.7996	62.8628	25.2007	12.6787	8.52027	6.44741
β_4	471.243	314.166	235.628	188.506	125.68	94.2684	37.7445	18.9249	12.6628	9.53654
β_5	628.322	418.884	314.166	251.336	167.564	125.679	50.2996	25.1894	16.8278	12.6508
β_6	785.401	523.603	392.704	314.166	209.449	157.092	62.8591	31.4613	21.0022	15.7758
β_7	942.48	628.322	471.243	376.997	251.335	188.506	75.421	37.737	25.1813	18.9062
β_8	1099.56	733.041	549.782	439.828	293.222	219.92	87.9841	44.0147	29.3632	22.0397
β_9	1256.64	837.761	628.322	502.659	335.109	251.335	100.548	50.2939	33.5468	25.1753
β_{10}	1413.72	942.48	706.861	565.49	376.996	282.75	113.112	56.5739	37.7316	28.3122
					$\eta = 0$					
β_1	0.894602	0.890244	0.885946	0.881708	0.871366	0.861367	0.807616	0.736002	0.67955	0.633263
β_2	157.082	104.724	78.5453	62.8386	41.8978	31.4289	12.595	6.33146	4.25189	3.21655
β_3	314.161	209.442	157.082	125.667	83.7808	62.8383	25.147	12.5902	8.40834	6.3193
β_4	471.24	314.161	235.621	188.498	125.667	94.2521	37.7086	18.8654	12.5868	9.44864
β_5	628.319	418.88	314.161	251.329	167.554	125.667	50.2726	25.1446	16.7704	12.5842
β_6	785.399	523.6	392.7	314.161	209.441	157.082	62.8375	31.4254	20.9562	15.7222
β_7	942.478	628.319	471.24	376.992	251.329	188.498	75.403	37.707	25.1429	18.8614
β_8	1099.56	733.039	549.779	439.824	293.217	219.913	87.9687	43.9891	29.3302	22.0013
β_9	1256.64	837.759	628.319	502.656	335.104	251.329	100.535	50.2714	33.5179	25.1416
β_{10}	1413.72	942.478	706.859	565.487	376.992	282.745	113.1	56.5539	37.7059	28.2822
					$\eta = 7$					
β_1	0.894397	0.88979	0.885153	0.880487	0.868724	0.856851	0.785445	0.676595	0.587642	0.517028
β_2	157.133	104.799	78.6447	62.9616	42.0777	31.6628	13.0978	7.11859	5.18815	4.22088
β_3	314.186	209.479	157.132	125.729	83.8709	62.9557	25.4038	13.0114	8.93897	6.92433
β_4	471.257	314.186	235.654	188.539	125.727	94.3304	37.8805	19.1498	12.9492	9.8673
β_5	628.332	418.899	314.185	251.36	167.599	125.726	50.4017	25.3589	17.0445	12.9023
β_6	785.409	523.615	392.72	314.185	209.478	157.129	62.9409	31.5972	21.1763	15.9782
β_7	942.487	628.332	471.256	377.013	251.359	188.537	75.4891	37.8503	25.3268	19.0754
β_8	1099.57	733.05	549.794	439.842	293.243	219.947	88.0425	44.112	29.488	22.1851
β_9	1256.64	837.768	628.332	502.671	335.127	251.358	100.599	50.379	33.6561	25.3026
β_{10}	1413.72	942.487	706.87	565.501	377.012	282.771	113.158	56.6496	37.8288	28.4255
					$\eta = 10$					
β_1	0.89431	0.889597	0.884814	0.879968	0.86761	0.854972	0.777305	0.66029	0.568707	0.498278
β_2	157.178	104.866	78.733	63.0709	42.2372	31.8695	13.5291	7.74807	5.88568	4.9228
β_3	314.209	209.513	157.176	125.783	83.9511	63.06	25.6302	13.3752	9.38644	7.42197
β_4	471.272	314.208	235.684	188.575	125.781	94.4001	38.0328	19.3995	13.2639	10.2267
β_5	628.343	418.916	314.208	251.387	167.639	125.778	50.5163	25.5481	17.2851	13.1796
β_6	785.418	523.628	392.738	314.207	209.51	157.171	63.0327	31.7493	21.3705	16.203
β_7	942.494	628.343	471.271	377.031	251.386	188.572	75.5657	37.9774	25.4894	19.2641
β_8	1099.57	733.059	549.806	439.857	293.265	219.977	88.1082	44.2211	29.6278	22.3475
β_9	1256.65	837.776	628.343	502.685	335.147	251.385	100.657	50.4746	33.7787	25.4452
β_{10}	1413.73	942.494	706.88	565.513	377.03	282.794	113.209	56.7346	37.9379	28.5524

Table 4. The influence of the aspect ratios and inhomogeneity indexes on the first three natural frequencies of a FGM free-free infinite cylinder ($\nu = 0.3$) for $\eta = -4, -3, -2, -1, 1, 2, 3, 4,$ and 5

b/a	1.02	1.03	1.04	1.05	1.075	1.10	1.25	1.50	1.75	2.00
					$\eta = -4$					
β_1	0.894719	0.890503	0.8864	0.882408	0.872884	0.863973	0.820964	0.775819	0.748964	0.731791
β_2	157.088	104.732	78.5558	62.8516	41.9168	31.4536	12.6484	6.41608	4.35369	3.32657
β_3	314.163	209.446	157.088	125.674	83.7903	62.8507	25.1741	12.6348	8.46472	6.38368
					$\eta = -3$					
β_1	0.89469	0.890438	0.886287	0.882233	0.872505	0.863323	0.81766	0.766172	0.732559	0.709067
β_2	157.084	104.726	78.5486	62.8427	41.9037	31.4366	12.6114	6.35679	4.28103	3.24623
β_3	314.161	209.443	157.084	125.669	83.7837	62.8422	25.1554	12.604	8.42558	6.33871
					$\eta = -2$					
β_1	0.89466	0.890373	0.886173	0.882058	0.872125	0.862671	0.814323	0.756219	0.715205	0.684418
β_2	157.082	104.723	78.5444	62.8375	41.8962	31.4268	12.5902	6.32271	4.23937	3.20038
β_3	314.16	209.441	157.082	125.667	83.78	62.8373	25.1447	12.5862	8.40307	6.31288
					$\eta = -1$					
β_1	0.894631	0.890308	0.88606	0.881883	0.871746	0.862019	0.81097	0.746108	0.697358	0.658769
β_2	157.081	104.722	78.5433	62.8362	41.8943	31.4242	12.5847	6.31423	4.22961	3.19044
β_3	314.16	209.441	157.081	125.666	83.779	62.836	25.1419	12.5816	8.39732	6.30639
					$\eta = 1$					
β_1	0.894573	0.890179	0.885833	0.881534	0.870986	0.860715	0.804279	0.726062	0.662312	0.609035
β_2	157.085	104.728	78.5503	62.8448	41.9069	31.4407	12.6209	6.37414	4.30563	3.2776
β_3	314.162	209.443	157.085	125.67	83.7853	62.8443	25.16	12.6119	8.43609	6.35149
					$\eta = 2$					
β_1	0.894543	0.890114	0.885719	0.881359	0.870607	0.860065	0.800975	0.71644	0.646107	0.586987
β_2	157.089	104.734	78.5584	62.8549	41.9216	31.4598	12.6626	6.44176	4.38954	3.3714
β_3	314.164	209.447	157.089	125.675	83.7927	62.8538	25.181	12.6466	8.48039	6.40267
					$\eta = 3$					
β_1	0.894514	0.890049	0.885606	0.881184	0.870228	0.859416	0.797719	0.707266	0.631274	0.567654
β_2	157.095	104.742	78.5695	62.8686	41.9418	31.4861	12.7197	6.5335	4.50181	3.49505
β_3	314.167	209.451	157.094	125.682	83.8028	62.867	25.2099	12.6943	8.54101	6.47243
					$\eta = 4$					
β_1	0.894485	0.889984	0.885492	0.88101	0.86985	0.85877	0.794525	0.698641	0.618006	0.5512
β_2	157.102	104.753	78.5837	62.8862	41.9675	31.5196	12.792	6.64832	4.64025	3.64521
β_3	314.17	209.456	157.102	125.691	83.8156	62.8838	25.2466	12.7548	8.61761	6.56019
					$\eta = 5$					
β_1	0.894456	0.88992	0.885379	0.880835	0.869474	0.858127	0.791408	0.690634	0.606359	0.537493
β_2	157.111	104.766	78.601	62.9076	41.9987	31.5602	12.8794	6.78502	4.80243	3.81843
β_3	314.175	209.463	157.11	125.702	83.8313	62.9041	25.2912	12.828	8.70979	6.66528

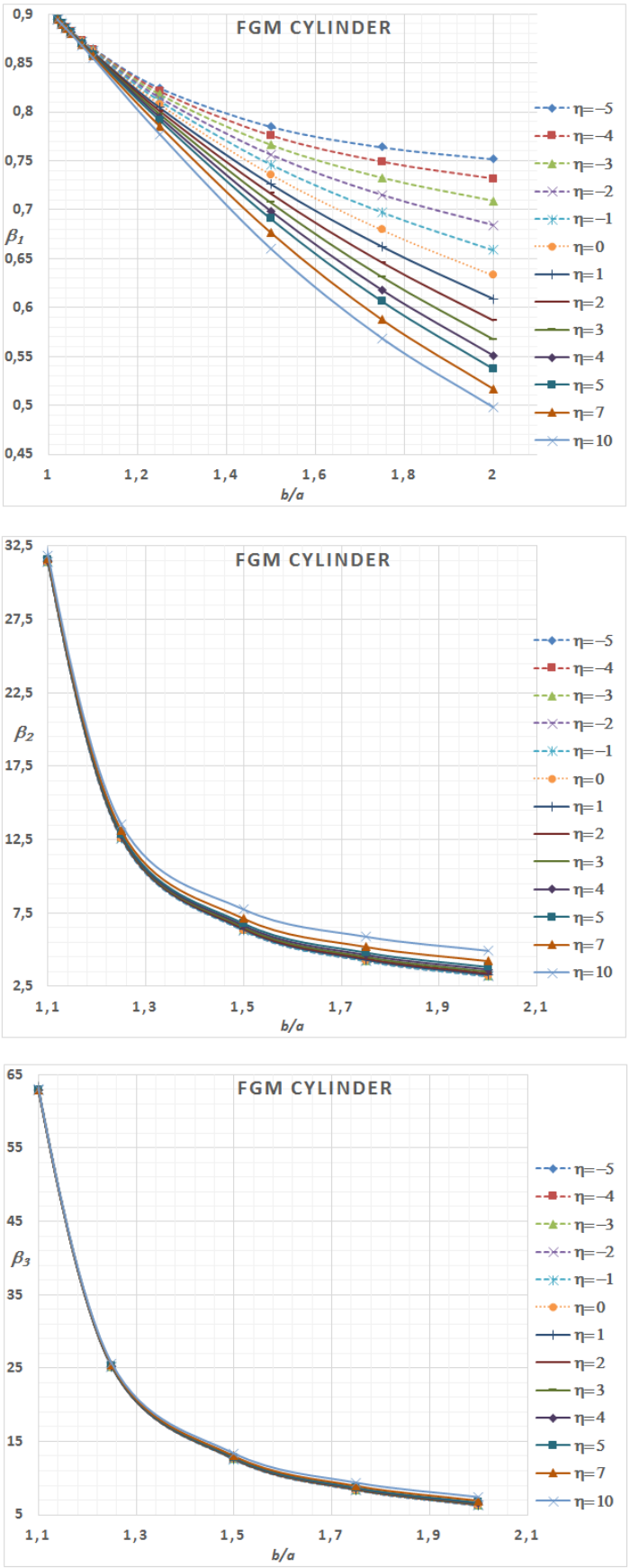

Fig. 3. Variation of the first three natural frequencies with the inhomogeneity indexes for $1.1 \leq b/a \leq 2$ and $-5 \leq \eta \leq 10$.

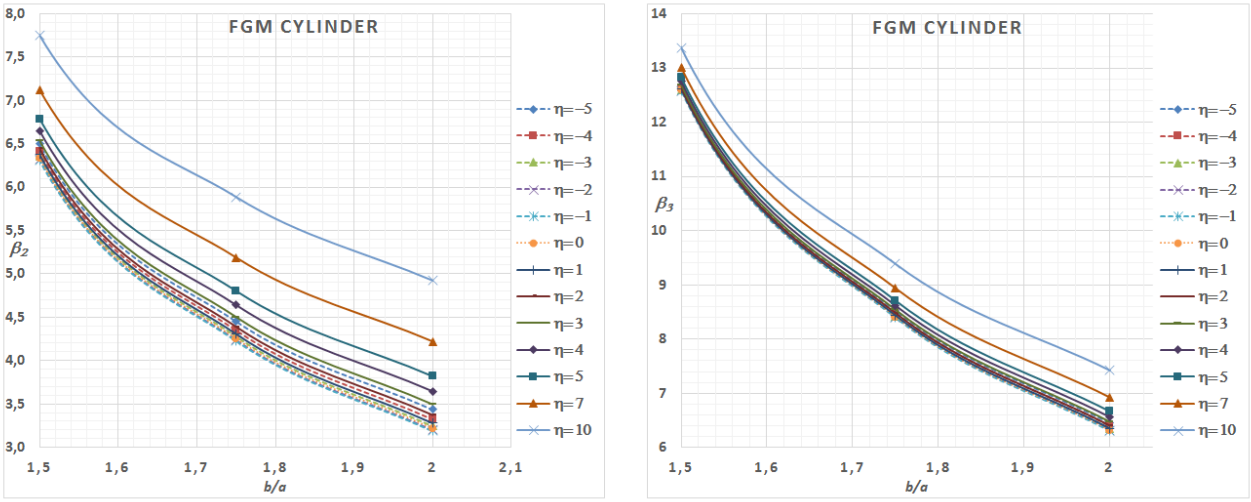

Fig. 4. Variation of the second and the third natural frequencies with the inhomogeneity indexes for $1.5 \leq b/a \leq 2$ and $-5 \leq \eta \leq 10$.

Both Table 3 and Table 4 suggest that as the thickness increases, the dimensionless natural frequencies decrease. This response is slightly observed for fundamental frequencies. However, there is sharply decrease in frequencies of higher modes as the thickness build up.

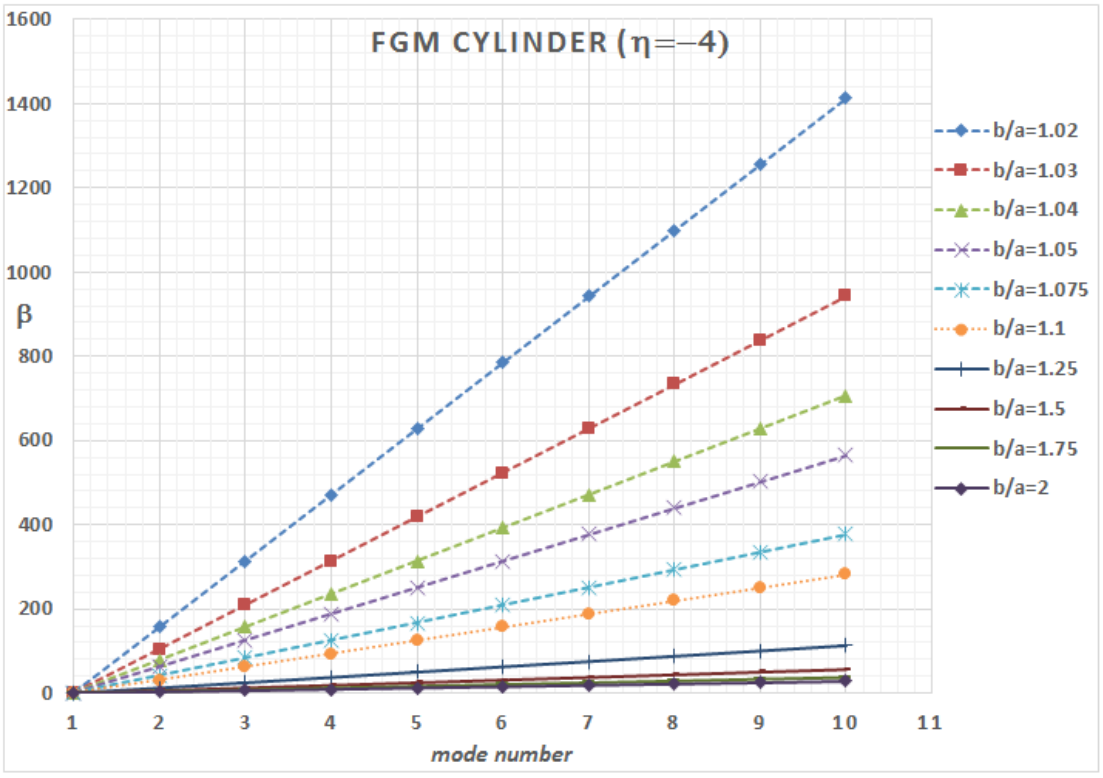

Fig. 5. The relationship between the frequencies of the same cylinder

For the dimensionless frequencies, the degree of to be influenced from the change of inhomogeneity indexes is rather slow. This is demonstrated in Figs. 3 and 4. Figure 3 shows the variation of the first three natural frequencies with the inhomogeneity indexes for $1.1 \leq b/a \leq 2$ and $-5 \leq \eta \leq 10$. Variation of the second and the third natural frequencies with the inhomogeneity indexes for $1.5 \leq b/a \leq 2$ and $-5 \leq \eta \leq 10$ is illustrated in Fig. 4. As seen from Fig. 3, the fundamental frequencies are more affected from the change in the inhomogeneity index. In the interval of the aspect ratio, $1.1 \leq b/a \leq 1.5$, it is almost impossible to observe the variation of natural frequencies in higher modes with the change in the inhomogeneity index. However, as in Fig. 4, this may be clearly observed for $1.5 \leq b/a \leq 2$ for the second and third frequencies.

In this study, it is also revealed that, there is a linear relationship between the pure radial fundamental frequency and others in higher modes of the same cylinder for all inhomogeneity indexes and aspect ratios as seen from Fig. 5.

5. Concluding Remarks

In the present study, the free vibration of hypothetically power-law graded hollow infinite stress-free cylinders is analytically studied to investigate the influences of inhomogeneity indexes and aspect ratios, whose figures are chosen in the broadest possible range of values that can be used in practice, on the natural frequencies. The following conclusions are drawn:

- The fundamental frequency is mainly affected from the variation of the inhomogeneity index than those of other higher frequencies. This may be acceptable as plausible because of huge differences between the fundamental and higher frequencies. For example, for *b/a*=1.02 the natural frequency in the second mode is more than 150 times the fundamental frequency, however it is around four times the first one for *b/a*=2 (see Tables 3-4).
- The effects on the frequencies of the changes in thickness of the cylinder are clearly observed. Increasing thickness produce a substantial decrease in dimensionless frequencies which are particularly in frequencies in higher modes.
- There is also a linear relationship between the frequencies of fundamental and higher modes of the same cylinder.

As stated before, the present results pertaining to the cylinders made of hypothetically FGM materials are obtained by using the same inhomogeneity index for both elasticity modulus and material density. It is a great possibility that there is no such a physical material that provides this feature. For this sense, it may be useful to confirm the present conclusions with physical materials. As mentioned above, this requires the putting numerical solution techniques into practice.

References

[1] Chree, C., The equations of an isotropic elastic solid in polar and cylindrical coordinates, their solutions and applications. *Transactions of the Cambridge Philosophical Society*, 14, 250–309, 1889.

[2] Greenspon, J. E., Flexural vibrations of a thick-walled circular cylinder according to the exact theory of elasticity. *Journal of Aero/Space Sciences*, 27, 1365–1373, 1957.

[3] Gazis, D. C., Three dimensional investigation of the propagation of waves in hollow circular cylinder. *Journal of the Acoustical Society of America*, 31, 568–578, 1959.

[4] Gladwell, G. M., Tahbildar, U. C., Finite element analysis of axisymmetric vibrations of cylinders. *Journal of Sound and Vibration*, 22, 143–157, 1972.
[5] Gladwell, G. M., Vijay, D. K., Natural frequencies of free finite length circular cylinders. *Journal of Sound and Vibration*, 42, 387–397, 1975.
[6] Hutchinson, J. R., Vibrations of solid cylinders. *Journal of Applied Mechanics*, 47, 901–907, 1980.
[7] Hutchinson, J. R., El-azhari, S. A., Vibrations of free hollow circular cylinders. *Journal of Applied Mechanics*, 53, 641–646, 1986.
[8] Singal, R. K., Williams, K. A., Theoretical and experimental study of vibrations of thick circular cylindrical shell and rings. *Journal of Vibration, Acoustics, Stress and Reliability in Design*, 110, 533–537, 1988.
[9] Gosh, A. K., Axisymmetric vibration of a long cylinder. *Journal of Sound and Vibration*, 186(5), 711–721, 1995.
[10] Leissa, A. W., So, J., Accurate vibration frequencies of circular cylinders from three-dimensional analysis. *Journal of the Acoustical Society of America*, 98, 2136–2141, 1995.
[11] So, J., Leissa, A. W., Free vibration of thick hollow circular cylinders from three-dimensional analysis. *Journal of Vibration and Acoustics*, 119, 89–95, 1997.
[12] Liew, K. M., Hung, K. C., Lim, M. K., Vibration of stress free hollow cylinders of arbitrary cross-section. *Journal of Applied Mechanics*, ASME, 62, 718–724, 1995.
[13] Hung, K. C., Liew, K. M., Lim, M. K., Free vibration of cantilevered cylinders: effects of cross-sections and cavities. *Acta Mechanica*, 113, 37–52, 1995.
[14] Wang, H., Williams, K. Vibrational modes of thick cylinders of finite length. *Journal of Sound and Vibration*, 191, 955–971, 1996.
[15] Zhou, D., Cheung, Y. K., Lo, S. H., Au, F. T. K., 3D vibration analysis of solid and hollow circular cylinders via Chebyshev–Ritz method. *Computer Methods in Applied Mechanics and Engineering*, 192, 1575–1589, 2003.
[16] Mofakhami, M. R., Toudeshky, H. H., Hashemi, S. H. H., Finite cylinder vibrations with different end boundary conditions. *Journal of Sound and Vibration*, 297, 293–314, 2006.
[17] Abbas, İ., Natural frequencies of a poroelastic hollow cylinder. *Acta Mechanica*, 186(1–4), 229–237, 2006.
[18] Yahya, G. A., Abd-Alla, A. M., Radial vibrations in an isotropic elastic hollow cylinder with rotation. *Journal of Vibration and Control*, 22(13), 3123–3131, 2016.
[19] Nelson, R. B., Dong, S. B., Kalra, R. D., Vibrations and waves in laminated orthotropic circular cylinders. *Journal of Sound and Vibration*, 18, 429–444, 1971.
[20] Huang, K. H., Dong, S. B., Propagating waves and edge vibrations in anisotropic composite cylinders. *Journal of Sound and Vibration*, 96, 363–379, 1984.
[21] Yuan, F. G., Hsieh, C. C., Three-dimensional wave propagation in composite cylindrical shell. *Composite Structures*, 42, 153–167, 1988.
[22] Kharouf, N., Heyliger, P. R., Axisymmetric free vibrations of homogeneous and laminated piezoelectric cylinders. *Journal of Sound and Vibration*, 174(4), 539-561, 1994.
[23] Markus, S., Mead, D. J., Axisymmetric and asymmetric wave motion in orthotropic cylinders. *Journal Sound Vibration*, 181, 127–147, 1995.
[24] Markus, S., Mead, D. J., Wave motion in a 3-layered, orthotropic isotropic orthotropic composite shell. *Journal Sound Vibration*, 181, 149–167, 1995.
[25] Ding, H. J., Wang, H. M., Chen, W. Q., Elastodynamic solution of a non-homogeneous orthotropic hollow cylinder. *Acta Mechanica Sinica*, 18, 621–628, 2002.
[26] Ding, H. J., Wang, H. M., Chen, W. Q., A solution of a non-homogeneous orthotropic cylindrical shell for axisymmetric plane strain dynamic thermo elastic problems. *Journal of Sound and Vibration*, 263, 815–829, 2003.

[27] Heyliger, P. R., Jilani, A., The free vibrations of inhomogeneous elastic cylinders and spheres. *International Journal of Solids and Structures*, 29(22), 2689-2708, 1992.
[28] Loy, C. T., Lam, J. N., Reddy, J. N., Vibration of functionally graded cylindrical shells. *Int. J. Mech. Sci*. 41, 309–324, 1999.
[29] Han, X., Liu, G. R., Xi, Z. C., Lam, K. Y., Characteristics of waves in a functionally graded cylinder. *Int. Journal for Numerical Methods in Engineering,* 53(3), 653–676, 2002.
[30] Patel, B. P., Gupta, S. S., Loknath, M. S., Kadu, C. P., Free vibration analysis of functionally graded elliptical cylindrical shells using higher-order theory. *Compos. Struct*., 69, 259–270, 2005.
[31] Pelletier, J. L., Vel, S. S., An exact solution for the steady-state thermoelastic response of functionally graded orthotropic cylindrical shells. *Int. J. Solids Struct*., 43, 1131–1158, 2006.
[32] Arciniega, R. A., Reddy, J. N., Large deformation analysis of functionally graded shells. *Int. J. Solids Struct*., 44, 2036–2052, 2007.
[33] Yang, J., Shen, H. S., Free vibration and parametric resonance of shear deformable functionally graded cylindrical panels. *J. Sound Vib*., 261, 871–893, 2007.
[34] Jianqiao, Y., Qiujuan, M., Shan, S., Wave propagation in non-homogeneous magneto-electro-elastic hollow cylinders. *J. Ultrasonic*, 48, 664–677, 2008.
[35] Abd-Alla, A. M., Nofal, T. A., Farhan, A. M., Effect of the non-homogenity on the composite infinite cylinder of isotropic material. *Physics Letters A*, 372, 4861–4864, 2008.
[36] Tornabene, F., Viola, E., Inman, D. J., 2-D differential quadrature solution for vibration analysis of functionally graded conical, cylindrical shell and annular plate structures. *J. Sound Vib.*, 328, 259-290, 2009.
[37] Keleş, İ., Tütüncü, N., Exact analysis of axisymmetric dynamic response of functionally graded cylinders (or disks) and spheres. *Journal of Applied Mechanics*, 78(6), 061014 (7 pages), 2011.
[38] Shen, H. S., Xiang, Y., Nonlinear vibration of nanotube-reinforced composite cylindrical shells in thermal environments. *Comput. Methods Appl. Mech. Engrg*., 213, 196-205, 2012.
[39] Shen, H. S., Xiang, Y., Nonlinear vibration of nanotube-reinforced composite cylindrical panels resting on elastic foundations in thermal environments. *Compos. Struct*., 111, 291-300, 2014.
[40] Moradi-Dastjerdi, R., Foroutan, M., Pourasghar, A., Dynamic analysis of functionally graded nanocomposite cylinders reinforced by carbon nanotube by a mesh-free method. *Mater. Des.*, 44, 256-266, 2013.
[41] Bowman, F., *Introduction to Bessel Functions*, New York, Dover, 1958.
[42] Hildebrand, F. B., *Advanced Calculus for Applications*, Prentice-Hall. Inc. Englewood Cliffs, New Jersey, 1962.
[43] Abramowitz, M., Stegun, I. A. (Eds.), *Handbook of Mathematical Functions with Formulas, Graphs and Mathematical Tables*, 9th printing, New York, Dover, 1972.

International Journal of Engineering & Applied Sciences (IJEAS)
Vol.9, Issue 4 (2017) 42-50
http://dx.doi.org/10.24107/ijeas.342039
Int J Eng Appl Sci 9(4) (2017) 42-50

Estimation of Hydrologic Parameters of Kocanaz Watershed by a Hydrologic Model

Müsteyde Baduna Koçyiğit [a], Hüseyin Akay [b], Ali Melih Yanmaz [c]*

[a,b] Gazi Universitesi Muhendislik Fakultesi Insaat Muhendisligi Bolumu
[c] Orta Dogu Teknik Universitesi Muhendislik Fakultesi Insaat Muhendisligi Bolumu
[*]E-mail address: baduna@gazi.edu.tr

ORCID numbers of authors:
0000-0003-2338-4425[a], 0000-0002-9714-4590[b], 0000-0002-7145-2827[c]

Received date: October 2017
Accepted date: December 2017

Abstract

The main goal of this study is to estimate the hydrologic parameters of Kocanaz watershed located in Western Black Sea Region, using a semi-distributed hydrologic model, Hydrologic Engineering Center – Hydrologic Modelling System (HEC-HMS). In this study, the hydrologic model was set up for two flood events occurred in 2002 and 2013, in which one was used for calibration while the other one was used for validation of the calibrated hydrologic parameters. The watershed was introduced into the model as a single basin. Hydrologic parameters used for transformation from rainfall to runoff and base flow estimations were searched using Nelder and Mead method and calibrated using the peak-weighted root mean square error. The model results were deliberated by statistical indicators such as Nash-Sutcliffe efficiency coefficient (E_{NS}), coefficient of determination (R^2), mass balance error (MBE) and peak flow rate error (PE). The model results were found to be very good for calibration and satisfactory for validation while the peak flow rate was under estimated for both calibration and validation. It can be concluded that small watersheds such as Kocanaz might be modelled as a single basin without sacrificing the estimation capability of the model and increasing the model simulation time. Though, slightly improved peak discharge estimations were obtained in case of using sub basins.

Keywords: Kocanaz, HEC-HMS, calibration, validation, hydrologic model

1. Introduction

A sound design and operation philosophy of hydraulic structures requires either determination of a peak flow rate or a runoff hydrograph to estimate the maximum runoff volume in a catchment area using rainfall data and flood history of the area. In order to improve the understanding of complex hydrologic processes between the amount of rainfall on a basin and the amount of runoff from that basin, many variable parameters such as meteorological, drainage basin and stream channel characteristics need to be considered. Hence, many studies have been carried out to assess these hydrologic processes and try to relate these parameters quantitatively to the discharge. One area of such research includes the usage of hydrologic modelling software such as Precipitation Runoff Modeling System (PRMS), Hydrologic Simulation Model (HYSIM), Model for Urban Stormwater Improvement Conceptualization (MUSIC), Storm Water Management Model (SWMM), Soil and Water Assessment Tool (SWAT), MIKE - SHE and HEC-HMS which is chosen for this research [1-3].

In the process of hydrologic modeling of a basin, firstly calibration of hydrologic parameters are carried out using the rainfall data obtained from meteorological stations situated in or around the basin and the stream discharge values obtained from stream gaging stations for a rainfall event. Then,

those calibrated hydrologic parameters are validated using data of another rainfall or storm data. Hydrological analysis can be performed for short or long term time intervals. Short term hydrological analysis is used to understand the event based hydrological process, such as flooding in the watershed while long term hydrological analysis considers a long time span to estimate probable flooding events occurred in that time span [4, 5].

In the literature, there are many applications of HEC-HMS and other such hydrologic models for both short and long term calibration of hydrologic parameters. For instance, Chu and Steinman [6] investigated the implementation of an effective and accurate hydrologic modeling in case of using fine-scale and coarse-scale hydrologic modeling. HEC-HMS and Watershed Modeling System (WMS) were applied to Mona Lake watershed in west Michigan. The model parameters were first calibrated with fine scale event data adopting 5 minute time steps which was supplied by intensive field data and these calibrated parameters were then used in the continuous hydrologic model with coarser scale of hourly time step. In both hydrologic modeling, surface runoff was simulated and the relationship between the two rainfall-runoff models was analyzed. Outputs of those simulations suggested that fine – scale event modeling was efficient in improving the continuous modeling by providing more accurate and well calibrated parameters. Laouacheria and Mansouri [7] used Watershed Bounded Network Model (WBNM) and HEC-HMS to test the effect of catchment size and time steps on runoff hydrograph shape and to evaluate the catchment reaction to a given rainfall event in the Azzaba City located in the North East of Algeria. Characteristics of the simulated hydrographs were compared with the same characteristics of the same observed hydrographs and statistically analyzed. The results suggested that HEC-HMS provided acceptable simulations in the flood events where WBNM failed to simulate. Kaffas and Hrissanthou [8] also applied HEC-HMS to the basin of Kosynthos River in Norteastern Greece and compared the simulated runoff results with the field discharge measurements. The hydrologic modeling was performed for a relatively long period of time and the parameters of base flow component were determined by calibration. The model outputs showed that this approach for base flow component provided a more realistic assumption for the time variation of base flow. Zhang et al. [2] calibrated the hydrologic parameters for two storm events in Clear Creek, Iowa, USA and then cross validated the parameters using these two storm data to demonstrate the behavior of parameters under different flood conditions. Shahid et al. [9] calibrated hydrologic parameters for different storms and cross validated parameters using those of calibrated hydrologic parameters. Authors found the results with a significant range of reasonable to good. Though studies about improving existing engineering hydrology curricula has been emphasized especially in hydrologic modeling area with increasing availability of hydrologic data over a wide range of scales like remote sensing, only in the last decade application of various hydrologic models to watersheds in Turkey has begun to accelerate. For example Yilmaz et al. [10] used HEC-HMS and Large Basin Runoff Model (LBRM) to simulate snowmelt runoffs of Upper Euphrates Basin in Eastern Turkey for a relatively longer time period by using available data and basin properties. The performance of both models was found to be quite similar so the use of both models was recommended for the investigation of climate change influences on hydrology of the Euphrates Basin. Baloch et al. [11] used Hydrologic Simulation Program-Fortran (HSPF) model for the hydrologic modeling of Koycegiz Watershed in Turkey to investigate the effect of land-use and climate change on the hydrologic regime of the Namnam stream passing through that watershed. Findings of the study suggested that potential land-use changes and climate variability in the watershed would significantly modify the hydrologic regime of Namnam Stream. Akiner and Akkoyunlu [12], used SWAT model to calibrate the hydrologic parameters in Melen Creek and to forecast the flow hydrograph. The results of hydrologic simulations suggested the long term projection of the watershed characteristics. Baduna Kocyigit et al. [3] evaluated the effect of number of sub basins in the estimation of hydrologic parameters and hydrograph at basin outlet and its neighboring ungauged basin. The authors calibrated and cross-validated two flood events dividing the basin into seven different configurations. They used the calibrated hydrologic parameters of two

storms and their averages to validate other four storms. Moreover, the authors estimated the hydrologic parameters of the neighboring ungauged basin. Then, they evaluated sub basin divisions giving the best results. They found that parameters of the whole sub basin estimated the hydrographs of donor and neighboring basins the best and the individual calibrations were more compatible with the hydrographs than those of cross validation.

In this study, HEC-HMS was used for hydrologic modeling of Kocanaz basin located in Northwestern of Turkey to investigate the validation of the calibrated hydrologic parameters to predict the runoff hydrograph of the basin. Hence, the hydrologic parameters of Kocanaz basin are calibrated using a storm data and then validated for another storm event by substituting the calibrated parameters into the validated model.

2. Study Area

In this study, a small basin, Kocanaz, located in the Western Black Sea Region Basin which has 30000 km^2 drainage areas; having 811 mm of annual average rainfall with 9.93 km^3 flow volume is chosen as the study area [13]. Kocanaz Creek which collects water drained from Bartin and Ulus counties is a tributary of Bartin Creek passing through Bartin city center. The maximum and minimum altitudes of Kocanaz Creek considered in this study are 1755 m and 130 m, respectively. The drainage area, basin perimeter and longest flow path are 322.4 km^2, 115.26 km and 37.05 km, respectively. The watershed is generally mountainous and forestry, and consists of agricultural land, pasture, meadow and grasslands. The watershed is very steep with an average slope of 39.4% where the gradient might exceed 360% at several locations. Due to this steep slope, downstream of the basin frequently experiences flash flooding causing agricultural lands to be inundated, motorways to be closed to traffic and infrastructures of the town seriously damaged. Hydrologic soil groups of the basin are determined as C and D using land use and soil maps of the basin. The average curve number of the basin is about 78.5 and this value typically ranges from 70 to 98 locally. These values show that the major part of the rainfall continues as runoff in the watershed. In the basin, there is Kocanaz stream gaging station which is taken as the outlet of the basin in the model study (Fig. 1).

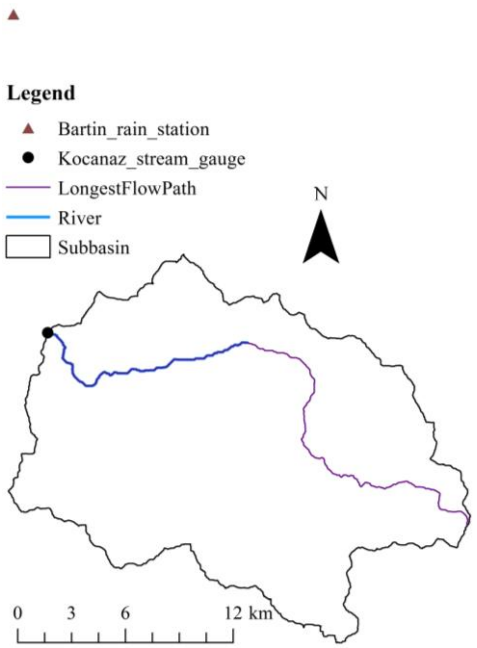

Fig. 1. General sketch of Kocanaz watershed and its main channel, longest flow path, stream gauge and meteorological stations

3. Method

Topographic maps with a scale of 1/25,000 resolution were introduced into ArcGIS 10.1 so digital elevation model (DEM) of the basin was established. The terrain model was created with ArcHydro toolbar and the basin model was produced with HECGeo-HMS 10.1. Of using the terrain model, sub-basins, slope of the basin and the tributaries can be specified. Basin and terrain models were then exported to HEC-HMS to set up the hydrologic model. Precipitation model for the hydrologic model can be obtained using precipitation data in or around the basin operated by State Meteorological Works. Kocanaz stream gauge with D13A039 local name operated by State Water Works (DSI) was taken as the outlet of the basin. Flow data provided by DSI was used to estimate the hydrologic parameters of the basin in hydrologic modeling.

4. Hydrologic Model

HEC-HMS was originally developed to simulate the precipitation-runoff processed of dendritic watershed systems. Later, it was improved to solve significant hydrologic problems including large river basin water supply, flood hydrology and small urban or natural watershed runoff [10]. HEC-HMS includes loss, flow transformation, base flow components for basins and routing processes for streams in the basis of semi-distributed hydrologic model. Furthermore, the model is capable of creating a meteorological model of the basin using precipitation, evaporation, temperature, humidity and radiation data for each sub basin. In the literature, there are many studies about the effect of number of sub basin on the estimation of flow data. Zhang et al. [2], Baduna Kocyigit et al. [3], Ao et al. [14] and Rouhani et al. [15] noted that as the number of sub basins increase, the model results are inversely affected. So, in this study Kocanaz basin was modeled as a single basin in the basin model in HECGeo-HMS.

Precipitation model was created using data of Bartin Meteorological Observation Station located near the basin as shown in Fig. 1. In this model, loss component was ignored as this is thought to be the worst scenario for the watershed, which frequently faces flash flooding. Thus, all the precipitation was assumed to be transformed to runoff. Clark's unit hydrograph and recession method were chosen as the transformation from rainfall to runoff and base flow components, respectively. In Clark's unit hydrograph method, transformation to runoff is calculated using time of concentration (T_c) and storage coefficient (S_c) parameters. In base flow recession method, base flow is computed using initial discharge (Q_0), recession constant (k) and threshold discharge (Q_{ts}). Direct runoff can be computed by subtracting base flow from storm hydrograph.

In this study, values of T_c and S_c for Clark's unit hydrograph method and k and Q_{ts} values were calibrated. Seven target functions and two different search methods were used for optimization of parameters during calibration of HEC-HMS [2]. In this study, parameters were calibrated according to the peak - weighed root mean squared error (PWRMSE) and Nelder – Mead method as objective function and search method, respectively (Eq. 1).

$$\mathrm{PWRMSE} = \sqrt{\frac{\sum (Q_{obs} - Q_{sim})^2 \dfrac{Q_{obs} + Q_{obs,av}}{2Q_{obs,av}}}{N}} \tag{1}$$

where Q_{obs}, Q_{sim} and $Q_{obs,av}$ represent the observed, simulated and average values of the observed discharges, respectively.

Initial values of the parameters to be calibrated in the model must also be introduced into the model. T_c initial value was calculated by SCS (Soil Conservation Service) method (Eq. 2).

$$T_c = \frac{2.587L^{0.8}(\frac{1000}{CN} - 9)^{0.7}}{1900S^{0.5}} \quad (2)$$

where L represents the main channel length (m), CN the curve number, S the basin average slope (%). While L and S values were obtained from basin model, CN values were obtained from hydrologic soil groups and land use maps provided by Republic of Turkey Ministry of Food, Agriculture and Livestock General Directorate of Agricultural Reform.
S_c value can be estimated by Eq. 3. where c is the proportionality coefficient and its value ranges from 8 to 12 for densely forested areas, 1.5–2.8 for predominantly agricultural areas, and 1.1–2.1 for urban areas [9]. In this study the initial value of c was taken to be 1.

$$S_c = cT_c \quad (3)$$

Base flow recession values (Q_b) were computed as in the form of Eq. 4. The observed discharge value at the start of each event was input as Q_0, while the recession constant value was initialized as 0.8, for Q_{ts}, the minimum observed discharge value for the month in which the event occurred [9].

$$Q_b = Q_0 e^{-kt} \quad (4)$$

Model results were deliberated by means of certain criteria used for the evaluation of the outputs obtained in both calibration and validation processes. These criteria may generally be used for all output results, or for their average and maximum values. The Nash-Sutcliffe efficiency coefficient (E_{NS}), coefficient of determination (R^2), mass balance error (MBE) and peak flow rate error (PE) were used to evaluate the statistical indicators (SI) of the model outputs (Eq. 5 – 8). The E_{NS} ranges between -∞ and 1 while values between 0 and 1 are generally viewed as acceptable levels of performance. If the E_{NS} value is less than 0.50, 0.65 and 0.75, the model performance is evaluated as unsatisfactory, satisfactory and good, respectively. However, if the E_{NS} value is greater than 0.75, the model performance is said to be very good [16]. The model results are stated as acceptable by Joo et al. [17] if -30%≤PE≤+30% while by Moriasi et al. [16] if -30%≤MBE≤ +30%.

$$E_{NS} = 1.0 - \frac{\sum(Q_s - Q_o)^2}{\sum(Q_o - Q_{o,av})^2} \quad (5)$$

$$R^2 = \frac{\left[\sum(Q_s - Q_{s,av})(Q_o - Q_{obs,av})\right]^2}{\left[\sum(Q_s - Q_{s,av})\right]^2\left[\sum(Q_o - Q_{obs,av})\right]^2} \quad (6)$$

$$MBE = \frac{Q_{s,av} - Q_{o,av}}{Q_{o,av}} \quad (7)$$

$$PE = \frac{Q_{sp} - Q_{op}}{Q_{op}} \quad (8)$$

where $Q_{s,av}$, Q_{sp} and Q_{op} represent the average of simulated, peak of the simulated and peak of the observed discharge values, respectively.

In this study, the hydrologic parameters of the flood event occurred during 16 October – 06 November 2013 were calibrated using semi-distributed hydrologic model, HEC-HMS. Calibrated hydrologic parameters were validated using daily precipitation-runoff data for another flood event occurred in 17 June – 02 July 2002 (Table 1).

Table 1. Flood event characteristics for both calibration and validation processes

Flood duration	Q_p (m^3/s)	*Flood volume* (10^3 m^3)
17.06-02.07.2002	68.40	15903.65
16.10-06.11.2013	152.00	24947.14

5. Hydrologic Model Results

The initial and the calibrated values of the hydrologic parameters are presented in Table 2.

Table 2. Initial and calibrated values of hydrologic parameters

Hydrologic parameters	*Initial values*	*Calibrated values*
T_c *(hr)*	4.10	4.41
S_c *(hr)*	4.10	3.13
k (1/hr)	0.80	1.00
Q_{ts} (m^3/s)	1.16	3.63

The calibration of hydrologic parameters was performed for the period of 16 October – 06 November 2013, while the validation of hydrologic parameters was performed for 17 June – 02 July 2002. The calibrated and validated hydrographs are presented in Fig. 2. and the SI for both the calibration and the validation are presented in Table 3.

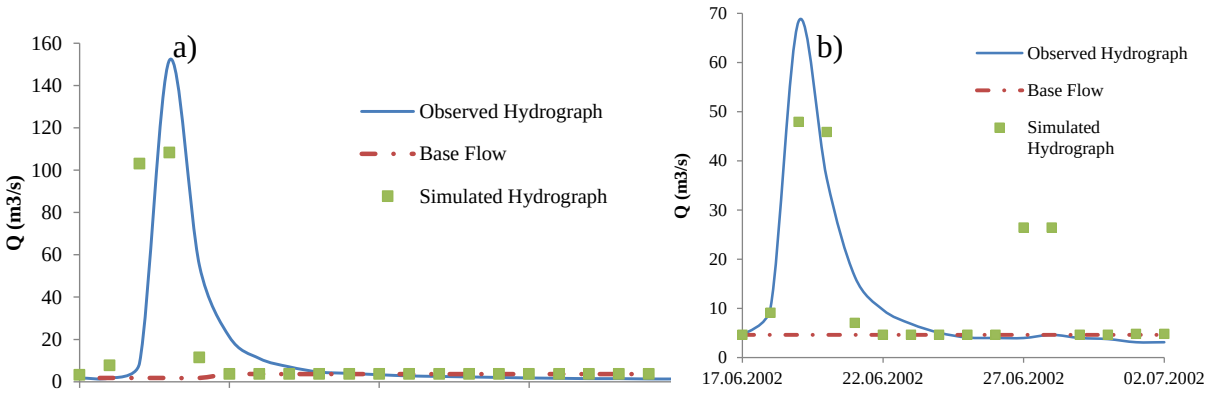

Fig. 2. Calibrated and validated flood hydrographs

Table 3. SI for both calibration and validation

Flood duration	E_{NS}	R^2	*MBE (%)*	*PE (%)*
16.10-06.11.2013	0.76	0.63	1.3	-28.7
17.06-02.07.2002	0.64	0.65	11.3	-29.9

It can be seen from the model outputs that calibrated hydrograph gave better results than validated hydrograph. While E_{NS} value for calibration can be accepted as very good, it can be evaluated as satisfactory for the validated hydrograph [16]. In both cases, the hydrograph is over estimated while the peak discharge is under estimated. Furthermore, the hydrograph estimation for calibration is closer to zero than for that of validation. All calibrated and validated hydrograph estimations are found to be in acceptable range. However, it should be noted that the model failed to reproduce the second peak discharge in the validated hydrograph. This anomaly can be explained by an error in the discharge data where the discharge reading might have been performed before the rain started. If the data discharge had been read after the precipitation, the model results would have been improved. As a result, *MBE* value would have been decreased and the E_{NS} and R^2 values would have been improved better.

6. Conclusions

In this study, the hydrologic parameters of Kocanaz watershed, a small basin in Western Black Sea Region, were estimated using a semi-distributed hydrologic model, HEC-HMS. The watershed was modelled as a single basin without dividing into sub basins. The hydrologic parameters of the model was calibrated by data of a flood event occurred in 2013 and then those calibrated parameters were validated by another flood event occurred in 2002. It is found out from model outputs that all calibrated and validated hydrograph estimations were in acceptable range.

Previous studies have shown that results obtained by modeling the whole basin as a single unit without dividing into sub basins gave improved results than using sub basins when they were evaluated according to the SI [3]. Increasing the number of sub basins would have a limited effect on peak flow, thereby resulting in some improvement in *PE* value. On the other hand, the disadvantage of increasing the number of sub basins is to calibrate more hydrologic parameters. Thus, determination of a large number of parameters would increase the uncertainty of the parameters determined by the model.

In this study, base flow values were determined by using the recession method. During calibration, the base flow values were kept constant while for validation process, they had two constant values forming one step. It is thought that the base flow increases with the change in flow in the rising limb of the hydrograph and possible errors arising from this increase are also affected in the results.

Acknowledgments

We gratefully acknowledge the Scientific and Technological Research Council of Turkey (TÜBİTAK) for their financial support (Project No. 114M292).

Notations

c	Proportionality constant
CN	Curve number
DSI	State Water Works
E_{NS}	Nash-Sutcliffe efficiency coefficient
HEC-HMS	Hydrologic Engineering Center-Hydrologic Modelling System
hr	Hour
IMD	Indian Meteorological Department
k	Recession constant
L	Main channel length

LBRM	Large Basin Runoff Model
MBE	Mass balance error
MUSIC	Model for Urban Stormwater Improvement Conceptualization
PE	Peak flow rate error
PWRMSE	Peak-weighted root mean square error
Q_0	Initial discharge
Q_b	Base flow
Q_{obs}	Observed discharge
$Q_{obs,av}$	Average od observed discharge
Q_{op}	Peak of observed discharge
$Q_{s,av}$	Average of simulated discharge
Q_{sim}	Simulated discharge
Q_{sp}	Peak of simulated discharge
Q_{ts}	Threshold discharge
R^2	Coefficient of determination
S	Basin average slope
S_c	Storage coefficient
SI	Statistical indicators
SCS	Soil Conservation Service
SWAT	Soil Water Assessment Toll
SWMM	Storm Water Management Model
T_c	Time of concentration
USA	United States of America

References

[1] Akay, H., Baduna Kocyigit, M., Yanmaz, A.M., Estimation of rainfall-runoff relation using HEC-HMS for a basin in Turkey, *Sustainable Hydraulics in the Era of Global Changes-Proceedings of the 4th European Congress of the IAHR*, Liege, Belgium, 2016.

[2] Zhang, H.L., Wang, Y.J., Wang, Y.Q., Li, D.X., Wang X.K., The effect of watershed scale on HEC-HMS calibrated parameters: a case study in the Clear Creek watershed in Iowa, US. *Hydrology and Earth System Sciences*, 17, 2735-2745, 2013.

[3] Baduna Kocyigit, M., Akay, H., Yanmaz, A.M., Effect of watershed partitioning on hydrologic parameters and estimation of hydrograph of an ungauged basin: a case study in Gokirmak and Kocanaz, Turkey. *Arabian Journal of Geosciences*, 10, 1-13, 2017.

[4] Akay, H., Baduna Kocyigit, M., Yanmaz, A.M., A Case Study for Determination of Hydrological Parameters in HEC-HMS in Computing Direct Runoff, *12th International Congress on Advances in Civil Engineering*, Istanbul, Turkey, 2016.

[5] Reshma, T., Reddy, K.V., Pratap, D., Ahmedi, M., Agilan V., Optimization of Calibration Parameters for an Event Based Watershed Model Using Genetic Algorithm. *Water Resources Management*, 29, 4589-4606, 2015.

[6] Chu, X., Steinman, A., Event and Continuous Hydrologic Modeling with HEC-HMS. *Journal of Irrigation and Drainage Engineering*, 135, 119-124, 2009.

[7] Laouacheria, F., Mansouri, R., Comparison of WBNM and HEC-HMS for Runoff Hydrograph Prediction in a SmallUrban Catchment. *Water Resources Management*, 29, 2485-2501, 2015.

[8] Kaffas, K., Hrissanthou, V., Application of a Continuous Rainfall-Runoff Model to the Basin of Kosynthos River using the Hydrologic Software HEC-HMS. *Global Nest*, 16, 188-203, 2014.

[9] Shahid, M.A., Boccardo, P., Usman, M., Albanese, A., Qamar, M.U., Predicting Peak Flows in Real Time through Event Based Hydrologic Modeling for a Trans-Boundary River Catchment. *Water Resources Management*, 31, 793-810, 2017.

[10] Yilmaz, A.G., Imteaz, M.A. & Ogwuda, O., Accuracy of HEC-HMS and LBRM Models in Simulating Snow Runoff in Upper Euphrates Basin. *Journal of Hydrologic Engineering*, 17, 342-347, 2012.

[11] Baloch, M.A., Ames, D.P., Tanik, A., Hydrologic impacts of climate and land use change on Namnam Stream in Koycegiz Watershed, Turkey. *International Journal of Environment Science and Technology*, 12, 1481-1494, 2015.

[12] Akiner, M.E., Akkoyunlu, A., Modeling and forecasting river flow rate from the Melen Watershed, Turkey. *Journal of Hydrology*, 456-457, 121-129, 2012.

[13] Yanmaz, M., *Applied Water Resources Engineering*, METU Press; 3rd edition, 2006.

[14] Ao, T.Q., Yoshitani, J., Takeuchi, K., Fukami, K., Mutsuura, T., Ishidaira, H., Effects of sub-basin scale on runoff simulation in distributed hydrological model: BTOPMC, *Weather Radar Information and Distributed Hydrological Modeling*, Sapparo, Japan, 2003.

[15] Rouhani, H., Willems, P., Feyen, J., Effect of watershed delineation and areal mean rainfall distribution on runoff prediction using the SWAT model. *Hydrology Research*, 40, 505-519, 2009.

[16] Moriasi, D.N., Arnold, J.G, Van Liew, M.W., Bingner, R.L., Harmel, R.D., Veith, T.L., Model evaluation guidelines for systematic quantification of accuracy in watershed simulations. *Transactions of the American Society of Agricultural and Biological Engineers*, 50, 885-900, 2007.

[17] Joo, J., Kjeldsen, T., Kim, H.J., Lee, H., A Comparison of Two Event-based Flood models (ReFH-rainfall Runoff Model and HEC-HMS). *KSCE Journal of Civil Engineering*, 18, 330-343, 2014.

International Journal of Engineering & Applied Sciences (IJEAS)
Vol.9, Issue 4 (2017) 51-64
http://dx.doi.org/10.24107/ijeas.349872
Int J Eng Appl Sci 9(4) (2017) 51-64

Fifth Order Predictor-Corrector Method for Quadratic Riccati Differential Equations

Gemadi Roba [a], Gashu Gadisa [b,], Kefyalew Hailu [c]*

[a,b,c] Department of Mathematics, Jimma University, P. O. Box 378, Jimma, Ethiopia
**Email: ggadisa@yahoo.com*

ORCID numbers of authors:
0000-0002-6366-5953[a], 0000-0003-3541-2630[b], 0000-0002-6206-4523[c]

Received date: November 2017
Accepted date: December 2017

Abstract

In this paper, fifth order predictor-corrector method is presented for solving quadratic Riccati differential equations. First, the interval is discretized and then the method is formulated by using the Newton's backward difference interpolation formula. The stability and convergence of the method have been investigated. To validate the applicability of the proposed method, three model examples with exact solutions have been considered and numerically solved by using MATLAB software. The numerical results are presented in tables and figures for different values of mesh size h. Pointwise absolute errors and maximum absolute errors are also estimated. Concisely, the present method gives better result than some existing numerical methods reported in the literature.

Keywords: Predictor-corrector method, Riccati differential equations, Stability analysis

1. Introduction

Problems arising in many physical phenomena, engineering and scientific applications are modeled with nonlinear differential equations. Riccati differential equation is applicable in engineering science applications such as stochastic realization theory, optimal control, robust stabilization, network synthesis, diffusion problems, and the newer applications include such areas as financial mathematics, Allahviranlooa and Behzadib [1]. The solution of Riccati differential equations has so much importance in numerical methods due to the fact that even higher order partial differential equations can be transformed into first order ordinary differential equation and solved, Baba [2]. Thus, methods of solution of such differential equations have attracted attention of researchers for a very long time.

Recently, some researchers have been tried to find the approximate solution of first order nonlinear ordinary differential equations. For example; Gashu and Habtamu [3] considered the comparison of higher order Taylor's method and fifth order Runge-Kutta method; Gemechis and Tesfaye [4] presented fourth order Runge-Kutta for solving quadratic Riccati differential equations; Vinod and Dimple [5] presented Newton-Raphson based modified Laplace Adomian decomposition method for solving quadratic Riccati differential equations;

Fateme and Esmaile [6] presented approximate solution for quadratic Riccati differential equations. Other authors [7-13] also discussed the quadratic Riccati differential equations. However, some of these methods are not more accurate. Thus in this paper, we present a stable and more accurate numerical method for solving quadratic Riccati differential equations.

2. Description of the Methods

Consider the quadratic Riccati differential equation of the form:

$$\frac{dy}{dx} = p(x) + q(x)\,y(x) + r(x)y^2(x) \tag{1}$$

with initial condition,

$$y(x_0) = \alpha \tag{2}$$

where, $p(x), q(x), r(x)$ are continuous functions, $r(x) \neq 0$ and α is arbitrary constant.
To describe the methods, denote Eq. (1) as:

$$\frac{dy}{dx} = f(x, y) \tag{3}$$

Now, divide the interval $[x_0, L]$ into N equal subintervals of mesh length h and the mesh points given by $x_i = x_0 + ih$, $i = 1, 2, \ldots, N$. Then, $h = \frac{L - x_0}{N}$, where N is a positive integer.
Integrating Eq. (3) on the interval $[x_i, x_{i+1}]$, we obtain:

$$\int_{x_i}^{x_{i+1}} \frac{dy}{dx}\,dx = \int_{x_i}^{x_{i+1}} f(x, y)\,dx$$

$$\Rightarrow y(x_{i+1}) = y(x_i) + \int_{x_i}^{x_{i+1}} f(x, y)\,dx \tag{4}$$

To derive the methods, we approximate $f(x, y)$ by a suitable interpolation polynomials.

2.1. Description of Predictor Method

Let us take k data values (x_i, f_i), $(x_{i-1}, f_{i-1}),\ldots,(x_{i-k+1}, f_{i-k+1})$. For this data, we fit the Newton's backward difference interpolating polynomial of degree $k-1$ and we get:

$$p_{k-1}(x) = f(x_i + sh) = f(x_i) + s\nabla f(x_i) + \frac{s(s+1)}{2!}\nabla^2 f(x_i) + \ldots + \frac{s(s+1)(s+2)\ldots(s+k-2)}{(k-1)!}\nabla^{k-1} f(x_i) + T_k^p \tag{5}$$

where

$$s = \frac{x - x_i}{h} \text{ and } T_k^p = \frac{s(s+1)(s+2)\ldots(s+k-1)}{k!} h^k f^{(k)}(\xi) \tag{6}$$

is the error term, when ξ lies in some interval containing the points x_i, $x_{i-1,\ldots,}x_{i-k+1}$ and x. The limits of integration in Eq. (4) becomes:

$$x = x_i \Rightarrow s = 0,\ x = x_{i+1} \Rightarrow s = 1 \text{ and } dx = hds. \tag{7}$$

Thus, replacing $f(x, y)$ by $P_{k-1}(x)$ in Eq. (4) and using Eq. (5) in Eq. (4), we get:

$$y_{i+1} = y_i + h\int_0^1 \left\{ f_i + s\nabla f_i + \frac{1}{2}s(s+1)\nabla^2 f_i + \frac{1}{6}s(s+1)(s+2)\nabla^3 f_i + \ldots \right\} ds \tag{8}$$

Now, on integrating term by term in Eq. (8) with respect to s, we obtain:

$$\int_0^1 s\,ds = \frac{1}{2}, \qquad \int_0^1 s(s+1)\,ds = \frac{5}{6}, \qquad \int_0^1 s(s+1)(s+2)\,ds = \frac{9}{4},$$

$$\int_0^1 s(s+1)(s+2)(s+3)\,ds = \frac{251}{30}, \qquad \int_0^1 s(s+1)(s+2)(s+3)(s+4)\,ds = \frac{475}{12}$$

Hence, from Eq. (8), we get:

$$y_{i+1} = y_i + h\left\{ f_i + \frac{1}{2}\nabla f_i + \frac{5}{12}\nabla^2 f_i + \frac{3}{8}\nabla^3 f_i + \frac{251}{720}\nabla^4 f_i + \frac{475}{1440}\nabla^5 f_i + \ldots \right\} \tag{9}$$

We obtain the error term as:

$$T_k^p = h^{k+1}\int_0^1 \frac{s(s+1)\ldots(s+k-1)}{(k)!} f^{(k)}(\xi_k)ds = h^{k+1}\int_0^1 g_p(s)\, f^{(k)}(\xi_k)ds, \quad 0<\xi_k<1 \qquad (10)$$

where

$$g_p(s) = \frac{1}{k!}\big(s(s+1)(s+2)\ldots(s+k-1)\big) \qquad (11)$$

By choosing different values for *k*, we get different methods. But for this particular study, we choose the value for $k=5$ which is of order five method. Thus, we get:

$$\begin{aligned} y_{i+1} &= y_i + h\left[f_i + \frac{1}{2}\nabla f_i + \frac{5}{12}\nabla^2 f_i + \frac{3}{8}\nabla^3 f_i + \frac{251}{720}\nabla^4 f_i\right] + T_5 \\ &= y_i + h\Big\{f_i + \frac{1}{2}(f_i - f_{i-1}) + \frac{5}{12}(f_i - 2f_{i-1} + f_{i-2}) + \frac{3}{8}(f_i - 3f_{i-1} + 3f_{i-2} - f_{i-3}) \\ &\quad + \frac{251}{720}(f_i - 4f_{i-1} + 6f_{i-2} - 4f_{i-3} + f_{i-4})\Big\} + T_5 \\ &= y_i + \frac{h}{720}\{1901f_i - 2774f_{i-1} + 2616f_{i-2} - 1274f_{i-3} + 251f_{i-4}\} + T_5 \end{aligned} \qquad (12)$$

where

$$T_5 = \frac{475}{1440}h^6 f^{(5)}(\xi_5) = \frac{475}{1440}h^6 y^{(6)}(\xi_5) \qquad (13)$$

is the local truncation error. Hence, Eq. (12) is called fifth order predictor method.

2.2. Description of Corrector Method

Consider the $k+1$ data values, $(x_{i+1}, f_{i+1}),(x_i, f_i),(x_{i-1}, f_{i-1}),\ldots,(x_{i-k+1}, f_{i-k+1})$ which include the current data point. For this data, we fit the Newton's backward difference interpolating polynomial of degree *k* and we get:

$$\begin{aligned} p_k(x) = f(x_i + sh) = f(x_{i+1}) + (s-1)\nabla f(x_{i+1}) + \frac{(s-1)s}{2!}\nabla^2 f(x_{i+1}) + \ldots \\ + \frac{(s-1)s(s+1)(s+2)\ldots(s+k-2)}{(k)!}\nabla^k f(x_{i+1}) + T_k^c \end{aligned} \qquad (14)$$

where

$$s = \frac{x - x_i}{h}\ ,\ x - x_{i+1} = (x - x_i) - (x_{i+1} - x_i) = sh - h = h(s-1),$$

$$T_k^c = \frac{(s-1)s(s+1)(s+2)\ldots(s+k-1)}{(k+1)!}h^{k+1}f^{(k+1)}(\xi) \qquad (15)$$

is the error term, when ξ lies in some interval containing the points x_{i+1}, x_i, x_{i-1},…, x_{i-k+1} and x.

The limit of integration in Eq. (4) becomes:

$$x = x_i \Rightarrow s = 0\,,\ x = x_{i+1} \Rightarrow s = 1 \text{ and } dx = hds\,. \tag{16}$$

Thus, replacing $f(x, y)$ by $p_k(x)$ in Eq. (4) and using Eq. (14) in Eq. (4), we get:

$$y_{i+1} = y_i + h\int_0^1 \left\{ f_{i+1} + (s-1)\nabla f_{i+1} + \frac{(s-1)s}{2}\nabla^2 f_{i+1} + \frac{(s-1)s(s+1)}{6}\nabla^3 f_{i+1} + \ldots \right\} ds \tag{17}$$

Here,

$$\int_0^1 (s-1)\,ds = \frac{-1}{2}, \qquad \int_0^1 (s-1)s\,ds = \frac{-1}{6}, \qquad \int_0^1 (s-1)s(s+1)\,ds = \frac{-1}{4},$$
$$\int_0^1 (s-1)s(s+1)(s+2)\,ds = \frac{-19}{30}, \quad \int_0^1 (s-1)s(s+1)(s+2)(s+3)\,ds = \frac{-9}{4} \tag{18}$$

Hence, from Eq. (17), we get:

$$y_{i+1} = y_1 + h\left\{ f_{i+1} - \frac{1}{2}\nabla f_{i+1} - \frac{1}{12}\nabla^2 f_{i+1} - \frac{1}{24}\nabla^3 f_{i+1} - \frac{19}{720}\nabla^4 f_{i+1} - \frac{9}{480}\nabla^5 f_{i+1} - \ldots \right\} \tag{19}$$

Using Eq. (15), we obtain the error term as:

$$T_k^c = h^{k+2}\int_0^1 \frac{(s-1)s(s+1)(s+2)\ldots(s+k-1)}{(k+1)!}\, f^{(k+1)}(\xi_k)$$
$$= h^{k+2}\int_0^1 g_c(s)\, f^{(k+1)}(\xi_k)ds, \qquad 0 < \xi_k < 1 \tag{20}$$

where

$$g_c(s) = \frac{1}{(k+1)!}\{(s-1)s(s+1)\ldots(s+k-1)\} \tag{21}$$

By choosing different values for *k*, different corrector methods will be obtained. So, as we have discussed before we choose k for fifth order, which implies $k = 4$.

i.e, by choosing $k=4$, we get the method:

$$\begin{aligned} y_{i+1} &= y_i + h\left\{ f_{i+1} - \frac{1}{2}\nabla f_{i+1} - \frac{1}{12}\nabla^2 f_{i+1} - \frac{1}{24}\nabla^3 f_{i+1} - \frac{19}{720}\nabla^4 f_{i+1} \right\} + T_4 \\ &= y_i + h\left\{ f_{i+1} - \frac{1}{2}(f_{i+1} - f_i) - \frac{1}{12}(f_{i+1} - 2f_i + f_{i-1}) - \frac{1}{24}(f_{i+1} - 3f_i + 3f_{i-1} - f_{i-2}) \right. \\ &\quad \left. - \frac{19}{720}(f_{i+1} - 4f_i + 6f_{i-1} - 4f_{i-2} + f_{i-3}) \right\} + T_4 \\ &= y_i + \frac{h}{720}\{251 f_{i+1} + 646 f_i - 264 f_{i-1} + 106 f_{i-2} - 19 f_{i-3}\} + T_4 \end{aligned} \tag{22}$$

where

$$T_4 = \frac{-9}{480} h^6 f^{(5)}(\xi_4) = \frac{-9}{480} h^6 y^{(6)}(\xi_4) \tag{23}$$

is the local truncation error. Hence Eq. (22) is called fifth order corrector method. So that, we use Eqs. (12) and (22) for solving quadratic Riccati differential equation in Eq. (1) with Eq. (2).

Remarks:

1. For using the methods, we require the starting values $y_0,\ y_1,\ y_2,\ y_3$.
2. The required starting values for the application of predictor-corrector methods are obtained by using any single step method like Euler's method, Taylor series method or Runge-Kutta methods.

3. Stability and Convergence Analysis

Definition 1: Let $\lambda_1, \lambda_2, \ldots, \lambda_k$ are the (not necessarily distinct) roots of the characteristic equation given by:

$$p(\lambda) = \lambda^k - a_{k-1}\lambda^{k-1} - \cdots - a_1\lambda - a_0 = 0 \tag{24}$$

associated with the multistep difference method of Eqs. (12) and (22) given as:

$$\begin{aligned} &y_{i+1} = a_{k-1}y_i + a_{k-2}y_{i-1} + \ldots + a_0 y_{i+1-k} + hF(x_i, h,\ y_{i+1},\ y_i,\ \ldots,\ y_{i+1-k}), \\ &\quad y_0 = \alpha,\ \ y_1 = \alpha_1,\ \ \ldots,\ \ y_{k-1} = \alpha_{k-1}, \text{ for each } i = k-1,\ k, \ldots, N-1, \end{aligned} \tag{25}$$

where $a_0, a_1, \ldots, a_{k+1}$ are constants.

If $|\lambda_i| \leq 1$, for $i = 1, 2, \ldots, k$, and all roots with absolute value 1 are simple roots, then the difference method is said to satisfy the root condition.

Definition 2 (Stability) [14]:

i. Methods that satisfy the roots condition in which λ = 1 is the only root of the characteristic equation with magnitude one are called strongly stable.
ii. Methods that satisfy the root condition and have more than one distinct root with magnitude one are called weakly stable.
iii. Methods that do not satisfy the root condition are called unstable.

Theorem 1: The fifth order predictor method in Eq. (12) is strongly stable.

Proof: The fifth order predictor method in Eq. (12) can be expressed as:

$$y_{i+1} = y_i + hF\left(x_i, h, y_{i+1}, y_i, \ldots, y_{i-3}, y_{i-4}\right) \tag{26}$$

where

$$F\left(x_i, h, y_{i+1}, y_i, \ldots, y_{i-3}, y_{i-4}\right) = \frac{1}{720}\left\{1901 f\left(x_i, y_i\right) - 2774 f\left(x_{i-1}, y_{i-1}\right) + 2616 f\left(x_{i-2}, y_{i-2}\right) - 1274 f\left(x_{i-3}, y_{i-3}\right) + 251 f\left(x_{i-4}, y_{i-4}\right)\right\} \tag{27}$$

In this case, we have: $k = 5,\ a_0 = a_1 = a_2 = a_3 = 0,$ and $a_4 = 1$.

The characteristic equation for the method becomes:

$$p(\lambda) = \lambda^5 - \lambda^4 = \lambda^4(\lambda - 1) = 0$$
$$\Rightarrow \lambda_1 = 1,\ \lambda_2 = \lambda_3 = \lambda_4 = \lambda_5 = 0 \tag{28}$$

are the roots of the polynomial.

Therefore, it satisfies the root condition and is strongly stable by Definition 2 (i).

Theorem 2: The fifth order corrector method in Eq. (22) is also strongly stable.

Proof: The fifth order corrector method in Eq. (22) can be expressed as:

$$y_{i+1} = y_i + hF\left(x_i, h, y_{i+1}, y_i, \ldots, y_{i-3}\right) \tag{29}$$

where

$$F\left(x_i.h, y_{i+1}\ , y_i, \ldots, y_{i-3}\right) = \frac{1}{720}\left\{251 f\left(x_{i+1}, y_{i+1}\right) + 646 f\left(x_i, y_i\right) - 264 f\left(x_{i-1}, y_{i-1}\right) + 106 f\left(x_{i-2}, y_{i-2}\right) - 19 f\left(x_{i-3}, y_{i-3}\right)\right\} \tag{30}$$

Following the similar procedure as we have done in Theorem 1, here,

$$k = 4,\ \ a_0 = a_1 = a_2 = 0,\ \ a_3 = 1 \tag{31}$$

The characteristic equation for the method becomes:

$$p(\lambda) = \lambda^4 - \lambda^3 = \lambda^3(\lambda - 1) = 0 \tag{32}$$

Thus, this polynomial has roots

$$\lambda_1 = 1,\ \ \lambda_2 = 0 = \lambda_3 = \lambda_4. \tag{33}$$

Therefore, it satisfies the root condition and is strongly stable by Definition 2 (i).

Definition 3 (Consistency): The method is consistent, if the local truncation error $T_k(h) \to 0$ as $h \to 0$.

From Eqs. (13) and (23), we have:

$$T_4 = \frac{-9}{480} h^6 y^{(6)}(\xi_4) \quad \text{and} \quad T_5 = \frac{475}{1440} h^6 y^{(6)}(\xi_5) \tag{34}$$

Thus, $T_k(h) \to 0$ as $h \to 0$ for $k = 4, 5$.

Therefore, the methods in Eq. (12) and (22) are consistent by Definition 3. Hence, they are convergent of fifth order. Since, consistency + stability $\Leftrightarrow$ convergence.

4. Numerical Examples and Results

To validate the applicability of the methods, three model examples of quadratic Riccati differential equations with initial conditions have been considered. Since all predictor-corrector methods are not a self-starter, we take the classical Runge-Kutta (RK4) method for the first four nodal points. For each number of nodal points N, the pointwise absolute errors are approximated by the formula, $\|E\| = |y(x_i) - y_i|$, for $i = 0, 1, 2, \cdots, N$, where $y(x_i)$ and y_i

are the exact and computed approximate solution of the given problems respectively, at the nodal point x_i. Numerical examples are given to illustrate the efficiency and convergence of the methods.

Example 1. Consider the following quadratic Riccati differential equation, Vinod and Dimple [5]; Khalid et al. [12],

$$\begin{aligned} y'(x) &= 1 + y^2(x), \quad 0 \le x \le 1, \\ y(0) &= 0 \end{aligned} \tag{35}$$

where the exact solution of this equation is $y(x) = \tan x$.

Table 1. Pointwise absolute errors for Example 1 with different values of *N*.

x	Vinod and Dimple [5]	Present Method N = 100	N = 100 Refinement	N = 200	N = 300	N = 400	N = 500
0.01	2.5001250e-07	8.3330e-13	8.3330e-13	5.2076e-14	1.0285e-14	3.2543e-15	1.0651e-15
0.02	2.0004001e-06	1.6657e-12	1.6657e-12	1.0409e-13	1.3538e-14	3.1954e-15	1.0443e-15
0.03	6.7530387e-06	2.4961e-12	2.4961e-12	1.0114e-13	1.3108e-14	3.0809e-15	1.0131e-15
0.04	1.6012809e-05	3.3232e-12	2.3825e-12	9.6610e-14	1.2476e-14	2.9421e-15	9.7145e-16
0.05	3.1289104e-05	3.1598e-12	3.1590e-12	9.0469e-14	1.1616e-14	2.7339e-15	9.0206e-16
0.06	5.4097349e-05	2.9452e-12	2.9438e-12	8.2712e-14	1.0547e-14	2.4772e-15	8.2573e-16
0.07	8.5960526e-05	2.6789e-12	2.6768e-12	7.3316e-14	9.2426e-15	2.1788e-15	7.3552e-16
0.08	1.2841072e-04	2.3600e-12	2.3571e-12	6.2270e-14	7.7161e-15	1.8319e-15	6.2450e-16
0.09	1.8299066e-04	1.9876e-12	1.9836e-12	4.9488e-14	5.9674e-15	1.4155e-15	4.8572e-16
0.1	2.5125533e-04	1.5604e-12	1.5553e-12	3.4958e-14	3.9829e-15	9.4369e-16	3.3307e-16

Table 2. The maximum absolute errors for Example 1 with different values of *N*.

N = 50	N = 100	N = 200	N = 300	N = 400	N = 500
1.6183e-07	6.6504e-09	2.3871e-10	3.2945e-11	8.0336e-12	2.6552e-12
Refinement					
1.7156e-07	6.7519e-09	2.3963e-10	3.3001e-11	8.0413e-12	2.6570e-12

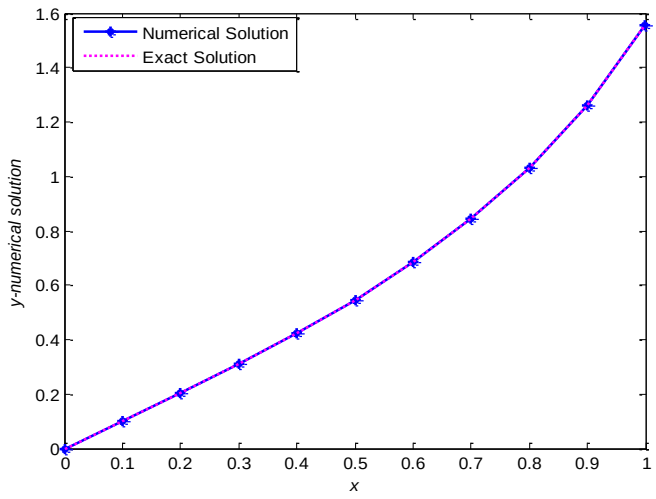

Fig. 1. Numerical solution versus exact solution for Example 1 when N = 10.

Example 2. Consider the following quadratic Riccati differential equation, Gemechis and Tesfaye [4]; Fateme and Esmaile [6],

$$\begin{aligned} &y'(x) = e^{x} - e^{3x} + 2e^{2x}y(x) - e^{x}y^{2}(x), \quad 0 \le x \le 1, \\ &y(0) = 1 \end{aligned} \tag{36}$$

The exact solution of the given problem is given by $y(x) = e^{x}$.

Table 3. Pointwise absolute errors for Example 2 with different values of N.

x	N = 10	N = 40	N = 70	N = 100	N = 200	N = 400
Present Method						
0.1	1.1153e-07	4.5427e-10	2.5490e-11	4.1438e-12	1.2457e-13	4.6629e-15
0.2	2.6297e-07	4.3364e-10	2.4216e-11	3.9286e-12	1.1813e-13	4.8850e-15
0.3	4.6838e-07	4.1083e-10	2.2808e-11	3.6910e-12	1.1036e-13	4.8850e-15
0.4	7.4674e-07	3.8563e-10	2.1253e-11	3.4284e-12	1.0236e-13	4.8850e-15
0.5	7.2073e-07	3.5778e-10	1.9533e-11	3.1379e-12	9.3259e-14	4.6629e-15
0.6	6.9197e-07	3.2699e-10	1.7632e-11	2.8164e-12	8.3489e-14	1.1102e-15
0.7	6.6020e-07	2.9297e-10	1.5530e-11	2.4616e-12	7.2387e-14	3.5527e-15
0.8	6.2508e-07	2.5537e-10	1.3208e-11	2.0699e-12	6.0396e-14	7.1054e-15
0.9	5.8627e-07	2.1382e-10	1.0642e-11	1.6369e-12	4.6185e-14	1.3323e-14
1.0	5.4337e-07	1.6790e-10	7.8062e-12	1.1582e-12	3.1530e-14	1.9096e-14
Gemechis and Tesfaye [4]						
0.1	3.8296e-07	4.5427e-10	4.8711e-11	1.1722e-11	7.3475e-13	4.5963e-14
0.2	2.6297e-07	1.0710e-09	1.1484e-10	2.7633e-11	1.7317e-12	1.0880e-13
0.3	4.6838e-07	1.9073e-09	2.0451e-10	4.9211e-11	3.0835e-12	1.9384e-13
0.4	7.4674e-07	3.0404e-09	3.2600e-10	7.8447e-11	4.9163e-12	3.0909e-13
0.5	1.1237e-06	4.5748e-09	4.9051e-10	1.1803e-10	7.3965e-12	4.6496e-13
0.6	1.6338e-06	6.6511e-09	7.1312e-10	1.7160e-10	1.0753e-11	6.7191e-13
0.7	2.3239e-06	9.4596e-09	1.0142e-09	2.4406e-10	1.5293e-11	9.5124e-13
0.8	3.2569e-06	1.3257e-08	1.4214e-09	3.4203e-10	2.1432e-11	1.3305e-12
0.9	4.5182e-06	1.8390e-08	1.9717e-09	4.7445e-10	2.9730e-11	1.8439e-12
1.0	6.2225e-06	2.5327e-08	2.7154e-09	6.5340e-10	4.0941e-11	2.5673e-12

Table 4. Pointwise absolute errors for Examples 2 with different values of N.

x	Fateme and Esmaile [6]	Present Method	
		N = 10	N = 300
0.0	0.0000000000000	0.0	0.0
0.1	0.00034681435605	1.1153e-07	1.6209e-14
0.3	0.00067436472882	4.6838e-07	1.4655e-14
0.5	3.8747×10^{-10}	7.2073e-07	1.3989e-14
0.7	0.00067437189321	6.6020e-07	7.1054e-15
0.9	0.00034682221170	5.8627e-07	2.2204e-15
1.0	0.000000000000	5.4337e-07	6.2172e-15

Table 5. The maximum absolute errors for Examples 2 with different values of N.

N = 50	N = 100	N = 200	N = 300	N = 400	N = 500
1.4455e-10	4.2630e-12	1.2945e-13	1.9096e-14	1.6875e-14	4.4409e-15
Refinement					
1.4327e-10	4.2437e-12	1.2923e-13	1.9096e-14	1.6875e-14	4.4409e-15

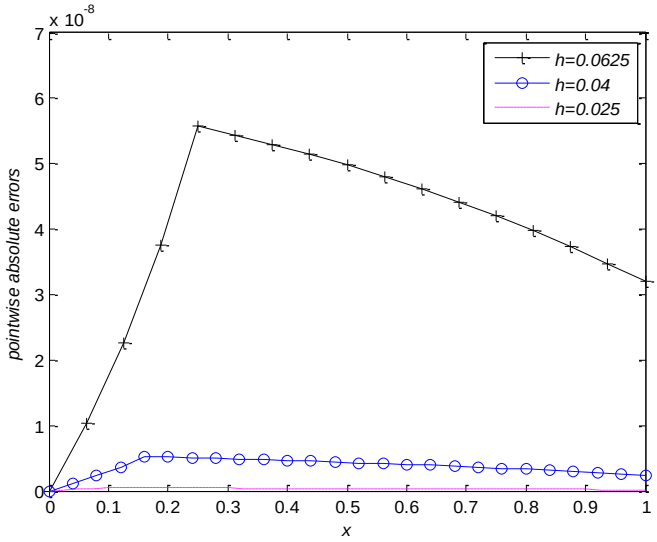

Fig. 2. Pointwise absolute errors of Example 2 for different values of h .

Example 3. Consider the following quadratic Riccati differential equation, Gemechis and Tesfaye [4]; Fateme and Esmaile [6],

$$\begin{aligned} &y'(x) = 1 + 2y(x) - y^2(x), \quad 0 \le x \le 1, \\ &y(0) = 0 \end{aligned} \tag{37}$$

where the exact solution of this equation is

$$y(x) = 1 + \sqrt{2}\tanh\left(\sqrt{2}x + 0.5\ln\left(\frac{\sqrt{2}-1}{\sqrt{2}+1}\right)\right) \tag{38}$$

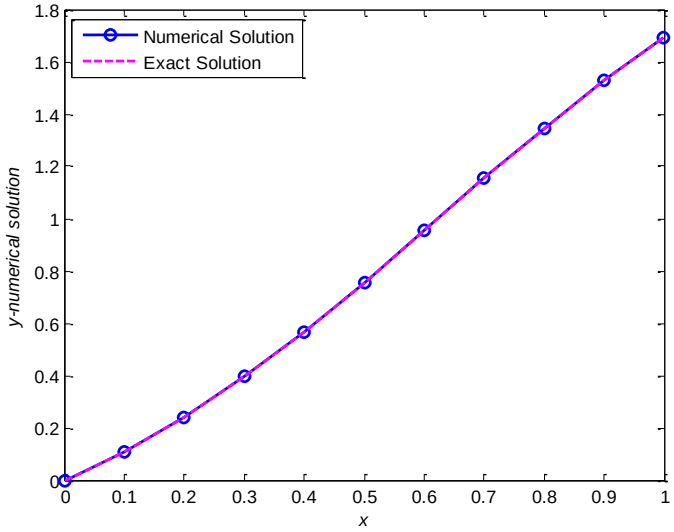

Fig. 3. Numerical solution versus exact solution of Example 3 when N = 10.

Table 6. Pointwise absolute errors for Example 3 with different values of N.

x	N = 10	N = 40	N = 70	N = 100	N = 200	N = 400
Present Method						
0.1	2.2551e-06	9.8491e-09	6.5613e-10	1.1501e-10	3.7895e-12	1.2192e-13
0.2	4.7763e-06	1.0576e-08	6.8253e-10	1.1788e-10	3.8127e-12	1.2154e-13
0.3	7.3083e-06	7.5309e-09	4.4688e-10	7.4441e-11	2.3045e-12	7.2109e-14
0.4	9.5635e-06	9.9895e-11	6.4516e-11	1.5673e-11	6.6713e-13	2.2982e-14
0.5	2.7825e-06	9.6406e-09	6.8248e-10	1.2102e-10	4.0088e-12	1.2823e-13
0.6	6.9705e-06	1.6943e-08	1.0936e-09	1.8762e-10	5.9928e-12	1.9307e-13
0.7	1.5393e-05	1.7084e-08	1.0377e-09	1.7402e-10	5.4168e-12	1.7675e-13
0.8	1.6632e-05	9.0960e-09	5.1689e-10	8.4664e-11	2.5677e-12	9.0150e-14
0.9	7.1404e-06	3.1027e-09	1.9362e-10	3.2240e-11	9.8810e-13	1.6209e-14
1.0	1.0444e-05	1.3554e-08	7.5227e-10	1.2112e-10	3.5889e-12	9.3703e-14
Gemechis and Tesfaye [4]						
0.1	2.2551e-06	9.8491e-09	1.0669e-09	2.8533e-10	1.6233e-11	1.0184e-12
0.2	4.7763e-06	2.0641e-08	2.2327e-09	5.3915e-10	3.3923e-11	2.1275e-12
0.3	7.3083e-06	3.1235e-08	3.3731e-09	8.1402e-10	5.1180e-11	3.2087e-12
0.4	9.5635e-06	4.0441e-08	4.3607e-09	1.0517e-09	6.6078e-11	4.1415e-12
0.5	1.1301e-05	4.7374e-08	5.1021e-09	1.2299e-09	7.7230e-11	4.8390e-12
0.6	1.2408e-05	5.1724e-08	5.5661e-09	1.3414e-09	8.4199e-11	5.2707e-12
0.7	1.2940e-05	5.3815e-08	5.7892e-09	1.3949e-09	8.7546e-11	5.4756e-12
0.8	1.3100e-05	5.4419e-08	5.8528e-09	1.4101e-09	8.8489e-11	5.5316e-12
0.9	1.3141e-05	5.4381e-08	5.8450e-09	1.4079e-09	8.8322e-11	5.5178e-12
1.0	1.3245e-05	5.4260e-08	5.8236e-09	1.4019e-09	8.7889e-11	5.5029e-12

Table 7. Pointwise absolute errors for Examples 3 with different values of N.

x	Fateme and Esmaile [6]	Present Method	
		N = 10	N = 300
0.0	9.6780×10^{-11}	0.0	0.0
0.1	0.000248944564121	2.2551e-06	5.0812e-13
0.3	0.0004481946615024	7.3083e-06	3.0248e-13
0.5	2.89441×10^{-10}	2.7825e-06	5.3524e-13
0.7	0.000374115023553	1.5393e-05	7.1365e-13
0.9	0.00017849475908	7.1404e-06	1.2368e-13
1.0	3.2516×10^{-10}	1.0444e-05	4.5808e-13

Table 8. The maximum absolute errors for Examples 3 with different values of N.

N = 50	N = 100	N = 200	N = 300	N = 400	N = 500
6.0022e-09	1.9281e-10	6.1084e-12	8.0802e-13	1.9695e-13	6.1950e-14
Refinement					
6.0007e-09	1.9281e-10	6.1084e-12	8.0802e-13	1.9695e-13	6.1950e-14

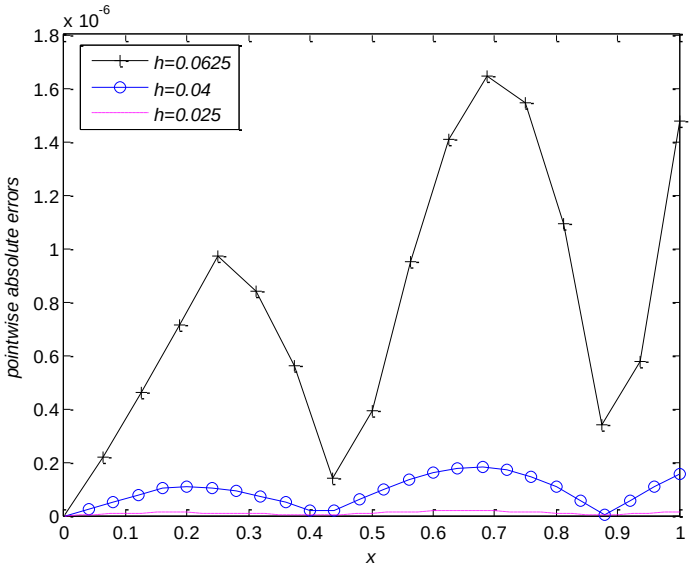

Fig. 4. Pointwise absolute errors of Example 3 for different values of *h*.

5. Discussion and Conclusion

In this paper, fifth order predictor-corrector method is presented for solving quadratic Riccati differential equations. The stability and convergence of the method have been investigated. The study is implemented on three model examples with exact solutions by taking different values for *N*, and the computational results are presented in the Tables (1–8). The results obtained by the present method are compared with the results of Gemechis and Tasfaye [4], Vinod and Dimple [5], Fateme and Esmaile [6] and shows betterment.

Furthermore, from the Tables (1–5) it is significant that all of the absolute errors decrease rapidly as *h* decreases, which in turn shows the convergence of the computed solution. Figs. (1, 3) shows that the present method approximates the exact solution very well. Figs. (2, 4) show that, as *h* decreases the absolute error goes to zero. This shows that the small step size provides the better approximation. Briefly, the present method is stable, more accurate and effective method for solving quadratic Riccati differential equations.

Acknowledgments

The authors would like to thank Jimma University for the financial and material support.

References

[1] Allahviranlooa, T. and Behzadib Sh. S., Application of iterative methods for solving general Riccati equation. *Int. J. Industrial Mathematics* (ISSN 2008-5621), 4 (4), 389-404, 2012.

[2] Baba Seidu, A Matrix system for computing the coefficients of the Adams Bashforth-Moulton Predictor-Corrector formulae. *International journal of computational and applied mathematics*, 6 (3), 215-220, 2011.

[3] Gashu Gadisa and Habtamu Garoma, Comparison of higher order Taylor's method and Runge-Kutta methods for solving first order ordinary differential equations. *Journal of Computer and Mathematical Sciences*, 8 (1), 12-23, 2017.

[4] Gemechis File and Tesfaye Aga, Numerical solution of quadratic Riccati differential equations. *Egyptian journal of basic and applied sciences* 3, 392–397, 2016.

[5] Vinod Mishra and Dimple Rani, Newton-Raphson based modified Laplace Adomian decomposition method for solving quadratic Riccati differential equations. *MATEC Web of Conferences*, 57 (05001), 2016.

[6] Fateme Ghomanjani and Esmaile Khorram, Approximate solution for quadratic Riccati differential equation. *Journal of Taibah University for Science* 11, 246–250, 2017.

[7] Opanuga Abiodun A., Edeki Sunday O., Okagbue Hilary I. and Akinlabi Grace O., A novel approach for solving quadratic Riccati differential equations. *International Journal of Applied Engineering Research*, 10 (11), 29121-29126, 2015.

[8] Biazar, J. and Eslami, M., Differential Transform method for quadratic Riccati differential equation. *International Journal of Nonlinear Science*, 9 (4), 444-447, 2010.

[9] Changqing Yang, Jianhua Hou and Beibo Qin, Numerical solution of Riccati differential equations by using hybrid functions and tau method. *International Scholarly and Scientific Research & Innovation*, 6 (8), 871-874, 2012.

[10] Geng, F., Lin, Y. and Cui, M., A piecewise variational iteration method for Riccati differential equations. *Comput. Math. Appl.*, 58, 2518-2522, 2009.

[11] Gulsu, M., and Sezer, M., On the solution of the Riccati equation by the Taylor matrix method. *Applied Mathematics and Computation*, 176, 414–421, 2006.

[12] Khalid, M., Mariam Sultana, Faheem Zaidi and Uroosa Arshad, An effective perturbation iteration algorithm for solving Riccati differential equations. *International Journal of Computer Applications*, 111 (10), 1-5, 2015.

[13] Tan, Y. and Abbasbandy, S., Homotopy analysis method for quadratic Riccati differential equation. *Commun. Nonlinear Sci. Numer. Simul.*, 13, 539-546, 2008.

[14] David Eberly, *Stability Analysis for Systems of Differential Equations*. Geometric Tools, LLC, 2008.

International Journal of Engineering & Applied Sciences (IJEAS)
Vol.9, Issue 4 (2017) 65-75
http://dx.doi.org/10.24107/ijeas.356197
Int J Eng Appl Sci 9(4) (2017) 65-75

Novel Weak Form Quadrature Element Method for Free Vibration Analysis of Hybrid Nonlocal Euler-Bernoulli Beams with General Boundary Conditions

Xinwei Wang

State Key Laboratory of Mechanics and Control of Mechanical Structures,
Nanjing University of Aeronautics and Astronautics,
Nanjing 210016, CHINA
**E-mail address*: wangx@nuaa.edu.cn

ORCID numbers of authors:
0000-0003-2825-3336

Received date: November 2017
Accepted date: December 2017

Abstract

A novel weak form quadrature element method (QEM) is presented for free vibration analysis of hybrid nonlocal Euler-Bernoulli beams with general boundary conditions. For demonstrations, the stiffness and mass matrices of a beam element with Gauss-Lobatto-Legendre (GLL) nodes are explicitly given by using the nodal quadrature method together with the differential quadrature (DQ) law. Convergence studies are performed and comparisons are made with exact solutions to show the excellent behavior of the proposed beam element. Case studies on hybrid nonlocal Euler-Bernoulli beams with different length scale parameters have been conducted. Accurate frequencies of the beams with different combinations of boundary conditions are obtained and presented.

Keywords: Weak form quadrature element method, hybrid nonlocal Euler-Bernoulli beam, multiple boundary conditions, free vibration.

1. Introduction

Due to its efficiency, the continuous mechanics approach is frequently used by researchers to study the behavior of free vibration of micro/nano-sized structures [1]. The nonlocal continuum theory [2-6] and the strain gradient elasticity theory [7-9] are the widely used theories of modeling the micro/nano-scaled structures.

The hybrid nonlocal Euler-Bernoulli beam models, proposed very recently by Lim et al. [10], possess two or more independent small length-scale parameters and may model the micro/nano-structures more accurately. However, it is difficult to get analytical solutions for hybrid nonlocal Euler-Bernoulli beams with general boundary conditions. Therefore, numerical methods should be resorted to for solutions.

Various efficient numerical methods [4,9,11-22] can be employed to get accurate solutions of hybrid nonlocal Euler-Bernoulli beams. The discrete singular convolution (DSC) [11-14], the differential quadrature method (DQM) and differential quadrature element method (DQEM) [15-18] belong to the strong form methods. The finite element method (FEM) [4,9] and the weak form quadrature element method (QEM) [18-22] belong to the weak form methods. If the boundary conditions are not appropriately applied, the DQM may result spurious complex eigen-values [15]. Being a high order FEM, applying multiple boundary conditions by the QEM is very simple. The QEM possesses the accuracy of the global methods such as the DSC, DQM and DQEM as well as the flexibility of the

local methods such as the FEM [20] and thus is used in present investigation. Up to dated research work related to the QEM has been well documented by Wang, Yuan and Jin [20].
The objective of this paper is to propose a novel weak form quadrature beam element for the free vibration analysis of the hybrid nonlocal Euler-Bernoulli beams. The stiffness and mass matrices of a beam element with Gauss-Lobatto-Legendre (GLL) nodes are explicitly given for the first time via the nodal quadrature method together with the differential quadrature (DQ) law. The rate of convergence of the proposed quadrature beam element is studied. Free vibration of hybrid nonlocal Euler-Bernoulli beams with different combinations of boundary conditions is analyzed. Some conclusions are drawn at the end of this paper.

2. Higher-order nonlocal strain gradient theory

Denote x the longitudinal coordinate measured from the middle point of the hybrid nonlocal Euler-Bernoulli beam. Denote I, A, E, ρ and w the second moment of the cross-sectional area, the cross sectional area, Young's modulus, the mass density, and the transverse displacement, respectively.

For the free vibration analysis, the simplified higher-order nonlocal strain gradient theory of the hybrid nonlocal Euler-Bernoulli beam is given by [10,17]

$$EI\frac{d^4w}{dx^4}-l^2EI\frac{d^6w}{dx^6}=\rho A\omega^2w-(ea)^2\rho A\omega^2\frac{d^2w}{dx^2} \tag{1}$$

where symbols l and ea represent the independent length-scale parameters, and ω is the circular frequency.

The shear force, bending moment and high order bending moment are defined as [10,17]

$$Q_x=EI\left(\frac{d^3w}{dx^3}-l^2\frac{d^5w}{dx^5}+\frac{\rho A\omega^2(ea)^2}{EI}\frac{dw}{dx}\right) \tag{2}$$

$$M_x=EI\left(\frac{d^2w}{dx^2}-l^2\frac{d^4w}{dx^4}\right) \tag{3}$$

$$M_{xx}=-l^2EI\frac{d^3w}{dx^3} \tag{4}$$

To obtain the solutions by the weak form quadrature element method (QEM), the expressions of strain energy and kinetic energy are needed for derivations of the stiffness and mass matrices of the quadrature beam element. For free vibration analysis, the corresponding strain energy of the hybrid nonlocal Euler-Bernoulli beam element is given by

$$U=\frac{EI}{2}\int_{-L/2}^{L/2}\left[\left(\frac{d^2w}{dx^2}\right)^2+l^2\left(\frac{d^3w}{dx^3}\right)^2\right]dx \tag{5}$$

where symbol L is the length of the beam element.
The corresponding kinetic energy of the hybrid nonlocal Euler-Bernoulli beam element is given by

$$T=\frac{\rho A\omega^2}{2}\int_{-L/2}^{L/2}\left[(w)^2+(ea)^2\left(\frac{\partial w}{\partial x}\right)^2\right]dx \tag{6}$$

It was pointed out early [17] that the hybrid nonlocal Euler-Bernoulli beam has totally twenty-one combinations of boundary conditions. For the QEM, however, only essential boundary conditions are needed and given. Adopt the notations presented in [17], the essential boundary conditions of the hybrid nonlocal Euler-Bernoulli beam are

(a) Simply supported end-a (S_a):

$$w = 0, \quad \frac{d^2 w}{dx^2} = 0 \tag{7}$$

(b) Simply supported end-b (S_b):

$$w = 0 \tag{8}$$

(c) Clamped end-a (C_a):

$$w = \frac{dw}{dx} = \frac{d^2 w}{dx^2} = 0 \tag{9}$$

(d) Clamped end-b (C_b):

$$w = \frac{dw}{dx} = 0 \tag{10}$$

(e) Free end-a (F_a):

$$\frac{d^2 w}{dx^2} = 0 \tag{11}$$

(f) Free end-b (F_b): all three boundary conditions are natural ones.

3. Formulation of the weak form quadrature beam element

Consider an N-node weak form quadrature beam element. The non-dimensional coordinates of the element node are denoted by ξ_k $(k = 1, 2, ..., N)$, where $\xi = 2x / L$. In present investigation, Gauss-Lobatto-Legendre (GLL) points are used as element nodes for simplicity considerations, and $\xi_k (k = 1, 2, ..., N)$ are the roots of the following equation,

$$\left(1 - \xi^2\right) \frac{dP_{N-1}(\xi)}{d\xi} = 0 \tag{12}$$

where $P_{N-1}(\xi)$ is the (N-1)th order Legendre polynomial.

The weights of nodal quadrature corresponding to integration point ξ_k, i.e., H_k, are given by

$$H_k = \frac{2}{N(N-1)} \quad (k=1,N), \qquad H_k = \frac{2}{N(N-1)\left[P_{N-1}(\xi_k)\right]^2} \quad (k=2,3,...,N-1) \tag{13}$$

Since no explicit formulas exist to compute ξ_k and H_k, the short subroutine listed in reference [20] is used to calculate the GLL points and their corresponding weights conveniently with any *N*.
The displacement function within the quadrature beam element is assumed as

$$\begin{aligned} w(x) &= \varphi_1(x)w(x_1) + \cdots + \varphi_N(x)w(x_N) + \psi_1(x)\left.\frac{dw}{dx}\right|_{x=x_1} + \psi_N(x)\left.\frac{dw}{dx}\right|_{x=x_N} \\ &\quad + \Gamma_1(x)\left.\frac{d^2w}{dx^2}\right|_{x=x_1} + \Gamma_N(x)\left.\frac{d^2w}{dx^2}\right|_{x=x_N} \\ &= \sum_{j=1}^{N}\varphi_j(x)w_j + \psi_1(x)w_1^{(1)} + \psi_N(x)w_N^{(1)} + \Gamma_1(x)w_1^{(2)} + \Gamma_N(x)w_N^{(2)} \\ &= \sum_{j=1}^{N+4} h_j(x)\delta_j \end{aligned} \tag{14}$$

where the shape function $h_j(x)$ is also called Hermite function and its order is (*N*+3), $\delta_j = w_j \ (j=1,2,...,N)$, $\delta_{N+1} = w_1^{(1)}$, $\delta_{N+2} = w_N^{(1)}$, $\delta_{N+3} = w_1^{(2)}$, $\delta_{N+4} = w_N^{(2)}$, $h_{N+1} = \psi_1$, $h_{N+2} = \psi_N$, $h_{N+3} = \Gamma_1$, $h_{N+4} = \Gamma_N$, and $h_j = \varphi_j \ (j=1,2,...,N)$, respectively.
The k^{th} order derivative of the displacement function $w(x)$ with respect to *x* at point *i* is given by

$$\begin{aligned} w^{(k)}(x_i) == \sum_{j=1}^{N+4} h_j^{(k)}(x)\delta_j &= \sum_{j=1}^{N}\varphi_j^{(k)}(x_i)w(x_j) + \psi_1^{(k)}(x_i)w^{(1)}(x_1) + \psi_N^{(k)}(x_i)w^{(1)}(x_N) \\ &\quad + \Gamma_1^{(k)}(x_i)w^{(2)}(x_1) + \Gamma_N^{(k)}(x_i)w^{(2)}(x_N) = \sum_{j=1}^{N+4} Q_{ij}^{(k)}\,\delta_j \quad (i=1,2,...,N) \end{aligned} \tag{15}$$

where $Q_{ij}^{(k)}$ is called the weighting coefficient of the k^{th} order derivative with respect to *x*.
Let $l_j(x)$ be the Lagrange interpolation function defined by

$$l_j(x) = \prod_{\substack{k=1 \\ k\neq j}}^{N} \frac{x - x_k}{x_j - x_k} \tag{16}$$

Then the shape functions of the quadrature beam element are given by [17]

$$\Gamma_j(x) = \frac{1}{2(x_j - x_{N-j+1})^2} l_j(x)(x-x_j)^2(x-x_{N-j+1})^2 \quad (j=1,N) \tag{17}$$

$$\psi_j(x)=\left[\frac{(x-x_{N-j+1})}{(x_j-x_{N-j+1})}\right]^2(x-x_j)l_j(x)-\left[2l_j^{(1)}(x_j)+\frac{4}{x_j-x_{N-j+1}}\right]\Gamma_j(x)\ (j=1,N) \tag{18}$$

$$\begin{aligned}\varphi_j(x)=&\left[\frac{(x-x_{N-j+1})}{(x_j-x_{N-j+1})}\right]^2 l_j(x)-\left[l_j^{(1)}(x_j)+\frac{2}{x_j-x_{N-j+1}}\right]\psi_j(x)\\&-\left[l_j^{(2)}(x_j)+\frac{4l_j^{(1)}(x_j)}{x_j-x_{N-j+1}}+\frac{2}{(x_j-x_{N-j+1})^2}\right]\Gamma_j(x)\qquad (j=1,N)\end{aligned} \tag{19}$$

$$\varphi_j(x)=\left[\frac{(x-x_1)(x-x_N)}{(x_j-x_1)(x_j-x_N)}\right]^2 l_j(x)\qquad (j=2,3,\cdots,N-1) \tag{20}$$

The strain energy of the beam element is obtained by substituting Eq. (14) into Eq. (5) and then integrated numerically using the nodal quadrature method, i.e., the *N*-point GLL quadrature. After doing so, *U* is given by

$$U=\frac{EI}{2}\sum_{k=1}^{N}\frac{LH_k}{2}\left\{\left(\sum_{i=1}^{N+4}Q_{ki}^{(2)}\delta_i\right)\left(\sum_{j=1}^{N+4}Q_{kj}^{(2)}\delta_j\right)+l^2\left(\sum_{i=1}^{N+4}Q_{ki}^{(3)}\delta_i\right)\left(\sum_{j=1}^{N+4}Q_{kj}^{(3)}\delta_j\right)\right\} \tag{21}$$

Elements in the stiffness matrix of the quadrature beam element $[\hat{k}]$ are given by

$$\hat{k}_{ij}=\frac{\partial^2 U}{\partial\delta_i\partial\delta_j}=\sum_{k=1}^{N}\frac{LEIH_k}{2}\left\{Q_{ki}^{(2)}Q_{kj}^{(2)}+l^2Q_{ki}^{(3)}Q_{kj}^{(3)}\right\}\ \ (i,j=1,2,...,N+4) \tag{22}$$

By the same token, the kinetic energy of the beam element is obtained by substituting Eq. (14) into Eq. (6) and then integrated numerically using the nodal quadrature. After doing so, *T* is given by

$$T=\frac{\omega^2\rho A}{2}\sum_{k=1}^{N}\frac{LH_k}{2}\left\{\left(\sum_{i=1}^{N+4}h_{ki}\delta_i\right)\left(\sum_{j=1}^{N+4}h_{kj}\delta_j\right)+(ea)^2\left(\sum_{i=1}^{N+4}Q_{ki}^{(1)}\delta_i\right)\left(\sum_{j=1}^{N+4}Q_{kj}^{(1)}\delta_j\right)\right\} \tag{23}$$

Elements in the consistent mass matrix of the quadrature beam element $[\hat{m}]$ are given by

$$\omega^2\hat{m}_{ij}=\frac{\partial^2 T}{\partial\delta_i\partial\delta_j}=\omega^2\sum_{k=1}^{N}\frac{L\rho AH_k}{2}\left\{h_{ki}h_{kj}+(ea)^2Q_{ki}^{(1)}Q_{kj}^{(1)}\right\}\ \ (i,j=1,2,...,N+4) \tag{24}$$

In Eq. (23) and Eq. (24), h_{ki} and h_{kj} are defined as

$$h_{ki}=h_i(x_k),\ h_{kj}=h_j(x_k) \tag{25}$$

And $Q_{ki}^{(1)}, Q_{kj}^{(1)}, Q_{ki}^{(2)}, Q_{kj}^{(2)}, Q_{ki}^{(3)}, Q_{kj}^{(3)}$ are the weighting coefficients of the first, second and third order derivatives with respect to *x*.

The weighting coefficients of *k*-th order derivative, $Q_{ij}^{(k)}$, can be explicitly computed by [17]

$$\begin{aligned} Q_{ij}^{(k)} = \Gamma_j^{(k)}(x_i) = \frac{1}{2(x_j - x_{N-j+1})^2}\Big\{ & l_j^{(k)}(x_i)(x_i - x_j)^2(x_i - x_{N-j+1})^2 \\ & + 2kl_j^{(k-1)}(x_i)(x_i - x_j)(x_i - x_{N-j+1})^2 + 2kl_j^{(k-1)}(x_i)(x_i - x_j)^2(x_i - x_{N-j+1}) \\ & + 4k(k-1)l_j^{(k-2)}(x_i)(x_i - x_j)(x_i - x_{N-j+1}) + k(k-1)l_j^{(k-2)}(x_i)(x_i - x_j)^2 \\ & + k(k-1)l_j^{(k-2)}(x_i)(x_i - x_{N-j+1})^2 + 2k(k-1)(k-2)l_j^{(k-3)}(x_i)(x_i - x_{N-j+1}) \\ & + 2k(k-1)(k-2)l_j^{(k-3)}(x_i)(x_i - x_j) + k(k-1)(k-2)(k-3)l_j^{(k-4)}(x_i)\Big\} \\ & (i = 1, 2, ..., N;\ j = 1, N) \end{aligned} \tag{26}$$

$$\begin{aligned} Q_{ij}^{(k)} = \psi_j^{(k)}(x_i) = & \Big\{ l_j^{(k)}(x_i)(x_i - x_j)(x_i - x_{N-j+1})^2 + k(k-1)l_j^{(k-2)}(x_i)\Big[2(x_i - x_{N-j+1}) + (x_i - x_j)\Big] \\ & + kl_j^{(k-1)}(x_i)\Big[(x_i - x_{N-j+1})^2 + 2(x_i - x_j)(x_i - x_{N-j+1})\Big] + k(k-1)(k-2)l_j^{(k-3)}(x_i)\Big\}/(x_j - x_{N-j+1})^2 \\ & - \left[2l_j^{(1)}(x_j) + \frac{4}{x_j - x_{N-j+1}}\right]\Gamma_j^{(k)}(x_i) \qquad (i = 1, 2, ..., N;\ j = 1, N) \end{aligned} \tag{27}$$

$$\begin{aligned} Q_{ij}^{(k)} = \varphi_j^{(k)}(x_i) = & \Big\{ l_j^{(k)}(x_i)(x_i - x_{N-j+1})^2 + 2kl_j^{(k-1)}(x_i)(x_i - x_{N-j+1}) + k(k-1)l_j^{(k-2)}(x_i)\Big\}/(x_j - x_{N-j+1})^2 \\ & - \left[l_j^{(1)}(x_j) + \frac{2}{x_j - x_{N-j+1}}\right]\psi_j^{(k)}(x_i) - \left[l_j^{(2)}(x_j) + \frac{4l_j^{(1)}(x_j)}{x_j - x_{N-j+1}} + \frac{2}{(x_j - x_{N-j+1})^2}\right]\Gamma_j^{(k)}(x_i) \\ & (i = 1, 2, ..., N;\ j = 1, N) \end{aligned} \tag{28}$$

$$\begin{aligned} Q_{ij}^{(k)} = \varphi_j^{(k)}(x_i) = \frac{1}{(x_j - x_1)^2(x_j - x_N)^2}\Big\{ & l_j^{(k)}(x_i)(x_i - x_1)^2(x_i - x_N)^2 + 2kl_j^{(k-1)}(x_i)\Big[(x_i - x_1)^2(x_i - x_N) \\ & + (x_i - x_1)(x_i - x_N)^2\Big] + k(k-1)l_j^{(k-2)}(x_i)\Big[(x_i - x_1)^2 + 4(x_i - x_1)(x_i - x_N) + (x_i - x_N)^2\Big] \\ & + 2k(k-1)(k-2)l_j^{(k-3)}(x_i)\Big[(x_i - x_1) + (x_i - x_N)\Big] + k(k-1)(k-2)(k-3)l_j^{(k-4)}(x_i)\Big\} \\ & (i = 1, 2, ..., N;\ j = 2, 3, \cdots, N-1) \end{aligned} \tag{29}$$

In Eqs. (26)-(29), $l_j^{(0)}(x_i) = l_j(x_i) = \delta_{ij}$, $l_j^{(n)}(x_i)$ should be dropped when $n < 0$ since the coefficient associated with it is zero, where $n = (k - i_1)$, $(i_1 = 1, 2, 3)$. Since nodal quadrature is used, $l_j^{(k)}(x_i)$ $(k = 1, 2, 3)$ can be computed explicitly by using the formulas of the DQM as follows [18],

$$l_j^{(1)}(x_i)=\tilde{A}_{ij}=\begin{cases}\dfrac{1}{x_j-x_i}\displaystyle\prod_{\substack{m=1\\ m\neq i,j}}^{N}\dfrac{x_i-x_m}{x_j-x_m} & (i\neq j)\\ \displaystyle\sum_{\substack{m=1\\ m\neq i}}^{N}\dfrac{1}{x_i-x_m} & (i=j)\end{cases}\qquad (i,j=1,2,...,N) \tag{30}$$

And

$$l_j^{(2)}(x_i)=\tilde{B}_{ij}=\sum_{m=1}^{N}\tilde{A}_{im}\tilde{A}_{mj};\ l_j^{(3)}(x_i)=\tilde{C}_{ij}=\sum_{m=1}^{N}\tilde{A}_{im}\tilde{B}_{mj} \tag{31}$$

It is easy to see that $Q_{ij}^{(k)}=0$ when $k>N+3$, since $h_j(x)$ is a $(N+3)$th order polynomial.

If only one element is used to model the entire beam, the equation of motion can be symbolically written as

$$[\hat{k}]\{\delta\}=\omega^2[\hat{m}]\{\delta\} \tag{32}$$

Eliminating the rows and columns in $[\hat{k}]$ and $[\hat{m}]$ in Eq. (32) which correspond to the zero displacements (i.e., the essential boundary conditions) yields

$$[\bar{k}]\{\bar{\delta}\}=\omega^2[\bar{m}]\{\bar{\delta}\} \tag{33}$$

Solving Eq. (33) by a generalized eigen-solver yields the frequencies of the hybrid nonlocal Euler-Bernoulli beam.

If more beam elements are used to model the entire beam structure, the assemblage procedures are exactly the same as the ones of the finite element method [20].

It is worth notice that the problem of spurious complex eigen-values will never occur since both stiffness matrix and mass matrix are symmetric matrices. It is also worth notice that both stiffness and mass matrices are not fully integrated, since the nodal quadrature is only exact for a polynomial of $(2N-3)$th degrees and less. If fully integrated stiffness and mass matrices are required, then Gauss quadrature should be used for efficiency considerations and $Q_{ij}^{(k)}(k=1,2,3)$ at Gauss integration points should be computed differently. More precisely, $l_j^{(k)}(x_i)$ in Eqs. (26)-(29) should be computed differently since the DQ law cannot be directly employed. The method proposed by author's group [19-22] should be used to compute $Q_{ij}^{(k)}(k=1,2,3)$ explicitly and conveniently.

4. Results and discussion

For convenience in presentation, three non-dimensional parameters are introduced, i.e., $\zeta=l/L$, $\tau=ea/L$ and $\lambda=\sqrt{\rho A\omega^2/EI}$. One N-node element is used to model the entire beam for simplicity.

For the S_a-S_a beam, the exact solution of the frequency parameter can be easily obtained by using Navier solution method [17]. The exact non-dimensional frequency parameter is given by

$$\lambda=\frac{n^2\pi^2\sqrt{1+\zeta^2n^2\pi^2}}{\sqrt{1+\tau^2n^2\pi^2}}\ (n=1,2,...) \tag{34}$$

where n is the mode number.
Convergence studies are performed first. The number of nodes N varies from 7 to 19. Figure 1 shows the convergence rate of the proposed element. The S_a-S_a beam with $\zeta = 0.16$ and $\tau = 0.1$ is considered. The absolute differences between the QEM data and analytical solutions are presented. It is seen that the proposed QEM exhibits the exponential rate of convergence.

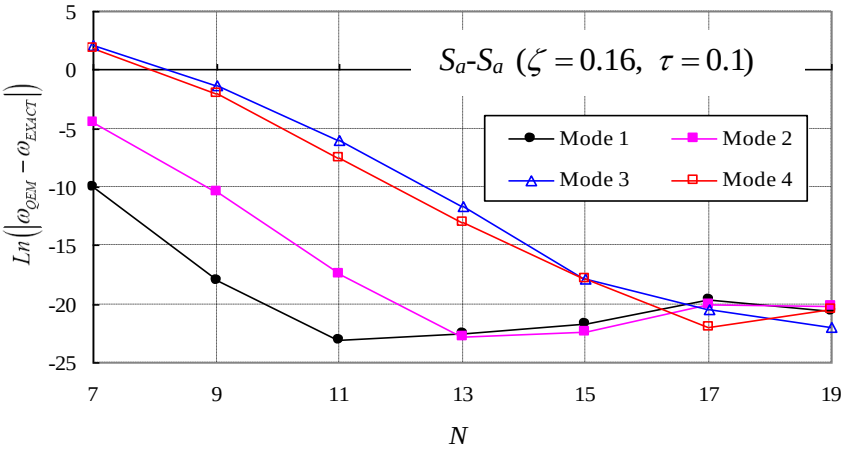

Fig. 1. Convergence rate of the proposed beam element

To demonstrate the high accuracy of the QEM further, the S_b-S_b beam with $\zeta = 0.2$ and $\tau = 0.14$ is analyzed. Since analytical solution is not available, thus the results obtained by the DQEM [17] with N=119 are served as the reference data. Figure 2 shows the variation of the first five frequency parameters with the number of nodes. It is seen that the rate of convergence is high and the QEM with N=13 can yield accurate first five frequency parameters. It was reported early [17] that the DQEM with N=13 can yield accurate first five frequency parameters for the hybrid nonlocal Euler-Bernoulli beam. This indicates that the QEM possesses the same accuracy of the DQEM.

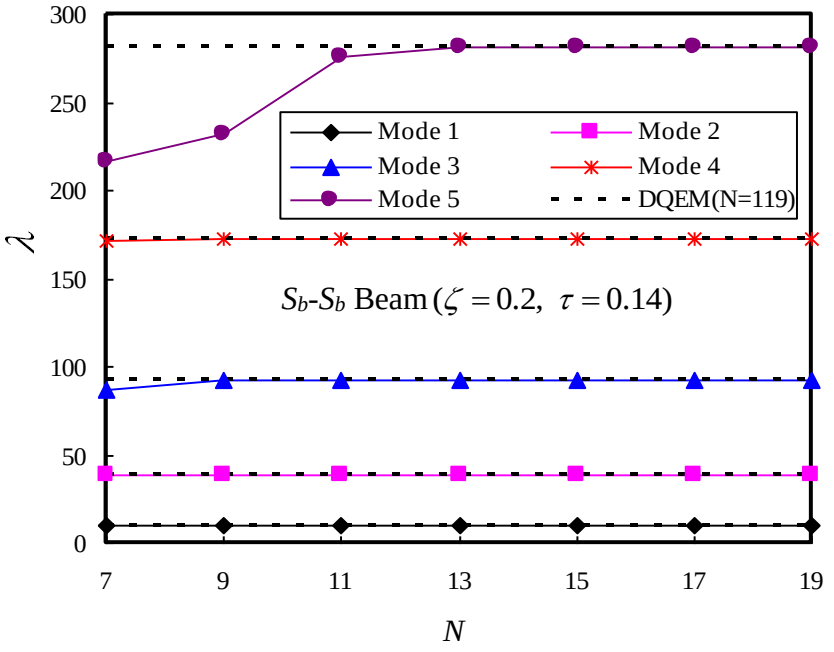

Fig. 2. Convergence of the first five frequency parameters

The variations of the first six frequency parameters of a C_a-F_a beam with one of the small length-scale parameter are shown in Fig. 3. One of the two small length-scale parameters is fixed and the other varies from 0.008 to 0.2.

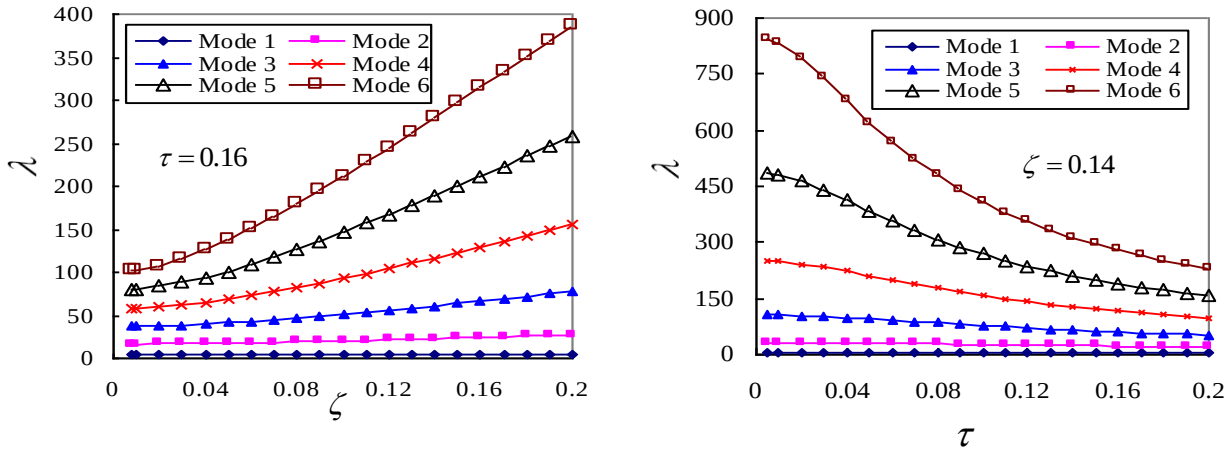

(*a*) (*b*)

Fig.3. Effect of small length-scale parameters on the frequencies of the C_a-F_a beam

To ensure the solution accuracy, the QEM results are obtained by using one 19-node beam element. It is clearly seen that the first six frequency parameters increase with the increase of ζ but decreases with the increase of τ, and the effect of τ and ζ on frequencies is appreciated and opposite. The influence degree is quite different and also increases with the increase of mode numbers. It is easy to get accurate frequencies for beams with other boundary conditions and small length-scale parameter by the proposed QEM. Results are omitted to save the space.

5. Conclusions

A novel weak form quadrature element method is presented for free vibration analysis of hybrid nonlocal Euler-Bernoulli beams. Explicit formulas to compute the element stiffness and mass matrices are given via nodal quadrature and the DQ law. It is shown that the QEM has exponential rate of convergence. Numerical results show that the proposed QEM is computationally efficient and capable of obtaining accurate solutions of the hybrid nonlocal Euler-Bernoulli beams with any combination of boundary conditions and length-scale parameters. It is seen that the effect of the two length-scale parameters on the frequency of the beam is opposite. It is demonstrated that the QEM possesses advantages of the flexibility of the FEM and high accuracy of the DQEM. Present research extends the application range of the weak form quadrature element method.

Acknowledgment

The author acknowledges the support from the Priority Academic Program Development of Jiangsu Higher Education Institutions.

References

[1] Behera, L., Chakraverty, S., Recent researches on nonlocal elasticity theory in the vibration of carbon nanotubes using beam models: A review. *Archives of Computational Methods in Engineering*. 24(3), 481-494, 2017.

[2] Eringen, A.C., On differential equations of nonlocal elasticity and solutions of screw dislocation and surface waves. *Journal of Applied Physics*, 54 (9), 4703-4710, 1983.

[3] Civalek, O., Demir, C., A simple mathematical model of microtubules surrounded by an elastic matrix by nonlocal finite element method. *Applied Mathematics and Computation*, 289, 335-352, 2016.

[4] Demir, C., Civalek, O., A new nonlocal FEM via Hermitian cubic shape functions for thermal vibration of nano beams surrounded by an elastic matrix. *Composite Structures*, 168, 872-884, 2017.

[5] Civalek, O., Demir, C., Bending analysis of microtubules using nonlocal Euler–Bernoulli beam theory. *Applied Mathematical Modeling*, 35, 2053-2067, 2011.

[6] Mercan, K., Civalek, O., Comparison of small scale effect theories for buckling analysis of nanobeams. *International Journal of Engineering & Applied Sciences*, 9(3), 87-97, 2017.

[7] Mindlin, R.D., Micro-structure in linear elasticity. *Archive for Rational Mechanics and Analysis*, 16 (1), 51-78, 1964.

[8] Akgöz, B., Civalek, O., Strain gradient elasticity and modified couple stress models for buckling analysis of axially loaded micro-scaled beams. *International Journal of Engineering Sciences*, 49, 1268-1280, 2011.

[9] Xu, W., Wang, L.F., Jiang, J.N., Strain gradient finite element analysis on the vibration of double-layered graphene sheets. *International Journal of Computational Methods*, 13, 1650011, 2016.

[10] Lim, C.W., Zhang, G., Reddy, J.N.. A higher-order nonlocal elasticity and strain gradient theory and its applications in wave propagation. *Journal of the Mechanics and Physics of Solids*, 78, 298-313, 2015.

[11] Wei, G.W., Discrete singular convolution for the solution of the Fokker-Planck equations. *Journal of Chemical Physics*, 110, 8930-8942, 1999.

[12] Wei, G.W., A new algorithm for solving some mechanical problems. *Computer Methods in Applied Mechanics and Engineering*, 190, 2017-2030, 2001.

[13] Wang, X., Duan, G., Discrete singular convolution element method for static , buckling and free vibration analysis of beam structures. *Applied Mathematics and Computation*, 234, 36-51, 2014.

[14] Wang, X., Yuan, Z., Discrete singular convolution and Taylor series expansion method for free vibration analysis of beams and rectangular plates with free boundaries. *International Journal of Mechanical Sciences*, 122, 184-191, 2017.

[15] Ng, C.H.W., Zhao, Y.B., Xiang, Y., Wei, G.W., On the accuracy and stability of a variety of differential quadrature formulations for the vibration analysis of beams. *International Journal of Engineering & Applied Sciences*, 1(4), 1-25, 2009.

[16] Tornabene, F., Fantuzzi, N., Ubertini, F., Viola, E., Strong formulation finite element method: A survey. *Applied Mechanics Reviews*, 67, 020801,2015.

[17] Wang, X., Novel differential quadrature element method for vibration analysis of hybrid nonlocal Euler-Bernoulli beams. *Applied Mathematics Letters*, 77, 94-100, 2018.

[18] Wang X. *Differential Quadrature and Differential Quadrature Based Element Methods: Theory and Applications*. Oxford: Butterworth-Heinemann, 2015.

[19] Jin, C., Wang, X., Ge, L., Novel weak form quadrature element method with expanded Chebyshev nodes. *Applied Mathematics Letters*, 34, 51-59, 2014.

[20] Wang, X., Yuan, Z., Jin, C., Weak form quadrature element method and its applications in science and engineering: A state-of-the-art review. *Applied Mechanics Reviews*, 69, 030801, 2017.

[21] Jin, C., Wang, X., Accurate free vibration of functionally graded skew plates. *Transactions of Nanjing University of Aeronautics & Astronautics*, 34(2), 188-194, 2017.

[22] Jin, C., Wang, X., Weak form quadrature element method for accurate free vibration analysis of thin skew plates. *Computers and Mathematics with Applications*, 70, 2074-2086, 2015.

International Journal of Engineering & Applied Sciences (IJEAS)
Vol.9, Issue 4 (2017) 76-88
http://dx.doi.org/10.24107/ijeas.357237
Int J Eng Appl Sci 9(4) (2017) 76-88

Numerical Solution of Advection-Diffusion Equation Using Operator Splitting Method

Ersin Bahar [a*], *Gurhan Gurarslan* [b]

[a,b] *Pamukkale University, Department of Civil Engineering, Denizli TR-20070, Turkey*
[*]*E-mail address*: ebahar@pau.edu.tr

ORCID numbers of authors:
0000-0001-8892-8441[a], *0000-0002-9796-3334*[b]

Received date: November 2017
Accepted date: December 2017

Abstract

In this study, effects of operator splitting methods to the solution of advection-diffusion equation are examined. Within the context of this work two operator splitting methods, Lie-Trotter and Strang splitting methods were used and comparisons were made through various Courant numbers. These methods have been implemented to advection-diffusion equation in one-dimension. Numerical solutions of advection and dispersion processes were carried out by a characteristics method with cubic spline interpolation (MOC-CS) and Crank-Nicolson (CN) finite difference scheme, respectively. Obtained results were compared with analytical solutions of the problems and available methods in the literature. It is seen that MOC-CS-CN method has lower error norm values than the other methods. MOC-CS-CN produces accurate results even while the time steps are great.

Keywords: Advection-diffusion equation, Operator splitting methods, Method of characteristics, Finite difference

1. Introduction

Rivers, lakes and other natural waters have been the drain place of urban and industrial wastes since the early days of civilization. In the early days, the amount and composition of these wastes were not at very important levels, so they did not have a negative effect on aquatic environments. However, rapid population growth, rising living standards and the development of the industry have led to an increase in the amount of pollution discharged into the aquatic environment. In order to reduce or eliminate this pollution, the pollutant transport processes represented by the advection-diffusion equation should be well understood and the processes to be carried out should be adapted to the nature of these processes [1]. The one-dimensional mathematical expression of the advection-diffusion equation without the source term is as follows

$$\frac{\partial C}{\partial t} + U\frac{\partial C}{\partial x} = D_x \frac{\partial^2 C}{\partial x^2} \tag{1}$$

Where t is time, x is spatial coordinate, C is concentration of substance, U is velocity of the flow and D is diffusion coefficient. We denote the spatial and temporal step sizes by Δx and Δt, respectively. Also Courant number, Cr, is computed as $U\Delta t/\Delta x$ and the Peclet number, Pe, is obtained as $U\Delta x/D_x$.

Although advection and diffusion are simultaneous processes, they have very different effects on mass transport. The advection process is only influenced by the past, and it occurs along the characteristic line. However, the diffusion process takes place between the characteristic lines, which will be influenced by both the past and present conditions. This means that there is a need for a numerical method that simultaneously solves both hyperbolic term (advection) and parabolic term (dispersion). There is no numerical method that can completely overcome of this problem [2]. So the great effort has been made on developing the efficient and stable numerical techniques.

Holly and Usseglio-Polatera [3] developed a sensitive numerical method to model the contaminant dispersion in two-dimensional tidal currents. This method uses the approach of high-order bi-cubic Hermite interpolation with characteristics in the solution of the advection part. The Crank-Nicolson scheme was used for the diffusion part in the study. Chen and Falconer [4] used a modified QUICK finite difference scheme for water quality modeling in rivers and coastal waters. Also, they did stability analysis of the modified method. Szymkiewicz [5] solved advection-diffusion equation with the help of Lie-Trotter operator splitting method. Cubic spline interpolation and standard Galerkin finite element method were used for advection and diffusion processes, respectively. Ahmad and Kothyari [6] proposed a new numerical scheme for the solution of the pure advection process. The basis of the proposed method is based on the backward time-line characteristics approach. Tsai et al. [7] investigated effects of the endpoint constraints which are used in the characteristics method with cubic spline interpolation, on the solution of advection process. Verma et al. [8], with the help of Lie-Trotter operator splitting method, used the MacCormack scheme and the Crank-Nicolson finite difference scheme for the solution of the advection and diffusion processes, respectively. Tian and Ge [9] have developed an exponential fourth-order compact alternating direction implicit method in which Crank-Nicolson scheme used for time discretization and an exponential fourth-order compact difference formula used for spatial discretization. Sari et al. [10] proposed high-order finite difference schemes for the solution of a one-dimensional advection-diffusion equation. Schemes are derived from Taylor series expansion. To get the solutions, they have integrated the fourth-order Runge-Kutta scheme in time with the finite difference schemes up to the tenth order in space. Gurarslan et al. [11] have produced numerical solutions to a one-dimensional advection-diffusion equation using a Runge-Kutta scheme of fourth-order and a compact finite difference scheme of sixth-order in space. In the study by Gurarslan [12], numerical simulations of the advection-dispersion equation were performed with high-order compact finite difference schemes. Compact finite difference schemes were used in conjunction with MacCormack and Runge-Kutta schemes to obtain solutions with the accuracy of sixth-order.

In this study, appropriate schemes will be used for the physical structures of the advection-diffusion problem. Advection process and diffusion process will be solved by characteristics method with cubic spline interpolation (MOC-CS) and the Crank-Nicolson scheme (CN), respectively. These two different methods will be combined through operator splitting methods. For this purpose, first-order Lie-Trotter and second-order Strang-Marchuk operator splitting methods which are frequently used in the literature were chosen and effects of them on the solution will be examined for a one-dimensional problem with sharp structure. The obtained results will be compared with the analytical solution of the test problem and the results in the literature.

2. Solution Procedures with Different Operator Splitting Methods

The mathematical representations of Lie-Trotter and Strang-Marchuk operator splitting methods and when they are applied to advection-diffusion equation, solution procedures will be explained in the next sections.

2.1. Lie-Trotter Operator Splitting Method

The Lie-Trotter operator splitting method is a first-order operator splitting method and named as a sequential splitting method. By applying this method to the advection-diffusion equation, the problem is divided into two sub-problems: advection and diffusion. The application of the Lie-Trotter separation method to Eq. (1) is as follows

$$\frac{\partial \hat{C}_1}{\partial t} + U\frac{\partial \hat{C}_1}{\partial x} = 0, \qquad \hat{C}_1(t_n, x) = C(t_n, x), \qquad t \in [t_n, t_{n+1}] \tag{2}$$

$$\frac{\partial \hat{C}_2}{\partial t} = D_x\frac{\partial^2 \hat{C}_2}{\partial x^2}, \qquad \hat{C}_2(t_n, x) = \hat{C}_1(t_{n+1}, x), \qquad t \in [t_n, t_{n+1}] \tag{3}$$

Where $\hat{C}_1$ is the concentration in the advection process and $\hat{C}_2$ is the concentration in the diffusion process. Eq. (2) and Eq. (3) represents the pure advection equation and diffusion equation, respectively. In the solution process, Eq. (2) will be solved for a time interval of Δt using the initial condition of Eq. (1). The result obtained from there will be the initial condition of Eq. (3). Then Eq. (3) will be solved for a time interval of Δt and the solution of Eq. (1) will be obtained for a time interval Δt. Thus, the problems will be solved consecutively by combining them with the initial conditions [13].

2.2. Strang-Marchuk Operator Splitting Method

The Strang-Marchuk operator splitting method is a second-order operator splitting method. By applying this method to Eq. (1), the problem will be divided into two sub-problems, namely advection and diffusion, similar to the Lie-Trotter operator splitting method. But this time these sub-problems will be solved in three steps in total. The application of the Strang-Marchuk opeator splitting method to Eq. (1) is as follows

$$\frac{\partial \hat{C}_1}{\partial t} + U\frac{\partial \hat{C}_1}{\partial x} = 0, \qquad \hat{C}_1(t_n, x) = C(t_n, x), \qquad t \in \left[t_n, t_{n+1/2}\right] \tag{4}$$

$$\frac{\partial \hat{C}_2}{\partial t} = D_x\frac{\partial^2 \hat{C}_2}{\partial x^2}, \qquad \hat{C}_2(t_n, x) = \hat{C}_1\left(t_{n+1/2}, x\right), \qquad t \in [t_n, t_{n+1}] \tag{5}$$

$$\frac{\partial \hat{C}_1}{\partial t} + U\frac{\partial \hat{C}_1}{\partial x} = 0, \qquad \hat{C}_1\left(t_{n+1/2}, x\right) = \hat{C}_2(t_{n+1}, x), \qquad t \in \left[t_{n+1/2}, t_{n+1}\right] \tag{6}$$

Where Eq. (4) will be solved for a time interval of $\Delta t/2$ using the initial condition of Eq. (1). The solution of Eq. (4) will be used as the initial condition of Eq. (5) and Eq. (5) will be solved for a time interval of Δt. The obtained result of Eq. (5) will be the initial condition of Eq. (6). Lastly, Eq. (6) will solved for a time interval of $\Delta t/2$. Thus, the solution of Eq. (1) will be obtained for a time interval of Δt [13].

3. Method of Characteristics for Advection Process

The method of characteristics approach is frequently used in the solution of advection process. This is because as the other schemes it does not have time and spatial discretization errors but only the error of the interpolation method. This is achieved by converting the pure advection equation in Eq. (2) into two ordinary differential equations. If both sides of Eq. (2) are multiplied by dt, this equation can be written in total derivative form. In this case, Eq. (2) can be represented by the following two ordinary differential equations.

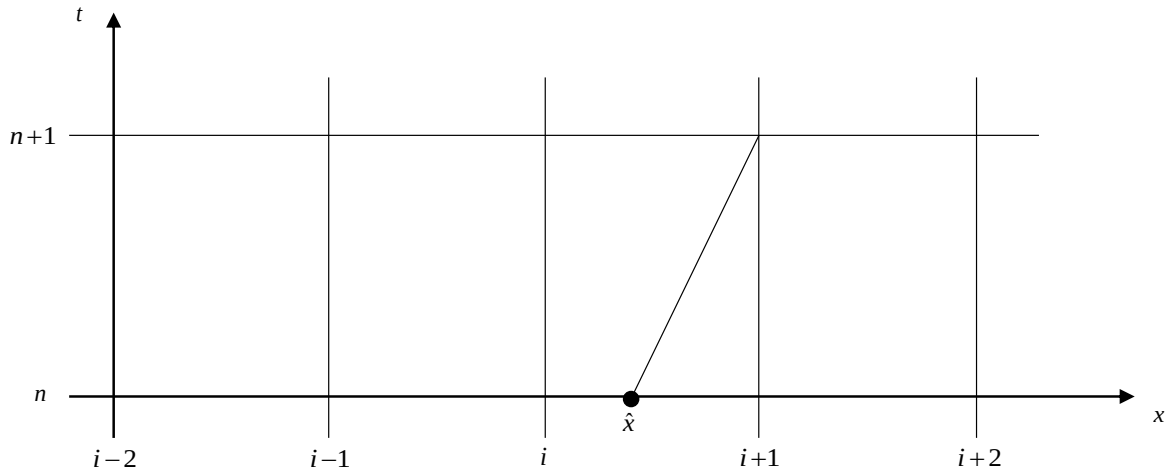

Fig. 1. Finite difference grid structure and trajectory of concentration particle in one-dimension

$$\frac{d\hat{C}_1}{dt} = 0 \tag{7}$$

$$\frac{dx}{dt} = U \tag{8}$$

Integration of the Eq. (7) and Eq. (8) yields

$$\hat{C}_1\big|_{\hat{x},n} = \hat{C}_1\big|_{i+1,n+1} \tag{9}$$

Along

$$x_{i+1} - \hat{x} = U\Delta t = Cr\Delta x \tag{10}$$

When the finite difference grid structure is generated for solution domain as can be seen from Fig. 1, each node representing concentration value can be taken as a concentration particle. We know the concentration particle moves with the velocity of the flow in the advection process, so we can follow its trajectory which is given by Eq. (8) and can be seen in Fig. 1. $\hat{C}_1\big|_{i+1,n+1}$ is the concentration value that needs to be calculated. $\hat{C}_1\big|_{\hat{x},n}$ is the concentration value at point $\hat{x}$ between nodes. As we know from Eq. (9) those values are equal. Therefore we need an interpolation method to calculate the concentration value at $\hat{x}$ by using the concentration values at all nodal points at time level n. The accuracy of the solution depends on the order of the

interpolation method. In this study cubic spline interpolation method is picked because of its high-order accuracy [22].

Cubic splines use third-order polynomials generated at each interval for interpolation. Suppose there are $M+1$ data points $\left(x_1, \hat{C}_1\big|_{1,n}\right), \ldots, \left(x_{M+1}, \hat{C}_1\big|_{M+1,n}\right)$ so that there are M intervals and thus M cubic polynomials. The general expression a cubic polynomial is as follows

$$P_i(x) = \alpha_i + \beta_i(x - x_i) + \gamma_i(x - x_i)^2 + \theta_i(x - x_i)^3, \quad i = 1,2, \ldots, M \tag{11}$$

Where $\alpha_i, \beta_i, \gamma_i, \theta_i$ are the coefficients that should be calculated. Since we have M cubic polynomials and there are 4 unknown coefficients in each polynomial, we need $4M$ equations so that these coefficients can be calculated. These equations derived based on the adjacent splines agree at interior knots and also first and second derivatives of the adjacent splines agree at interior knots.

$$P_M(x_{M+1}) = \hat{C}_1\big|_{M+1,n} \tag{12}$$

$$P_i(x_i) = \hat{C}_1\big|_{i,n}, \qquad i = 1,2, \ldots, M \tag{13}$$

The established polynomials must provide the concentration values at those points as stated in Eq. (12) and Eq. (13).

$$P_i(x_{i+1}) = P_{i+1}(x_{i+1}), \qquad i = 1,2, \ldots, M-1 \tag{14}$$

$$P_i'(x_{i+1}) = P_{i+1}'(x_{i+1}), \qquad i = 1,2, \ldots, M-1 \tag{15}$$

$$P_i''(x_{i+1}) = P_{i+1}''(x_{i+1}), \qquad i = 1,2, \ldots, M-1 \tag{16}$$

Eqs. (14-16) represent the equality of the concentration values and first and second derivatives of polynomials at interior knots of adjacent splines. In this way $4M-2$ equations are created. The last 2 equations that we need will be obtained from the boundary condition. As we know there are various boundary conditions, the natural boundary condition will be used in this study.

$$\begin{aligned} P_1''(x_1) &= 0 \\ P_M''(x_{M+1}) &= 0 \end{aligned} \tag{17}$$

Eq. (17) represents the assumptions made in the natural boundary condition. The second derivative in the first and last points equals to zero. Thus 4M equations are obtained. First, $P_i(x_i) = \alpha_i$ $(i = 1,2, \ldots, M)$ found from Eq. (11). By integrating this with Eq. (13)

$$\alpha_i = \hat{C}_1\big|_{i,n}, \qquad i = 1,2, \ldots, M \tag{18}$$

Eq. (18) obtained. We define the distance between the nodes as $h_i = x_{i+1} - x_i$ $(i = 1,2, \ldots, M)$ and the following equations are obtained when all unknown coefficients are written in γ.

$$\begin{gathered}\gamma_1 = 0 \\ \gamma_{i-1}h_{i-1} + 2\gamma_i(h_i + h_{i-1}) + \gamma_{i+1}h_i = K_1 - K_2, \quad i = 2,3,\dots,M \\ \gamma_{M+1} = 0\end{gathered} \tag{19}$$

Where

$$K_1 = \frac{3\left(\hat{C}_1\big|_{i+1,n} - \hat{C}_1\big|_{i,n}\right)}{h_i} \tag{20}$$

$$K_2 = \frac{3\left(\hat{C}_1\big|_{i,n} - \hat{C}_1\big|_{i-1,n}\right)}{h_{i-1}} \tag{21}$$

As seen in Eq. (19), the first and last γ coefficients are calculated by natural boundary condition. The γ coefficients at the other points form a tri-diagonal matrix system consisting of $M-1$ equations. As this system can effectively be solved by the Thomas algorithm, the γ coefficients at all points are calculated easily. The values of α coefficients are given in Eq. (18). The calculations of the remaining β and θ coefficients with the help of the γ coefficients are as follows

$$\beta_i = \frac{\hat{C}_1\big|_{i+1,n} - \hat{C}_1\big|_{i,n}}{h_i} - \frac{1}{3}(2\gamma_i + \gamma_{i+1})h_i, \qquad i = 1,2,\dots,M \tag{22}$$

$$\theta_i = \frac{\gamma_{i+1} - \gamma_i}{3h_i}, \qquad i = 1,2,\dots,M \tag{23}$$

Thus, a total of M cubic polynomials are obtained. A detailed description of the arrangements is available from the work of Esfandiari [14].

4. Crank-Nicolson Scheme for Diffusion Process

The Crank-Nicolson scheme is an implicit scheme and gives quite accurate results in the solution of the diffusion equation. The application to the diffusion equation given in Eq. (3) is as follows

$$\begin{gathered}\frac{\hat{C}_2\big|_{i,n+1} - \hat{C}_2\big|_{i,n}}{\Delta t} \\ = \frac{D}{2(\Delta x)^2}\left(\hat{C}_2\big|_{i+1,n} - 2\hat{C}_2\big|_{i,n} + \hat{C}_2\big|_{i-1,n}\right) \\ + \frac{D}{2(\Delta x)^2}\left(\hat{C}_2\big|_{i+1,n+1} - 2\hat{C}_2\big|_{i,n+1} + \hat{C}_2\big|_{i-1,n+1}\right)\end{gathered} \tag{24}$$

The values at time level n are known and the values at time level $n+1$ are unknown. By gathering the known values to the right side and the unknown values to the left side in the Eq. (24), the following equation is obtained.

$$a_i \hat{C}_2\big|_{i-1,n+1} + b_i \hat{C}_2\big|_{i,n+1} + c_i \hat{C}_2\big|_{i+1,n+1} = f_i \tag{25}$$

The coefficients in Eq. (25)

$$a_i = \frac{D\Delta t}{2(\Delta x)^2} \tag{26}$$

$$b_i = -\frac{D\Delta t}{(\Delta x)^2} - 1 \tag{27}$$

$$c_i = \frac{D\Delta t}{2(\Delta x)^2} \tag{28}$$

$$f_i = -\hat{C}_2\big|_{i,n} - \frac{D\Delta t}{2(\Delta x)^2}\left(\hat{C}_2\big|_{i+1,n} - 2\hat{C}_2\big|_{i,n} + \hat{C}_2\big|_{i-1,n}\right) \tag{29}$$

Eq. (25) forms a tridiagonal system of equations. This system can be solved effectively by the Thomas algorithm [15].

5. Numerical Application

In this section, a sharp structure one-dimensional advection-diffusion equation will be solved with different operator splitting methods which combine MOC-CS and CN. Effects of operator splitting methods will be examined for various Courant numbers. Obtained results will be compared with solutions available in the literature and exact solution. In addition, the accuracy of the methods will be evaluated by calculating the error norms. The error norms are calculated as follows.

$$L_\infty = \max_i \left| C_i^{exact} - C_i^{numerical} \right| \tag{30}$$

$$L_2 = \sqrt{\sum_{i=1}^{M+1} \left| C_i^{exact} - C_i^{numerical} \right|^2} \tag{31}$$

Example: Velocity of the flow and diffusion coefficient are taken as $U = 0.01\ m/s$ and $D = 0.002\ m^2/s$ in this experiment. Length of the channel picked as $L = 100\ m$. The analytic solution of this problem can be obtained by solving the following equation [5].

$$C(x,t) = \frac{1}{2} erfc\left(\frac{x - Ut}{\sqrt{4Dt}}\right) + \frac{1}{2} exp\left(\frac{Ux}{D}\right) erfc\left(\frac{x + Ut}{\sqrt{4Dt}}\right) \tag{32}$$

The used boundary conditions in the solution are as follows

$$C(0,t) = 1 \tag{33}$$

$$-D\left(\frac{\partial C}{\partial x}\right)(L,t) = 0 \tag{34}$$

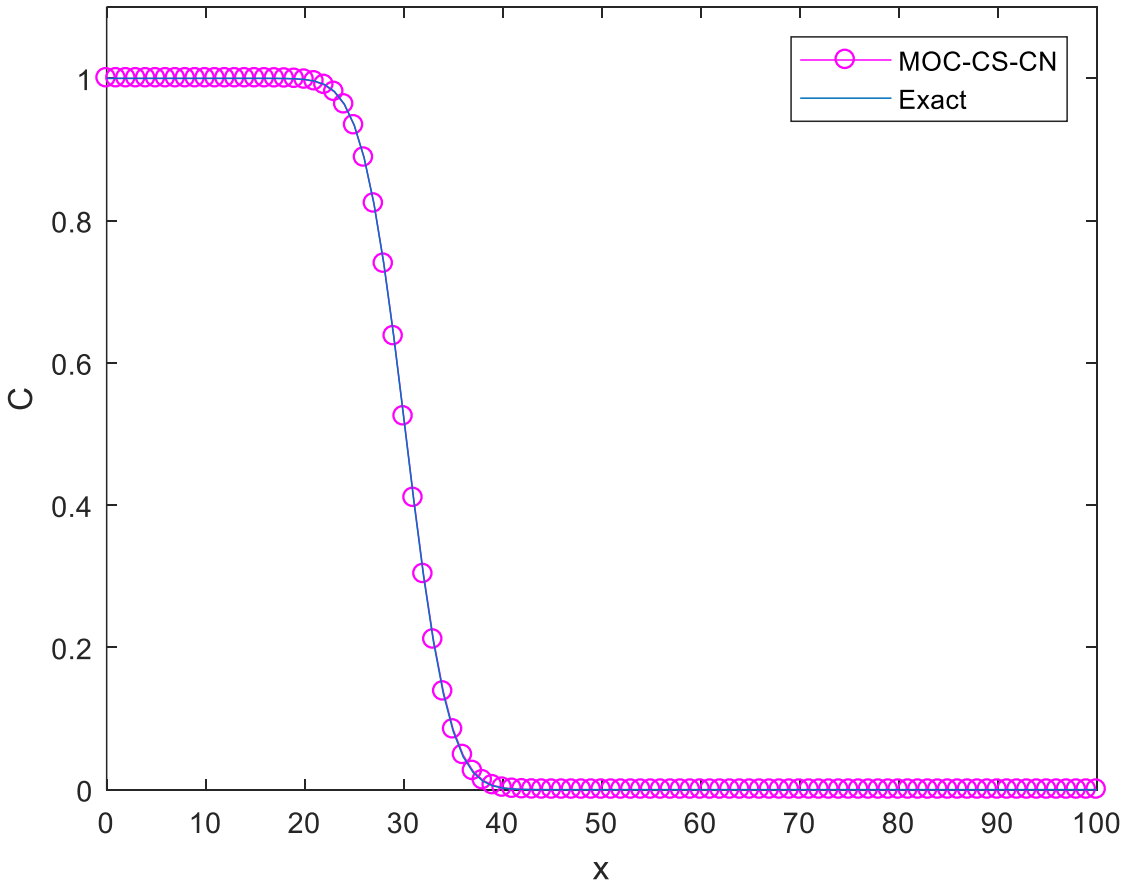

Fig. 2. Comparison of the exact and the numerical solution obtained with MOC-CS-CN method for $\Delta x = 1\ m$ and $\Delta t = 10\ s$

Initial condition of the problem can be obtained from the exact solution. In all calculations spatial step size picked as $\Delta x = 1\ m$. Fig. 2 shows that comparison of exact solution and numerical solution with MOC-CS-CN method for time interval of $\Delta t = 10$. As it clearly can be seen there is an excellent agreement between numerical solution and exact solution. As shown in Fig. 2, when the maximum calculation time is $3000\ s$, the critical concentration values are between 18 and 42 m. Therefore, the values at these points will be compared.

Since the problem has a sharp structure, obtaining close results to the analytical solution is very difficult. For this reason, calculations start from a small time interval. The calculations in Table 1 were made for $\Delta t = 1$. Almost all of the methods have found the same values as the analytical solution. There is also no visible difference between operator splitting methods. For this reason, the time interval will be gradually enlarged until this difference appears to be clear.

The calculations in Table 2 were made for $\Delta t = 10$. This small change in time interval is enough for other methods to start to get away from the analytical solution. When the calculated concentration values are compared it seems clear that the MOC-CS-CN method has the closest

results to the analytical solution and lowest error norms for both operator splitting methods. Thus, it has become clear how effective is the MOC-CS-CN method in sharp problems. In addition, the effect of operator splitting methods on the solution seems to appear.

Table 1. Comparison of obtained solution with exact and numerical solutions in the literature ($\Delta t = 1\ s$)

x (m)	[12] MC-CD6	[11] RK4-CD6	[16] CuTBSM	MOC-CS-CN		Exact
				Lie-Trotter	Strang	
0	1.000	1.000	1.000	1.000	1.000	1.000
18	1.000	1.000	1.000	1.000	1.000	1.000
19	0.999	0.999	0.999	0.999	0.999	0.999
20	0.998	0.998	0.998	0.998	0.998	0.998
21	0.996	0.996	0.996	0.996	0.996	0.996
22	0.991	0.991	0.991	0.990	0.990	0.991
23	0.982	0.982	0.982	0.981	0.981	0.982
24	0.964	0.964	0.964	0.963	0.963	0.964
25	0.935	0.934	0.934	0.933	0.933	0.934
26	0.889	0.889	0.888	0.888	0.888	0.889
27	0.824	0.823	0.822	0.823	0.823	0.823
28	0.739	0.738	0.736	0.738	0.738	0.738
29	0.637	0.636	0.635	0.635	0.635	0.636
30	0.523	0.523	0.522	0.522	0.522	0.523
31	0.408	0.408	0.408	0.408	0.408	0.408
32	0.301	0.301	0.301	0.301	0.301	0.301
33	0.208	0.208	0.208	0.209	0.209	0.208
34	0.135	0.135	0.136	0.137	0.137	0.135
35	0.082	0.082	0.082	0.084	0.084	0.082
36	0.047	0.046	0.046	0.048	0.048	0.046
37	0.025	0.024	0.024	0.026	0.026	0.024
38	0.012	0.012	0.012	0.013	0.013	0.012
39	0.005	0.005	0.005	0.006	0.006	0.005
40	0.002	0.002	0.002	0.003	0.003	0.002
41	0.001	0.001	0.001	0.001	0.001	0.001
42	0.000	0.000	0.000	0.000	0.000	0.000
L_2	0.0017	0.0017	-	0.0046	0.0046	-
L_∞	0.0008	0.0008	-	0.0019	0.0019	-

The calculated L_∞ error values are compared with other errors in the literature for different time intervals in Table 3. Except for the error of extended cubic B-spline collocation method at $\Delta t = 1\ s$, MOC-CS-CN always has smaller error values. In addition, the increase of the time interval makes the effect of the operator splitting method more noticeable. It is clear that the Strang splitting method improves the quality of the solution.

Table 2. Comparison of obtained solution with exact and numerical solutions in the literature ($\Delta t = 10\ s$)

x (m)	[12] MC-CD6	[11] RK4-CD6	[16] CuTBSM	MOC-CS-CN Lie-Trotter	MOC-CS-CN Strang	Exact
0	1.000	1.000	1.000	1.000	1.000	1.000
18	1.000	1.000	1.000	1.000	1.000	1.000
19	0.999	0.999	0.999	0.999	0.999	0.999
20	0.998	0.998	0.998	0.998	0.998	0.998
21	0.996	0.996	0.996	0.996	0.996	0.996
22	0.991	0.992	0.991	0.991	0.991	0.991
23	0.982	0.982	0.982	0.981	0.981	0.982
24	0.965	0.965	0.963	0.963	0.963	0.964
25	0.936	0.936	0.933	0.934	0.934	0.934
26	0.891	0.891	0.885	0.889	0.889	0.889
27	0.827	0.827	0.818	0.824	0.824	0.823
28	0.743	0.743	0.732	0.739	0.739	0.738
29	0.642	0.641	0.631	0.637	0.637	0.636
30	0.529	0.528	0.517	0.525	0.524	0.523
31	0.414	0.413	0.404	0.410	0.410	0.408
32	0.306	0.306	0.298	0.303	0.302	0.301
33	0.213	0.212	0.207	0.211	0.210	0.208
34	0.138	0.138	0.134	0.138	0.138	0.135
35	0.084	0.084	0.081	0.085	0.084	0.082
36	0.048	0.048	0.045	0.049	0.049	0.046
37	0.025	0.025	0.023	0.026	0.026	0.024
38	0.012	0.012	0.011	0.013	0.013	0.012
39	0.006	0.006	0.005	0.006	0.006	0.005
40	0.002	0.002	0.002	0.003	0.003	0.002
41	0.001	0.001	0.001	0.001	0.001	0.001
42	0.000	0.000	0.000	0.000	0.000	0.000
L_2	0.0148	0.0142	-	0.0073	0.0064	-
L_∞	0.0060	0.0055	-	0.0028	0.0025	-

Table 3. Comparison of L_∞ error norms ($\Delta x = 1\ m$)

Δt (s)	[17] BSCM	[17] ECuBSCM	MOC-CS-CN Lie-Trotter	MOC-CS-CN Strang
60	0.04330	0.04250	0.01942	0.01180
30	0.01962	0.01961	0.00828	0.00567
20	0.01270	0.01260	0.00512	0.00376
10	0.00685	0.00608	0.00284	0.00251
5	0.00409	0.00307	0.00222	0.00212
1	0.00224	0.00127	0.00188	0.00187

The calculations in Table 4 were made for $\Delta t = 60$. Examining Table 4, it can be seen that none of the methods have found close results to the exact solution. This indicates that selected time interval is quite large. When the results of the operator splitting methods are compared, the improvement provided by the Strang operator splitting method is clearly visible. But this improvement was not enough.

Table 4. Comparison of obtained solution with exact and numerical solutions in the literature ($\Delta t = 60\ s$)

x (m)	[18]	[5]	[19]	[20]		[21]		MOC-CS-CN		Exact
	MOCS	MOCG	CBSG	FEMLSF	FEMQSF	TC	TG	Lie-Trotter	Strang	
0	1.000	1.000	1.000	1.000	1.000	1.000	1.000	1.000	1.000	1.000
18	1.000	1.000	1.000	1.000	1.000	1.000	1.000	1.000	1.000	1.000
19	1.000	0.999	1.000	1.000	1.000	0.999	0.999	0.999	0.999	0.999
20	1.000	0.998	0.999	0.999	1.000	0.999	0.998	0.998	0.998	0.998
21	1.000	0.996	0.996	0.997	0.999	0.999	0.996	0.996	0.996	0.996
22	1.000	0.990	0.991	0.993	0.996	0.998	0.991	0.992	0.991	0.991
23	1.000	0.978	0.981	0.985	0.989	0.994	0.980	0.983	0.982	0.982
24	1.000	0.957	0.961	0.970	0.974	0.987	0.960	0.967	0.965	0.964
25	1.000	0.922	0.927	0.943	0.946	0.972	0.926	0.940	0.937	0.934
26	0.996	0.870	0.874	0.902	0.900	0.945	0.874	0.897	0.893	0.889
27	1.013	0.799	0.800	0.842	0.832	0.902	0.800	0.836	0.830	0.823
28	1.047	0.708	0.706	0.763	0.743	0.838	0.705	0.754	0.747	0.738
29	0.897	0.602	0.596	0.666	0.638	0.755	0.595	0.654	0.647	0.636
30	0.457	0.488	0.479	0.556	0.524	0.653	0.479	0.542	0.535	0.523
31	0.067	0.375	0.366	0.442	0.411	0.541	0.366	0.427	0.420	0.408
32	-0.036	0.272	0.265	0.332	0.306	0.427	0.264	0.318	0.312	0.301
33	-0.010	0.185	0.181	0.235	0.218	0.320	0.181	0.222	0.218	0.208
34	0.002	0.118	0.118	0.156	0.147	0.227	0.117	0.146	0.143	0.135
35	0.000	0.070	0.072	0.096	0.095	0.152	0.072	0.090	0.088	0.082
36	0.000	0.038	0.042	0.055	0.058	0.096	0.041	0.052	0.051	0.046
37	0.000	0.020	0.023	0.030	0.034	0.057	0.023	0.028	0.027	0.024
38	0.000	0.009	0.012	0.015	0.019	0.032	0.012	0.014	0.014	0.012
39	0.000	0.004	0.006	0.007	0.010	0.017	0.006	0.007	0.006	0.005
40	0.000	0.002	0.003	0.003	0.005	0.008	0.002	0.003	0.003	0.002
41	0.000	0.001	0.001	0.001	0.003	0.004	0.001	0.001	0.001	0.001
42	0.000	0.000	0.001	0.000	0.001	0.001	0.000	0.001	0.000	0.000
L_2	-	-	-	-	-	-	-	0.0479	0.0300	-
L_∞	-	-	-	-	-	-	-	0.0194	0.0118	-

6. Conclusions

This paper deals with the solution of advection-diffusion equation based on operator splitting approach. Two different operator splitting methods were used such as Lie-Trotter and Strang-Marchuk. The solutions of advection process and diffusion process were obtained by the method of characteristics with cubic spline and Crank-Nicolson scheme, respectively. These two different methods integrated through operator splitting methods and effects of them on the solution examined by a one-dimensional advection-diffusion problem which has a sharp

structure. The examination has been done by comparing error norm values and comparison with other results available in the literature. As a result, the MOC-CS-CN method achieved very good results. It has almost identical results when Δt is small. Also it has been observed that the Strang operator splitting method improves the quality of the result when the time interval increases. In future studies, it is considered to extend this method to multi-dimensional problems by operator splitting methods.

7. References

[1] Srivastava, R., *Flow Through Open Channels*, Oxford University Press, 2008.

[2] Baptista, A. E. De M., *Solution of Advection-Dominated Transport by Eulerian-Lagrangian Methods Using the Backward Method of Characteristics*, Ph.D Thesis, MIT, Cambridge, 1987.

[3] Holly, F.M., Usseglio-Polatera, J., Dispersion simulation in two-dimensional tidal flow. *Journal of Hydraulic Engineering*, 110(7), 905–926, 1984.

[4] Chen, Y., Falconer, R.A., Advection-diffusion modelling using the modified QUICK scheme. *International Journal for Numerical Methods in Fluids*, 15(10), 1171–1196, 1992.

[5] Szymkiewicz, R., Solution of the advection-diffusion equation using the spline function and finite elements. *Communications in Numerical Methods in Engineering*, 9, 197–206, 1993.

[6] Ahmad, Z., Kothyari, U.C., Time-line cubic spline interpolation scheme for solution of advection equation. *Computers and Fluids*, 30(6), 737–752, 2001.

[7] Tsai, T.L., Yang, J.C., Huang, L.H., Characteristics method using cubic–spline interpolation for advection–diffusion equation. *Journal of Hydraulic Engineering*, 130(6), 580–585, 2004.

[8] Verma, P., Prasad, K.S.H., Ojha, C.S.P., MacCormack scheme based numerical solution of advection-dispersion equation. *ISH Journal of Hydraulic Engineering*, 12(1), 27-38, 2006.

[9] Tian, Z.F., Ge, Y.B., A fourth-order compact ADI method for solving two-dimensional unsteady convection-diffusion problems. *Journal of Computational and Applied Mathematics*, 198(1), 268–286, 2007.

[10] Sari, M., Gürarslan, G., Zeytinoğlu, A., High-order finite difference schemes for solving the advection-diffusion equation. *Mathematical and Computational Applications*, 15(3), 449–460, 2010.

[11] Gurarslan, G., Karahan, H., Alkaya, D., Sari, M., Yasar, M., Numerical solution of advection-diffusion equation using a sixth-order compact finite difference method. *Mathematical Problems in Engineering*, vol. 2013, Article ID 672936, 7 pages, 2013.

[12] Gurarslan, G., Accurate simulation of contaminant transport using high-order compact finite difference schemes. *Journal of Applied Mathematics*, 2014, 1–8, 2014.

[13] Hundsdorfer, W., Verwer, J., *Numerical Solution of Time-Dependent Advection-Diffusion-Reaction Equations*, Springer-Verlag Berlin Heidelberg, 2003.

[14] Esfandiari, R.S., *Numerical Methods for Engineers and Scientists Using MATLAB*, New York: Taylor and Francis Group, 2013.

[15] Lam, C.Y., *Applied Numerical Methods for Partial Differential Equations*, Singapore, Simon and Schuster, 1994.

[16] Nazir, T., Abbas, M., Izani, A., Abd, A., The numerical solution of advection-diffusion problems using new cubic trigonometric B-splines approach. *Applied Mathematical Modelling*, 40(7–8), 4586–4611, 2016.

[17] Irk, D., Dag, I., Tombul, M., Extended cubic B-spline solution of the advection-diffusion equation. *KSCE Journal of Civil Engineering*, 19(4), 929-934, 2015.

[18] Holly, F.M., Preissmann, A., Accurate calculation of transport in two dimensions. *Journal of Hydraulic Division*, 103(11), 1259-1277, 1977.
[19] Gardner, L.R.T. and Dag, I., A Numerical Solution of the Advection-Diffusion Equation Using B-Spline Finite Element, *Proceedings International AMSE Conference*, Lyon, France, 109-116, 1994.
[20] Dag, I., Irk, D., Tombul, M., Least-squares finite element method for the advection-diffusion equation. *Applied Mathematics and Computation*, 173(1), 554–565, 2006.
[21] Dag, I., Canivar, A., Sahin, A., Taylor-Galerkin method for advection-diffusion equation. *Kybernetes*, 40(5/6), 762–777, 2011.
[22] Bahar, E., *Numerical Solution of Advection-Dispersion Equation Using Operator Splitting Method*, Denizli: Pamukkale University, (in Turkish) 2017.

International Journal of Engineering & Applied Sciences (IJEAS)
Vol.9, Issue 4 (2017) 89-99
http://dx.doi.org/10.24107/ijeas.362242
Int J Eng Appl Sci 9(4) (2017) 89-99

Buckling Analysis of Non-Local Timoshenko Beams by Using Fourier Series

Hayrullah Gün Kadıoğlu [a*], *Mustafa Özgür Yaylı* [b]

[a,b] *Uludağ University, Faculty of Engineering, Department of Civil Engineering, Bursa, Turkey.*
[*]*E-mail address*: hyrllh_1113@hotmail.com

ORCID numbers of authors:
0000-0001-7370-2722[a], *0000-0003-2231-170X*[b]

Received date: December 2017
Accepted date: December 2017

Abstract

In this study, buckling analysis of a nano sized beam has been performed by using Timoshenko beam theory and Eringen's nonlocal elasticity theory. Timoshenko beam theory takes into account not only bending moment but also shear force. Therefore, it gives more accurate outcomes than Euler Bernoulli beam theory. Moreover, Eringen's nonlocal elasticity theory takes into account the small scale effect. Thus, these two theories are utilized in this study. The vertical displacement function is chosen as a Fourier sine series. Similarly, the rotation function is chosen as a Fourier cosine series. These functions are enforced by Stokes' transformation, and higher order derivatives of them are obtained. These derivatives are written in the governing equations for the buckling of nonlocal Timoshenko beams. Hence Fourier coefficients are acquired. Subsequently boundary condition of established beam model is identified with Timoshenko beam and Eringen's nonlocal elasticity theories, and the linear equations are obtained. A coefficients matrix is created by utilizing these linear systems of equations. When determinant of this coefficient matrix is calculated, the critical buckling loads are acquired. Finally, achieved outcomes are compared with other studies in the literature. Calculated results are also presented in a series of figures and tables

Keywords: Timoshenko beam theory, Eringen's nonlocal elasticity theory, elastic buckling analysis, Stokes' transformation, Fourier series.

1. Introduction

Nano derives from a Greek word meaning dwarf. A nanometer is a unit of length equal to one billionth of a meter. Nanotechnology being with manipulation of substance on an atomic, molecular, and supramolecular scale is a new science. This new science aims to create a lot of new materials which occurs from many different atoms combined. Therefore the emphasis of nanotech. is increasing step by step. A lot of researches being associated with nanotech. are made in the literature. These researches are made by three methods. These are synthesis, simulation and theoretical. Cost of synthesis and simulation are utmost large. Hence theoretical method is utilized commonly. In this study, buckling analysis of nano sized beams has examined by theoretically. Thus Timoshenko beam and Eringen's nonlocal elasticity theories are utilized together. Timoshenko beam theory is more advanced a version of Euler Bernoulli beam theory. In the Euler Bernoulli beam theory, influence of shear on bending deformation is considered negligible compared to bending moment. Therefore plane sections remain plane and normal to the longitudinal axis during bending deformation. However, in the reality, influence of shear on bending deformation cannot be neglected. Thus Timoshenko beam theory regarding not solely moment but also shear effect gives more realistic

outcomes than Euler Bernoulli beam theory. Moreover Eringen's nonlocal elasticity theory takes into account the small scale effect.

Once the literature is investigated closely, it is observed that. There are a lot of studies being associated with nonlocal elasticity theory. Studies regarding nonlocal elasticity theory found in the literature are compiled and presented in this part. In order to explain the small scale effect, the nonlocal continuum mechanics has been utilized in [1-3]. Moreover Atomistic simulations and experimental findings have proved a significant small scale effect in the mechanic performance of material at micro and nano scale [4-6]. The long term repercussions of these studies on engineering and science have been felt. Thus many investigators have implemented nonlocal elasticity theory for their studies being associated with bending, buckling and vibration [7-36].

In this study, on the basis of the higher order elasticity theory known as nonlocal elasticity theory, an analytical method is presented for the buckling analysis of nano sized Timoshenko beams with rotational restraints. The vertical displacement function is sought as a Fourier cosine series and the slope of the beam is represented as Fourier sine series. Then Stokes' transformation is used to take care of the rotational restraints. A coefficient matrix including shear correction factor and rotational spring parameters is obtained. The eigen values of this matrix gives the buckling loads. Present results are compared with the similar problem solutions available in the literature.

2. Formulation of the Problem

According to the nonlocal Timoshenko beam theory, governing equations are given [7];

$$EI\frac{\partial^2\theta}{\partial z^2}+\gamma^2 P\frac{\partial^3\varphi}{\partial z^3}-\kappa_S GA\left(\theta+\frac{\partial\varphi}{\partial z}\right)=0 \tag{1}$$

$$\kappa_S GA\left(\frac{\partial\theta}{\partial z}+\frac{\partial^2\varphi}{\partial z^2}\right)-P\frac{\partial^2\varphi}{\partial z^2}=0 \tag{2}$$

where, E is modulus of elasticity, I is moment of inertia of beam, G is modulus of elasticity in shear, A is cross sectional area, κ_s is Timoshenko shear coefficient, P is critical buckling load, γ is small-scale effect coefficient φ is the vertical displacement function, θ is the rotation function.

In Ref. [7] and [8], the solution of above equations has been presented for rigid boundary conditions. On the other hand, difference of this study from the other studies is that. This study allows to make solution for non-rigid boundary conditions. Therefore the long term repercussions of this study on engineering and science will be felt.

2.1. Fourier Series

The displacement and rotation functions can be indicated as following Fourier series.

$$\varphi=\sum_{n=1}^{\infty}A_n\sin(\alpha_n z)\qquad 0<z<L \tag{3}$$

$$\theta=\sum_{n=1}^{\infty}B_n\cos(\alpha_n z)\qquad 0<z<L \tag{4}$$

Where

$$\alpha_n = \frac{n\pi}{L} \tag{5}$$

In which L is length of beam, A_n and B_n is Fourier coefficients.

2.2. Stokes' Transformation

In order to include non-rigid boundary conditions in the solution of problem a mathematical transform is necessary. Therefore, in this study, Fourier series and Stokes' transformations are utilized together and included to the solution of the problem with the deformable boundary conditions.

$$A_n = \frac{2}{L}\int_0^L \varphi(z)\, sin(\alpha_n z) \tag{6}$$

The first derivative of the displacement function yields;

$$\varphi'(z) = \sum_{n=1}^{\infty} \alpha_n A_n\, cos(\alpha_n z) \tag{7}$$

The above function can be exhibited as a Fourier cosine series;

$$\varphi'(z) = \frac{f_0}{2} + \sum_{n=1}^{\infty} f_n\, cos(\alpha_n z) \tag{8}$$

In the equation (8), f_0 and f_n coefficients are indicated as follows.

$$f_0 = \frac{2}{L}\int_0^L \varphi'(z)\, \partial z = \frac{2}{L}\,(\varphi(L) - \varphi(0)) \tag{9}$$

$$f_n = \frac{2}{L}\int_0^L \varphi'(z)\, cos(\alpha_n z)\partial z \quad n = 1,2,3 \ldots \tag{10}$$

Finally, if partial integration is applied;

$$f_n = \frac{2}{L}\,[\varphi(z)\, cos(\alpha_n z)]_0^L + \frac{2}{L}\,[\alpha_n \int_0^L \varphi(z)\, sin(\alpha_n z)\partial z] \tag{11}$$

$$f_n = \frac{2}{L}\,[(1)^n\, \varphi(L)\,) - \varphi(0)] + A_n \alpha_n \tag{12}$$

The steps followed above are recognized as Stokes' transformations. Higher order derivatives can be found out similarly. Up until the fourth order, resulting derivatives of the displacement function are obtained to be as following.

$$\frac{\partial\varphi(z)}{\partial z}=\frac{(\varphi_L-\varphi_0)}{L}+\sum_{n=1}^{\infty}cos(\alpha_n z)(\frac{2((-1)^n\varphi_L-\varphi_0)}{L}+\alpha_n A_n) \tag{13}$$

$$\frac{\partial^2\varphi(z)}{\partial z^2}=-\sum_{n=1}^{\infty}\alpha_n sin(\alpha_n z)(\frac{2((-1)^n\varphi_L-\varphi_0)}{L}+\alpha_n A_n) \tag{14}$$

$$\frac{\partial^3\varphi(z)}{\partial z^3}=\frac{(\varphi_L''-\varphi_0'')}{L}+\sum_{n=1}^{\infty}cos(\alpha_n z)[\frac{2}{L}(\varphi_L''(-1)^n-\varphi_0'')-{\alpha_n}^2(\frac{2}{L}(\varphi_L(-1)^n-\varphi_0)+\alpha_n A_n)] \tag{15}$$

$$\frac{\partial^4\varphi(z)}{\partial z^4}=-\sum_{n=1}^{\infty}sin(\alpha_n z)[\frac{2}{L}({\varphi_L}''(-1)^n-{\varphi_0}'')-{\alpha_n}^2(\frac{2}{L}(\varphi_L(-1)^n-\varphi_0)+\alpha_n A_n)]\alpha_n \tag{16}$$

The first derivative of the rotation function yields;

$$\theta'(z)=-\sum_{n=1}^{\infty}\alpha_n B_n sin(\alpha_n z) \tag{17}$$

In order to display the above function as a Fourier cosine series, the second derivative of the rotation function is necessary to be calculated;

$$\theta''(z)=-\sum_{n=1}^{\infty}{\alpha_n}^2 B_n cos(\alpha_n z) \tag{18}$$

If the steps followed for the displacement function are similarly applied for the rotation function up until the third order, resulting derivatives of the rotation function are obtained to be as following.

$$\frac{\partial\theta(z)}{\partial z}=-\sum_{n=1}^{\infty}\alpha_n B_n sin(\alpha_n z) \tag{19}$$

$$\frac{\partial^2\theta(z)}{\partial z^2}=\frac{(\theta_L'-\theta_0')}{L}+\sum_{n=1}^{\infty}cos(\alpha_n z)(\frac{2((-1)^n\theta_L'-\theta_0')}{L}-{\alpha_n}^2 B_n) \tag{20}$$

$$\frac{\partial^3\theta(z)}{\partial z^3}=\sum_{n=1}^{\infty}\alpha_n sin(\alpha_n z)(\frac{2({\theta_0}'-{\theta_L}'(-1)^n)}{L}+{\alpha_n}^2 B_n) \tag{21}$$

2.3. Fourier Coefficients

Taking the first derivative of the equation (1);

$$EI\frac{\partial^3\theta}{\partial z^3}+\gamma^2 P\frac{\partial^4\varphi}{\partial z^4}-\kappa_S GA\left(\frac{\partial\theta}{\partial z}+\frac{\partial^2\varphi}{\partial z^2}\right)=0 \tag{22}$$

If the equations (14), (16), (19) and (21) are written in the equations (2) and (22);

$$EI\left(\frac{2(\theta_0' - \theta_L'(-1)^n)}{L} + \alpha_n{}^2 B_n\right)\alpha_n sin(\alpha_n z) - \gamma^2 P\left[\frac{2}{L}(\varphi_L''(-1)^n - \varphi_0'') - \alpha_n{}^2\left(\frac{2}{L}(\varphi_L(-1)^n - \varphi_0) + \alpha_n A_n\right)\right]\alpha_n sin(\alpha_n z) - \kappa_S GA(-\alpha_n B_n sin(\alpha_n z) - \alpha_n sin(\alpha_n z)\left(\frac{2((-1)^n\varphi_L - \varphi_0)}{L} + \alpha_n A_n\right)) = 0 \quad (23)$$

$$\kappa_S GA(-\alpha_n B_n sin(\alpha_n z) - \alpha_n sin(\alpha_n z)\left(\frac{2((-1)^n\varphi_L - \varphi_0)}{L} + \alpha_n A_n\right)) + P\alpha_n sin(\alpha_n z)\left(\frac{2((-1)^n\varphi_L - \varphi_0)}{L} + \alpha_n A_n\right) = 0 \quad (24)$$

A_n and B_n are derived from these equations when φ_0 and φ_L are equal to zero.

$$A_n = -\frac{2AG\kappa_S(P\gamma^2\varphi_0'' + EI\theta_0' + (-1)^{n+1}(P\gamma^2\varphi_L'' + EI\theta_L'))}{EILP\alpha_n{}^3 + AGL\kappa_S\alpha_n(P + (-EI + P\gamma^2)\alpha_n{}^2)} \quad (25)$$

$$B_n = -\frac{2(P - AG\kappa_S)(P\gamma^2\varphi_0'' + EI\theta_0' + (-1)^{n+1}(P\gamma^2\varphi_L'' + EI\theta_L'))}{EILP\alpha_n{}^2 + AGL\kappa_S(P + (-EI + P\gamma^2)\alpha_n{}^2)} \quad (26)$$

2.4. Boundary Conditions

Flexural moment function M(x) of nonlocal Timoshenko beams is shown as following [7].

$$M = EI\frac{\partial\theta}{\partial z} + P\gamma^2\frac{\partial^2\varphi}{\partial z^2} \quad (27)$$

If the equation (27) is written in the equations (25) and (26);

$$A_n = -\frac{2AG\kappa_S(M_0 + (-1)^{n+1}(M_L))}{EILP\alpha_n{}^3 + AGL\kappa_S\alpha_n(P + (-EI + P\gamma^2)\alpha_n{}^2)} \quad (28)$$

$$B_n = -\frac{2(P - AG\kappa_S)(M_0 + (-1)^{n+1}(M_L))}{EILP\alpha_n{}^2 + AGL\kappa_S(P + (-EI + P\gamma^2)\alpha_n{}^2)} \quad (29)$$

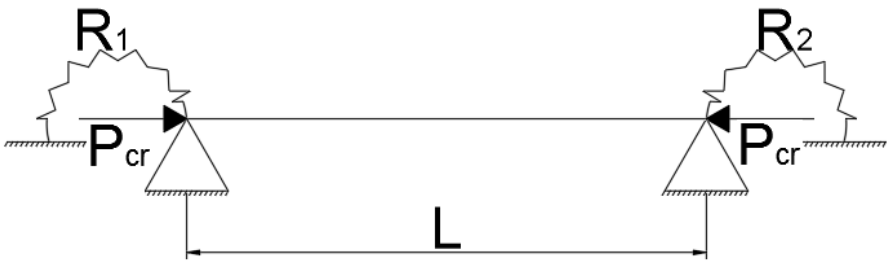

Fig. 1. The figure, displaying boundary conditions.

Flexural moment function M(x) can be shown in the form;

$$M = \theta R \quad \rightarrow \quad M - \theta R = 0, \tag{30}$$

where R is stiffness of the rotational springs.

2.5. Construction of Coefficients Matrix

If z=0 and $\alpha_n=n\pi/L$ are written in the equation (30);

$$0 = M_0 + \sum_{n=1}^{\infty} R_1 \left(\frac{2(P - AG\kappa_S)(M_0 + (-1)^{n+1}(M_L))}{EILP(\frac{n\pi}{L})^2 + AGL\kappa_S(P + (-EI + P\gamma^2)(\frac{n\pi}{L})^2)} cos\frac{n\pi}{L}z) \right) \tag{31}$$

If z=L and $\alpha_n=n\pi/L$ are written in the equation (30);

$$0 = M_L + \sum_{n=1}^{\infty} R_2 \left(\frac{2(P - AG\kappa_S)(M_0 + (-1)^{n+1}(M_L))}{EILP(\frac{n\pi}{L})^2 + AGL\kappa_S(P + (-EI + P\gamma^2)(\frac{n\pi}{L})^2)} \cos\frac{n\pi}{L}z) \right) \tag{32}$$

Two equations are obtained dependent on M_0 and M_L. Thus coefficients matrix is composed.

$$\begin{bmatrix} \Phi_{11} & \Phi_{12} \\ \Phi_{21} & \Phi_{22} \end{bmatrix} \begin{bmatrix} M_0 \\ M_L \end{bmatrix} = 0 \tag{33}$$

Where Φ_{11}, Φ_{12}, Φ_{21} and Φ_{22} parameters are given the below.

$$\Phi_{11} = -1 - \sum_{n=1}^{\infty} \frac{2LR_1(P - AG\kappa_S)}{EIP\pi^2 n^2 + AG(PL^2 + \pi^2 n^2(-EI + P\gamma^2))\kappa_S} \tag{34}$$

$$\Phi_{12} = \sum_{n=1}^{\infty} \frac{2(-1)^n LR_1(P - AG\kappa_S)}{EIP\pi^2 n^2 + AG(PL^2 + \pi^2 n^2(-EI + P\gamma^2))\kappa_S} \tag{35}$$

$$\Phi_{21} = -1 - \sum_{n=1}^{\infty} \frac{2LR_2(P - AG\kappa_S)}{EIP\pi^2 n^2 + AG(PL^2 + \pi^2 n^2(-EI + P\gamma^2))\kappa_S} \tag{36}$$

$$\Phi_{22} = \sum_{n=1}^{\infty} \frac{2(-1)^n LR_2(P - AG\kappa_S)}{EIP\pi^2 n^2 + AG(PL^2 + \pi^2 n^2(-EI + P\gamma^2))\kappa_S} \tag{37}$$

3. Numerical results

The equation (33) is an eigenvalue problem. The critical buckling loads can be calculated by setting the determinant of the coefficient matrix to zero. The characteristic equation can be achieved by assigning the proper values of (R_1) and (R_2) corresponding to the restrained boundary condition. If R_1=0 and R_2=0, the beam is pinned ended beam. If R_1=0 and R_2=∞, the beam is clamped pinned beam. If R_1=∞ and R_2=∞, the beam is clamped ended beam. κ_s =0.9 for Timoshenko beam, κ_s =∞ for Euler Bernoulli beam.

With the theoretical formulation proposed in this study, different numerical examples are solved in this part. Firstly, accuracy and validity of the present mathematical approach is validated. Validation study is given in Tables 1-2.

Several numerical examples are solved numerically. Tabulated values given in the Table 1 are plotted in the Figs 2-4. The Fourier sine and cosine series are truncated for 50 terms of infinite series. It can be seen from these figures, the nonlocal effects are more pronounced for higher buckling modes.

Table 1. Critical buckling loads Pcr(nN) for pinned, clamped–pinned and clamped beams with diverse small scale coefficients γ(nm) and length-to-diameter ratios L/d in this study.
d=1nm, A= $\pi^2/4$ nm², I= π /64 nm⁴, E=1000kPa, G=420.168kPa

γ(nm)	0		0.5		1		1.5		2	
L/d	T	EB	T	EB	T	EB	T	EB	T	EB
					Pinned ended beam					
10	4.7670	4.8447	4.6540	4.7281	4.3450	4.4095	3.9121	3.9644	3.4333	3.4735
12	3.3267	3.3644	3.2713	3.3077	3.1156	3.1486	2.8865	2.9149	2.6172	2.6405
14	2.4514	2.4718	2.4212	2.4411	2.3348	2.3533	2.2038	2.2202	2.0432	2.0574
16	1.8805	1.8925	1.8626	1.8744	1.8111	1.8222	1.7313	1.7414	1.6306	1.6396
18	1.4878	1.4953	1.4766	1.4840	1.4440	1.4511	1.3928	1.3993	1.3269	1.3329
					Clamped-pinned beam					
10	9.6851	10.01	9.2298	9.5258	8.0890	8.3155	6.7074	6.8624	5.4130	5.5135
12	6.7934	6.9525	6.5662	6.7147	5.9675	6.0899	5.1803	5.2723	4.3727	4.4381
14	5.0215	5.1079	4.8963	4.9784	4.5555	4.6685	4.0820	4.1388	3.5643	3.6067
16	3.8599	3.9107	3.7855	3.8343	3.5785	3.6221	3.2796	3.3163	2.9363	2.9656
18	3.0581	3.0899	3.0112	3.0421	2.8788	2.9069	2.6821	2.7066	2.4481	2.4684
					Clamped ended beam					
10	18.542	19.777	16.942	17.967	13.458	14.097	10.023	10.373	7.3846	7.5729
12	13.127	13.734	12.304	12.836	10.357	10.731	8.1958	8.4284	6.3426	6.4810
14	9.7591	10.090	9.2970	9.5974	8.1406	8.3700	6.7428	6.8995	5.4361	5.5374
16	7.5298	7.7256	7.2517	7.4332	6.5283	6.6751	5.5977	5.7053	4.6665	4.7410
18	5.9813	6.1042	5.8045	5.9202	5.3316	5.4291	4.6943	4.7696	4.0213	4.0765

Table 2. In Ref. [7], critical buckling loads Pcr(nN) for pinned, clamped–pinned and clamped beams with diverse small scale coefficients γ(nm) and length-to-diameter ratios L/d.
d=1nm, A= $\pi^2/4$ nm², I= π /64 nm⁴, E=1000kPa, G=420.168kPa

γ	0		0.5		1		1.5		2	
L/d	T	EB	T	EB	T	EB	T	EB	T	EB
					Pinned ended beam					
10	4.7670	4.8447	4.6540	4.7281	4.3450	4.4095	3.9121	3.9644	3.4333	3.4735
12	3.3267	3.3644	3.2713	3.3077	3.1156	3.1486	2.8865	2.9149	2.6172	2.6405
14	2.4514	2.4718	2.4212	2.4411	2.3348	2.3533	2.2038	2.2202	2.0432	2.0574
16	1.8805	1.8925	1.8626	1.8744	1.8111	1.8222	1.7313	1.7414	1.6306	1.6396
18	1.4878	1.4953	1.4766	1.4840	1.4440	1.4511	1.3928	1.3993	1.3269	1.3329
					Clamped-pinned beam					
10	9.5605	9.9155	9.1179	9.4349	8.0055	8.2461	6.6520	6.8151	5.3782	5.4830
12	6.7118	6.8858	6.4904	6.6496	5.9059	6.0363	5.1348	5.2321	4.3410	4.4096
14	4.9638	5.0589	4.8416	4.9297	4.5086	4.5844	4.0448	4.1052	3.5355	3.5811
16	3.8168	3.8715	3.7441	3.7967	3.5418	3.5885	3.2490	3.2880	2.9120	2.9431
18	3.0248	3.0603	2.9789	3.0121	2.8493	2.8795	2.6567	2.6828	2.4270	2.4489
					Clamped ended beam					
10	18.192	19.379	16.649	17.638	13.273	13.894	9.9200	10.263	7.3283	7.5137
12	12.874	13.458	12.082	12.594	10.199	10.562	8.0964	8.3233	6.2829	6.4187
14	9.5687	9.8872	9.1240	9.4132	8.0077	8.2296	6.6514	6.8038	5.3765	5.4756
16	7.3818	7.5699	7.1143	7.2889	6.4168	6.5585	5.5155	5.6199	4.6092	4.6819
18	5.8631	5.9811	5.6931	5.8043	5.2375	5.3315	4.6212	4.6942	3.9675	4.0212

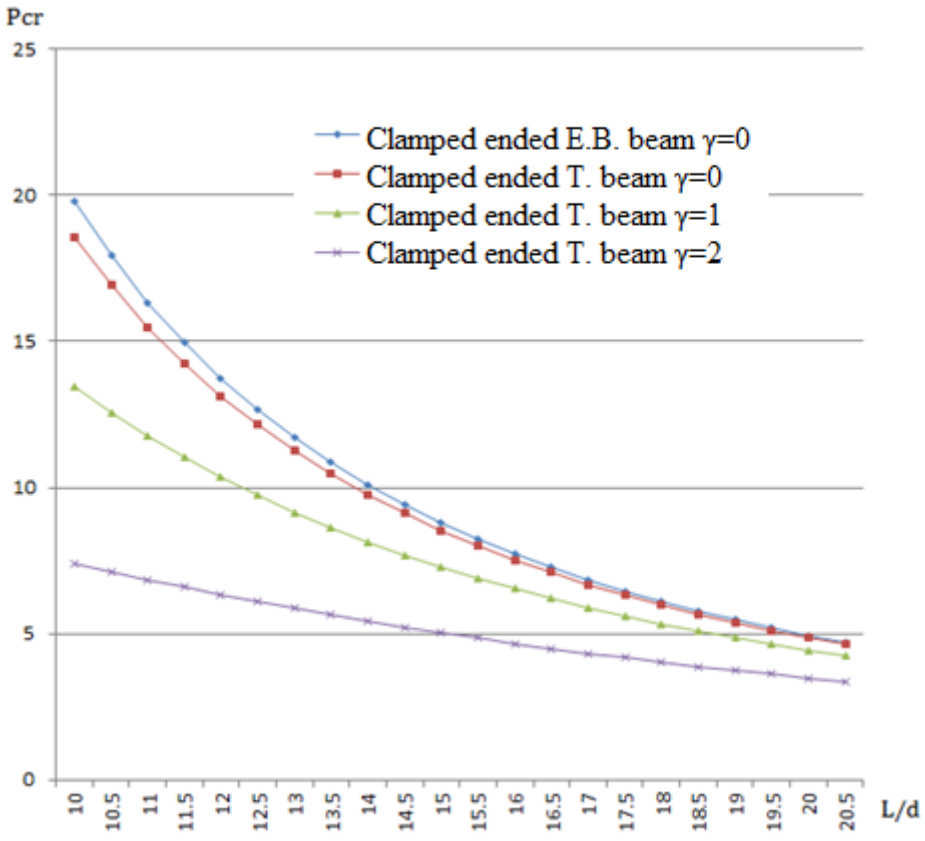

Fig. 2. Variations of critical buckling load for clamped ended beam.

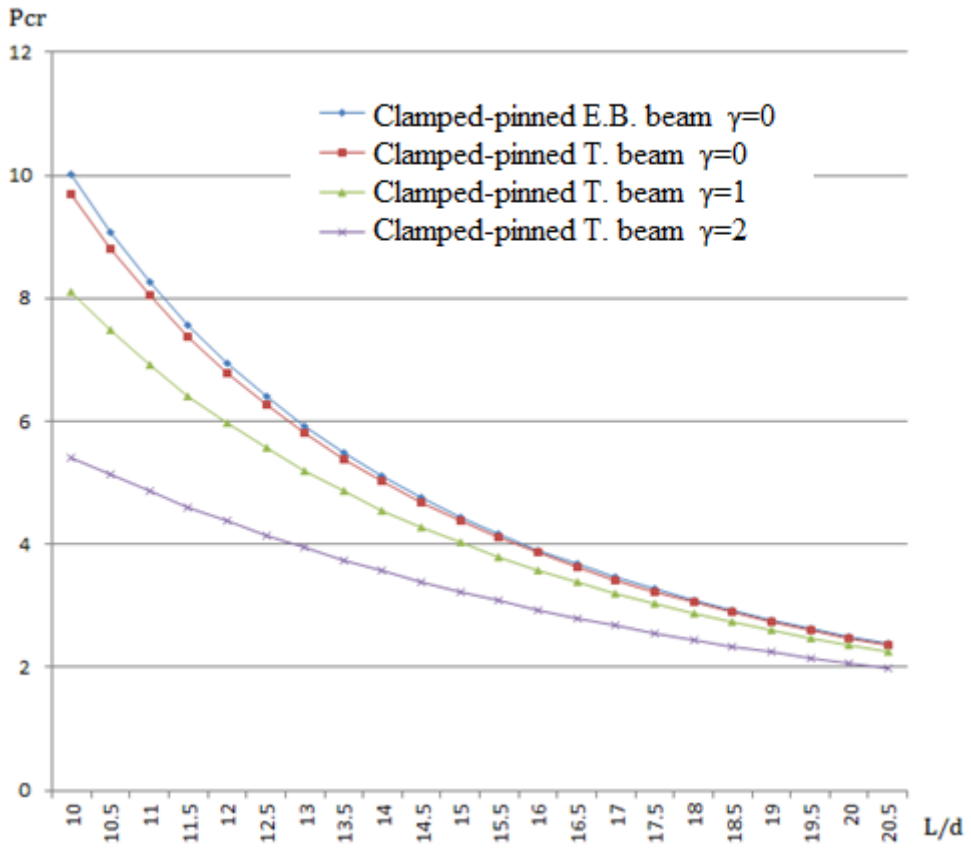

Fig. 3. Variations of critical buckling load for clamped pinned beam.

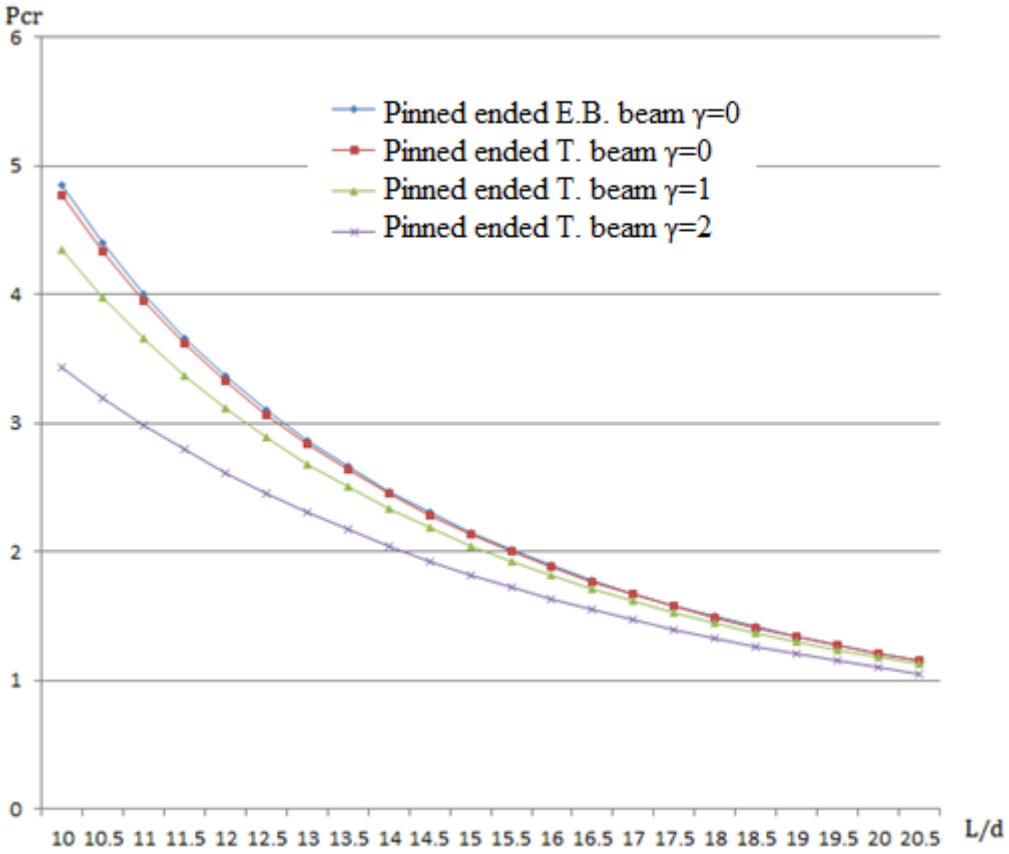

Fig. 4. Variations of critical buckling load for pinned ended beam.

4. Conclusions

The critical buckling loads are found by using nonlocal elasticity theory for the Timoshenko and Euler Bernoulli beams. If the critical buckling loads of the Timoshenko and Euler Bernoulli beams are compared between each other, it is observed that. Once length-to-diameter ratios decline, results diverge from each other. Once length-to-diameter ratios increase, results converge to each other. Even if the results converge to each other. The critical buckling loads of the Timoshenko beams are always lower than the Euler Bernoulli beams. Because, in the Timoshenko beams, influence of shear on bending deformation is taken into account. Moreover, if the value of the small effect scale rises, the critical buckling loads decrease.

The results are compared to other studies found in the literature which led to the conclusion that a great deal of similarity exists between them, which additionally proves the accuracy of this method. Moreover, this method allows calculation with non-rigid boundary conditions. It is this reason that makes this study a significant contribution with a potential to pave the way for further and more advanced studies on this topic.

References

[1] Eringen, A. C., Nonlocal polar elastic continua, *International journal of engineering science*. 10, 1-16, 1972.
[2] Eringen A. C. and Edelen D. G. B., On nonlocal elasticity. *Int. J. Eng. Sci*, 10, 233–48, 1972.
[3] Eringen A. C., On differential equations of nonlocal elasticity and solutions of screw dislocation and surface waves, *J. Appl. Phys*. 54, 4703–4710, 1983.
[4] Li, C. Y., Chou T. W., A structural mechanics approach for the analysis of carbon nanotubes, *Int. J. Solids Struct*. 40, 2487-2499, 2003.
[5] Chowdhury, R., Adhikari, S., Wang, C. W., Scarpa, F., A molecular mechanics approach for the vibration of single walled carbon nanotubes. *Comput. Mater. Sci*., 48, 730-735, 2010.
[6] Poncharal, P., Wang, Z. L., Ugarte, D., Heer, W. A. D., Electrostatic deflections and electromechanical resonances of carbon nanotubes. *Science*, 283, 1513-1516, 1999.
[7] Wang, C. M., Zhang, Y. Y., Ramesh, S. S., Kitipornchai, S., Buckling analysis of micro-and nano-rods/tubes based on nonlocal Timoshenko beam theory. *Journal of Physics D: Applied Physics*, 17, 3904-3909, 2006.
[8] Ghannadpour, S. A. M., and Mohammadi, B., Buckling analysis of micro-and nano-rods/tubes based on nonlocal Timoshenko beam theory using Chebyshev polynomials. *Advanced Materials Research*, 123, 619-622, 2010.
[9] Yayli M. Ö., Buckling Analysis of a Rotationally Restrained Single Walled Carbon Nanotube Embedded In An Elastic Medium Using Nonlocal Elasticity. *Int J Eng Appl Sci*, 8(2), 40-50, 2016. [10] Yayli M. Ö., An Analytical Solution for Free Vibrations of A Cantilever Nanobeam with A Spring Mass System. *Int J Eng Appl Sci*, 7(4), 10-18, 2016.
[11] Civalek, Ö., Akgöz, B., Free vibration analysis of microtubules as cytoskeleton components: nonlocal Euler–Bernoulli beam modeling. *Sci. Iranica Trans. B: Mech. Eng.*, 17, 367-375, 2010.
[12] Civalek, Ö., Demir, Ç., Bending analysis of microtubules using nonlocal Euler–Bernoulli beam theory. *Appl. Math. Model.*, 35, 2053-2067, 2011.
[13] Wang, C.M., Kitipornchai, S., Lim, C.W., Eisenberger, M., Beam bending solutions based on nonlocal Timoshenko beam theory. *J. Eng. Mech.*, 134, 475-481, 2008.
[14] Lu, P., Lee, H.P., Lu, C., Zhang, P.Q., Dynamic properties of flexural beams using a nonlocal elasticity model. *J. Appl. Phys.*, 99, 73510-73518, 2006.

[15] Murmu, T., Pradhan, S.C., Small-scale effect on the vibration of nonuniform nanocantilever based on nonlocal elasticity theory. *Physica E*, 41, 1451-1456, 2009.
[16] Rahmani, O., Pedram, O., Analysis and modeling the size effect on vibration of functionally graded nanobeams based on nonlocal Timoshenko beam theory. *Int. J. Eng. Sci*, 77, 55-70, 2014.
[17] Eltaher, M.A., Emam, S.A., Mahmoud, F.F., Static and stability analysis of nonlocal functionally graded nanobeams. *Compos. Struct*, 96, 82-88, 2013
[18] Thai, H.T., A nonlocal beam theory for bending, buckling, and vibration of nanobeams. *Int. J. Eng. Sci.*, 52, 56-64, 2012.
[19] Reddy J. N., Pang, S. D., Nonlocal continuum theories of beam for the analysis of carbon nanotubes. *Journal of Applied Physics*, 103, 1-16, 2008.
[20] Setoodeh, A.R., Khosrownejad, M., Malekzadeh, P., Exact nonlocal solution for post buckling of single-walled carbon nanotubes. *Physica E*, 43, 1730-1737, 2011
[21] Yayli, M.Ö., Buckling Analysis of a Rotationally Restrained Single Walled Carbon Nanotube. *Acta Physica Polonica A*, 127, 3, 678-683, 2015.
[22] Yayli, M.Ö., Stability analysis of gradient elastic microbeams with arbitrary boundary conditions. *Journal of Mechanical Science and Technology*, 29, 8, 3373-3380, 2015.
[23] Artan R., Tepe A., The initial values method for buckling of nonlocal bars with application in nanotechnology. *European Journal of Mechanics-A/Solids*, 27, (3), 469-477, 2008.
[24] Demir, Ç., Civalek, Ö., Nonlocal finite element formulation for vibration. *International Journal of Engineering and Applied Sciences,* 8(2), 109-117, 2016.
[25] Demir, Ç., Civalek, Ö., On the analysis of microbeams. *International Journal of Engineering Science*, 121(Supplement C), 14-33, 2017.
[26] Demir, Ç., Civalek, Ö., Nonlocal deflection of microtubules under point load. *International Journal of Engineering and Applied Sciences*, 7(3), 33-39, 2015
[27] Akgoz, B., Civalek, Ö., Buckling analysis of linearly tapered micro-columns based on strain gradient elasticity. *Structural Engineering and Mechanics,* 48(2), 195-205, 2013.
[28] Akgöz, B., Civalek, Ö., Bending analysis of embedded carbon nanotubes resting on an elastic foundation using strain gradient theory. *Acta Astronautica* 119, 1-12, 2016.
[29] Civalek, Ö., Demir Ç., A simple mathematical model of microtubules surrounded by an elastic matrix by nonlocal finite element method. *Applied Mathematics and Computation* 289, 335-352, 2016.
[30] Mercan, K., Civalek, Ö., DSC method for buckling analysis of boron nitride nanotube (BNNT) surrounded by an elastic matrix. *Composite Structures* 143, 300-309, 2016.
[31] Civalek, Ö., Analysis of thick rectangular plates with symmetric cross-ply laminates based on first-order shear deformation theory. *Journal of Composite Materials* 42(26), 2853-2867, 2008.
[32] Yayli, M.Ö., On the axial vibration of carbon nanotubes with different boundary conditions. *Micro & Nano Letters* 9(11), 807-811, 2014.
[33] Yayli, M.Ö., Torsion of nonlocal bars with equilateral triangle cross sections. *Journal of Computational and Theoretical Nanoscience* 10(2), 376-379, 2013.
[34] Yayli, M.Ö., Weak formulation of finite element method for nonlocal beams using additional boundary conditions. *Journal of Computational and Theoretical Nanoscience* 8(11), 2173-2180, 2011.
[35] Yayli, M.Ö., Çerçevik A. E., 1725. Axial vibration analysis of cracked nanorods with arbitrary boundary conditions. *Journal of Vibroengineering* 17(6), 2907-2921, 2015.
[36] Yayli, M.Ö., Airy Stress Functions for Transverse Sinusoidally Loaded Beam in Nonlocal Elasticity. *Journal of Computational and Theoretical Nanoscience* 8(10), 2006-2012, 2011.

International Journal of Engineering & Applied Sciences (IJEAS)
Vol.9, Issue 4 (2017) 100-105
http://dx.doi.org/10.24107/ijeas.366441
Int J Eng Appl Sci 9(4) (2017) 100-105

Effects of Barite Sand Addition on Glass Fiber Reinforced Concrete Mechanical Behavior

Sadık Alper Yıldızel

Karamanoglu Mehmetbey University, Engineering Faculty, Civil Engineering Department
**E-mail address*: sayildizel@kmu.edu.tr

ORCID numbers of authors:
0000-0001-5702-807X

Received date: December 2017
Accepted date: December 2017

Abstract

Glass fiber reinforced concrete (GFRC) is a cementitious composite reinforced by the addition of alkali-resistant glass fibers. GFRC is widely used for various types of precast products in civil engineering industries. GRFC mixes generally include silica sand to produce precast concrete elements; however, silica sand was replaced with barite sand at the ratios of 5%, 10 % and 15 % of wt. in order to reveal its applicability and potential for different engineering purposes. The flexural strength and the freeze-thaw(F&T) resistance of the composites were studied. The experimental results showed that the replacement of silica sand with barite sand up to 15 % of wt. enhances the mechanical properties of the composites in respect to flexural strength and F&T resistance properties.

Keywords: Glass fiber, silica sand, barite sand, silica sand replacement, glass fiber reinforced concrete.

1. Introduction

Fiber addition into the matrix significantly enhances the mechanical properties of the concretes. Engineering properties of the concrete such as flexural strength, toughness, abrasion resistance and impact can be increased with the addition of various types of fibers according to the results of many literature studies [1-3]. Various types of fibers such as basalt, carbon, aramid and glass have been commonly used for reinforcing cementitious matrixes [4, 5].

Some academics reported that glass fiber addition increase the flexural and splitting tensile strength of the composites up to 20 %. Flexural toughness and shear toughness properties can also be increased by inclusion of a certain amount of fibers as per the results of the studies [6,7].

Barite mineral is commonly used as aggregates for producing heavyweight concrete. Barite aggregate added concrete mixes are generally selected to minimize the effect of radiations such as gamma rays. The addition of this mineral in small quantities can enhance the concrete behavior against the radiation waves compared to the conventional concrete mixes [8,9]. Some researches results showed that addition of barite mineral can not enhance the mechanical properties of the ordinary concrete [10, 11].

Barite mineral is more sensitive to abrasion compared to the other types of aggregates. In addition, due to massive usage of barite minerals for the radiation shielding purposes, it becomes difficult to find coarse graded barite aggregates [12].

In this study, the aim was to investigate the potential usage of barite aggregates as silica sand replacement materials in GFRC applications.

2. Materials and Experimental Details

CEM I type white cement complying the TS EN 197-1 standard was used as a binding material. Some physical and chemical properties of the white cement can be found in Table 1.

Table 1. The chemical and physical properties of CEM I 52.5 R cement

Chemical Properties (%)	SiO_2	21.6	Physical Properties	Specific weight (t/m^3)	3.06
	Al_2O_3	4.05		Specific surface (cm^2/g)	4600
	Fe_2O_3	0.26		Whiteness (%)	85.5
	CaO	65.7		Initial Setting time (min.)	100
	MgO	1.30		Final Setting time (min.)	130
	Na_2O	0.30		Water for standard consistency (%)	30
	K_2O	0.35		Volume constancy (mm)	1
	SO_3	3.30		0.045 Sieve Residue (%)	1
	Free CaO	1.6		0.090 Sieve Residue (%)	0.1
	Chloride (Cl)	0.01		Compressive Strength at 2 days (MPa)	37
	Insoluble	0.18		Compressive Strength at 7 days (MPa)	50
	Loss on Ignition	3.20		Compressive Strength at 28 days (MPa)	60

Silica sand and barite mineral were selected as aggregates. Particle size distribution of silica sand is given in Fig. 1. And chemical and mineralogical properties of the aggregates can be found in Table 2.

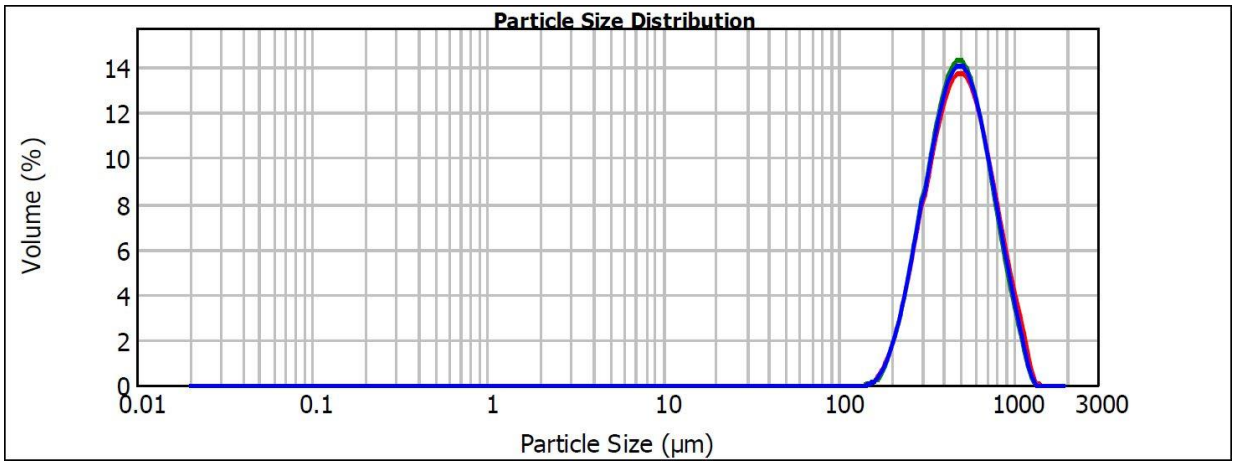

Fig.1. Silica sand particle size distribution

Table 2. Aggregates chemical and mineralogical properties

Chemical and mineralogical composition							
	SiO_2	Fe_2O_3	MgO	CaO	K_2O	Na_2O	Al_2O_3
Silica sand	98.60	0.13	0.03	0.01	0.09	0.02	1.12
Barite	0.4	0.06	0.10	0.36	-	-	-

Polycarboxylate based plasticizer was used as the chemical agent. The water used during the experimental works was potable. Alkali resistant glass fibers were chosen as reinforcing fiber material, and mechanical and physical properties of the glass fiber are given in Table 3. Fiber ratio was kept constant as 3 % of wt. Mix proportions of the composite can be found in Table 4.

Table 3. Physical and mechanical properties of the alkali resistant glass fibers

Mechanical and physical properties of the glass fibers	
Ultimate strength, bending (MOR, MPa)	20-28
Elastic limit, bending (LOP, MPa)	7-11
Ultimate strength, tensile (MOR, MPa)	8-11
Elastic limit, tensile (LOP, MPa)	5-7
Compressive Strength (Mpa)	50-80
Elastic Modulus (GPa)	10-20
Dry density t/m^3	1.9-2.1

Table 4. Experimental sets

Mixture Code	Silica Sand(kg)	Barite Sand (kg)	Fiber ratio	White cement (kg)	W/C	Superplasticizer (kg)
R_1	50	0	3 %	50	0.34	0.50
M_1	47.5	2.5		50	0.34	0.52
M_2	45	5		50	0.34	0.55
M_3	42.5	7.5		50	0.34	0.58

The reference mix was composed of silica sand, white cement, glass fiber and superplasticizer. The specimens with the dimensions of 160 x 40 x 40 mm were made for the mechanical tests. Flexural strength tests were conducted with four-point bending test machine. All specimens were kept under the laboratory conditions for 24 hours. Flexural strength tests were conducted as per the requirements of TS EN 1170-4,5. F&T resistance of the specimens were determined in comply with the ASTM C 666 standard.

3. Results and Discussions

Flexural test results at 7, 15 and 28 days are given in Fig. 2. Flexural test results showed that strength values enhance with the increasing barite sand content.

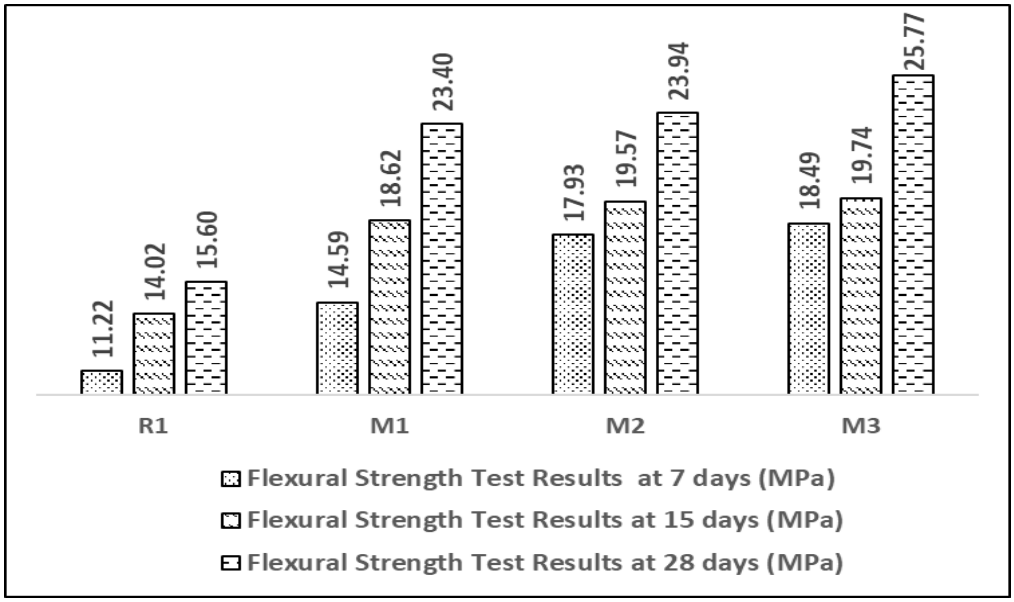

Fig.2. Flexural strength test results

Maximum flexural strength value was recorded as 25.77 MPa at 28 days and it was belonged the mixture M_3. Silica sand replacement with the barite sand at the ratios of 15 % of wt. significantly increased the strength values of the specimens.

The strength test results and strength losses of the composites can be found in Fig. 3. Barite added mixes have lower strength loss values compared to the reference mix. The minimum strength loss value after F&T cycles was obtained as 22.27 % belonged to the M_3 mix. Decrease in strength losses may be attributed to the increased durability of the mixes with the increasing barite content.

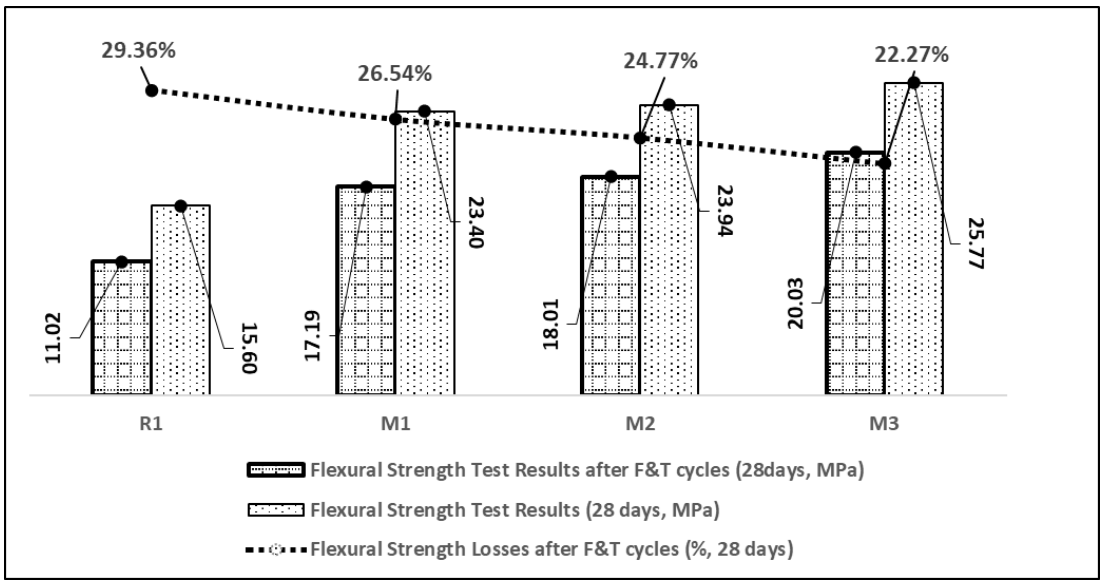

Fig.3. Flexural strength losses after F-T cycles

4. Conclusions

The effects of barite addition to glass fiber reinforced concrete were studied within the scope of this experimental research. A good synergy between the barite aggregate addition and conventional GFRC composition was obtained with the light of the results of the tests. The main findings can be summarized as follows:

- The increase in barite aggregate content in GFRC composites increases the flexural strength values.
- In replacement of 15 % of wt. silica sand with barite aggregates showed the best performances both for the flexural strength and F&T test results.
- Barite aggregates can be used in GFRC mixes for specific purposes such as radiation protection.
- As the amount of barite increased in GFRC, the durability property was also increased according to the F&T test results. Strength losses of the composites can be limited against the F&T effects with the addition of barite aggregates.
- Future studies should be conducted on possible aging effects.

References

[1] Yoo, D.-Y., Lee, J.-H., Yoon, Y.-S., Effect of fiber content on mechanical and fracture properties of ultra high performance fiber reinforced cementitious composites, *Composite Structures*, 106, 742–53, 2013.

[2] Yoo, D.Y., Yoon, Y.S., Banthia, N., Predicting the post-cracking behavior of normal- and high-strength steel-fiber-reinforced concrete beams, *Construction and Building Materials*, 93, 477–85, 2015.

[3] Wittmann, F.H., Rokugo, K., Brühwiler, E., Mihashi, H., Simonin, P., Fracture energy and strain softening of concrete as determined by means of compact tension specimens, Materials and Structures, 21, 21–32, 1988.

[4] Newman, J., Choo, B.S., Advanced Concrete Technology, Butterworth-Heinemann, 1st edition, 2003.

[5] Kizilkanat, A.B., Kabay, N., Akyüncü, V., Chowdhury, S., Akça, A.H., Mechanical properties and fracture behavior of basalt and glass fiber reinforced concrete: An experimental study, *Construction and Building Materials*, 100, 218–24, 2015.

[6] Tassew, S.T., Lubell, A.S., Mechanical properties of glass fiber reinforced ceramic concrete, *Construction and Building Materials*, 51, 215–24, 2014.

[7] Chandramouli, K., Rao S.S., Pannirselvam, N., Sekhar, S.T., Sravana, P., Strength Properties of Glass Fibre Concrete, *Journal of Engineering and Applied Sciences*, 5, 1–6, 2010.

[8] Bashter, I.I., Calculation of radiation attenuation coefficients for shielding concretes, *Annals of Nuclear Energy*, 24, 1389–401, 1997.

[9] Akkurt, I., Basyigit, C., Kilincarslan, S., Mavi, B., Akkurt, A., Radiation shielding of concretes containing different aggregates, *Cement and Concrete Composites*, 28, 153–7, 2006.

[10] Sakr, K., El-Hakim, E., Effect of high temperature or fire on heavy weight concrete properties, *Cement and Concrete Research*, 35, 590–6, 2005.

[11] Kilincarslan, S., Akkurt, I., Basyigit, C., The effect of barite rate on some physical and mechanical properties of concrete, *Materials Science and Engineering A*, 424, 83–6, 2006.

[12] Saidani, K., Ajam, L., Ben Ouezdou, M., Barite powder as sand substitution in concrete: Effect on some mechanical properties, *Construction and Building Materials*, 95, 287–95, 2015.

International Journal of Engineering & Applied Sciences (IJEAS)
Vol.9, Issue 4 (2017) 106-114
http://dx.doi.org/10.24107/ijeas.368922
Int J Eng Appl Sci 9(4) (2017) 106-114

Prediction of Significant Wave Height along Konyaaltı Coast

Rifat Tur [a], Dilayda Soylu Pekpostalci [b], Özen Arlı Küçükosmanoğlu [c], Alp Küçükosmanoğlu [d]*

[a,b] Akdeniz University, Engineering Faculty, Antalya-TURKIYE
[c,d] Mehmet Akif Ersoy University, Engineering-Architecture Faculty, Burdur-TURKIYE
[*]E-mail address: alpkosmo@gmail.com

ORCID numbers of authors:
0000-0003-3008-8480[a], 0000-0001-6140-0399[b], 0000-0002-2119-8074[c], 0000-0002-7551-1513[d]

Received date: December 2017
Accepted date: December 2017

Abstract

Prediction of wave parameters is important for the planning, designing, construction and maintenance of coastal structures. In this study, significant wave heights (H_s) for Konyaaltı coast, located in Antalya at Mediterranean Sea coastline of Turkey is predicted. Significant wave height estimation is performed based on the wind data set which is obtained from The European Centre for Medium-Range Weather Forecasts (ECMWF) and Turkish State Meteorological Service (TSMS) by numerical and parametric methods in literature including WAM, CEM, Wilson and SMB method. While 13 years of wind data obtained from ECMWF is used for WAM and CEM method, 30 years of wind data provided from TSMS is used for SMB and Wilson method. The accuracy of these methods is investigated by comparing the Gumbel distribution results with Wind and Deep Water Wave Atlas for Turkish Coast for Konyaaltı Coast. Consequently, CEM method provides more consistent results for the study area compare to other significant wave height prediction methods.

Keywords: Wave hindcasting, Significant wave height, SMB, Wilson, CEM, WAM

1. Introduction

Significant wave height which has an important role in coastal activities such as planning, designing of coastal structures, sediment transport and coastal erosion can be predicted by different methods including artificial intelligence techniques, numerical models, parametric methods etc. [1-8]. There are many studies in literature related to significant wave height estimation. While Duan et al. (2016) use a hybrid Empirical Model Decomposition (EMD) Support Vector Regression (SVR) model for short term, Altunkaynak (2015) uses spatial function for significant wave height prediction [9, 10]. Classification and regression trees are used by Mahjoobi and Etemad-Shahidi, an enhanced Takagi-Sugeno-based fuzzy methodology is used by Hashim et al., and also genetic algorithm is used by Elbisy [11-13]. Moreover, while Wang proposes transformed linear simulation method, Rusu and Raileanu uses a wave modelling system based on the simulating waves nearshore for significant wave height prediction [14, 15].

Wind wave characteristic is necessary for wave hindcasting. Since numerical modelling which solves the energy balance equation along the area where active wave generation occurs requires the bathymetric, meteorological and oceanographic data. Since numerical modelling is expensive and difficult in the absence of these data , several simplified methods including SMB (Sverdrup, Munk and Bretschneider) (Bretschneider 1970), Wilson (Wilson 1965), JONSWAP (Haselman et al. 1973),

Donelan (Donelan 1980), SPM (Shore Protection Manual) (U.S. Army 1984), CEM (Coastal Engineering Manual) (U.S. Army 2006) are used [16].

The studies on significant wave height estimation by parametric models including Wilson, SPM, JONSWAP, and CEM for the south of Black Sea indicate that although CEM method provides better results than the others, parametric methods are unable to provide sufficient result. However, ANFIS models provide more accurate results than the parametric methods [17, 18]. Dubey and Das (2013) indicates that after significant wave height for Indian Coast is estimated by CEM and Wilson method the extreme wave analysis is done by Gumbel, Weibull and log-normal distribution methods [19]. Balas et al. (2013) present significant wave height prediction by CEM method and Gumbel distribution for Edremit, Balıkesir by use of HYDROTAM-3D [20]. Etemad-Shahidi et al. compare the results of CEM, Wilson and SMB methods with the measured wave heights for Great Lakes and investigate the accuracy of each model for different conditions [16].

The aim of this study is to compare extreme value analysis with Gumbel distribution obtained from four different significant wave height prediction methods including WAM (A third generation ocean wave prediction model), CEM, Wilson and SMB methods.

2. Material and Methods

2.1. Study Area and Dataset Description

The data set for Konyaaltı coast, located in Antalya at Mediterranean Sea coastline of Turkey at 30.70°E 36.84°N, 30.66°E (Fig. 1) is obtained from both ECMWF and Turkish State Meteorological Service.

Fig. 1. Location of study area

Approximately 30 years of hourly wind data acquired from Turkish State Meteorological Service. The data set is composed of station 17300 (from June, 1981 to December, 2006) and station 17302 wind data (from January, 2012 to March, 2016). 13 years of 6 hourly wind data (from 2000 to 2013) is obtained from ECMWF. While 13 years of ECMWF wind data is used for WAM and CEM method, 30 years of wind data provided from TSMS is used for SMB and Wilson method.

2.2. Methodology

While WAM model is numerical, the other methods are parametric methods. All methods can be used for wave hindcast or forecast. Also the comparative results obtained from WAM, CEM, Wilson and SMB methods are presented.

First of all, fetch length and wind duration are needed to determine whether the fully developed state occurs or not. If wind transfers maximum energy to wave, then fully developed sea condition occurs. Otherwise, duration limited condition occurs when wind duration is smaller than t_{min} or fetch limited condition occurs when fetch length is smaller than F_{min}. Since fetch or duration is inadequate to that wind is able to impart maximum energy to wave, sea is non-fully developed state for both duration and fetch limited condition.

The effective fetch length (F_{eff}) which is commonly used in literature is determined according to the location of study area. For each wind direction, fetch lengths (F_i) are measured extend over 45º range either side of wind direction for each 7,5º interval (α_i). By this way, measured 12 fetch lengths and 12 angles for the wind direction are used to calculate effective fetch length [21] :

$$F_{eff} = \frac{\sum F_i \cos^2 \alpha_i}{\sum \cos \alpha_i} \tag{1}$$

Since wind velocity higher than 3m/s is considered for Wilson and SMB method, wind duration is determined according to duration of wind blowing that velocity of wind is higher than 3m/s. And wind speed at 10 m above the sea (U_{10}) is used for the methods presented in the following parts. If wind speed is observed at any elevation up to 20 m Eq. (2) can be used [22]:

$$U_{10} = U_z \left(\frac{10}{z} \right)^{\frac{1}{7}} \tag{2}$$

Additionally, stability correction due to the air-sea temperature difference Eq. (3) and location effect due to surface roughness Eq. (4) proposed by Resio and Vincent (1977) can be used where needed [22]:

$$U = R_T U(10) \tag{3}$$

$$U_w = R_L U_L \tag{4}$$

After gathering the U_{10} values, significant wave heights are calculated. First of all, it should be determined that the case is fetch limited, duration limited or fully developed. So significant wave height are calculated according to formulation that differs in these cases. Since results obtained from SMB, Wilson, CEM, and WAM methods indicate the extreme value analysis for Konyaaltı coast, the comparative results are shown by Gumbel distribution for each method.

2.2.1. SMB

If wind duration is greater than t_{min} , H_s is calculated by Eq. (5) in case fetch limited condition. Otherwise, case is duration limited and Eq. (6) is used to find corresponding fetch for duration limited cases, and then H_s is calculated by Eq. (6).

$$\frac{gH_s}{U_{10}^2} = 0,283\tanh\left(0,0125\left(\frac{gF}{U_{10}^2}\right)^{0,42}\right) \tag{5}$$

$$\frac{gt_{\min}}{U_{10}} = 6,5882\exp\left\{\left[0,0161\left(\ln\left(\frac{gF}{U_{10}{}^2}\right)\right)^2 - 0,3692\left(\ln\left(\frac{gF}{U_{10}{}^2}\right)\right) + 2,2024\right]^{0,5} + 0,8798\left(\ln\left(\frac{gF}{U^2}\right)\right)\right\} \tag{6}$$

where g is acceleration due to gravity (m/s^2), F is the fetch length (m), U_{10} is the wind speed at 10 m above the sea surface (m/s), t_{min} is the minimum duration (hr),

2.2.2. Wilson

In this method, minimum duration (t_{min}, hr) and minimum fetch length (F_{min}, km) are calculated by the Eq. (7) and Eq. (8):

$$t_{\min} = 1,0F^{0,73}U_{10}^{-0,46} \tag{7}$$

$$F_{\min} = 1,0t^{1,37}U_{10}^{0,63} \tag{8}$$

where, F is the fetch length (km), U_{10} is the wind speed at 10 m above the sea surface (m/s), t is wind duration (hr).

The significant wave height is calculated by Eq. (9) in the fetch limited condition:

$$\frac{gH_s}{U_{10}^2} = 0,30\left[1-\left[1+0,004\left(\frac{gF}{U_{10}^2}\right)^{0,5}\right]^{-2}\right] \tag{9}$$

where g is acceleration due to gravity (m/s^2).

Otherwise, in the duration limited condition significant wave height is calculated with equivalent fetch which is defined by replacing t_{min} by t in Eq. (7)

2.2.3. CEM

In the CEM method [23] the minimum wind duration (t_{min} , s) formulation is expressed by Eq. (10):

$$t_{\min} = 77,23\frac{F^{0,67}}{U_{10}^{0,34}g^{0,33}} \tag{10}$$

where F is the fetch length (m), U_{10} is the wind velocity above 10 m from the sea surface (m/s), g is the acceleration of gravity (m/s^2).

For fetch limited condition H_s is calculated by Eq. (11):

$$\frac{gH_s}{u_*^2} = 4,13\times10^{-2}\left(\frac{gF}{u_*^2}\right)^{0,5} \tag{11}$$

where u_* is the friction velocity (m/s) estimated by Eq. (12):

$$u_* = U_{10}(C_D)^{0,5} \tag{12}$$

where, C_D is the drag coefficient which is calculated by Eq. 13

$$C_D = 0,001(1,1+0,035U_{10}) \tag{13}$$

In duration limited condition equivalent fetch length is calculated by:

$$\frac{gF}{U_*^2} = 5,23\times10^{-3}\left(\frac{gt}{U_*}\right)^{1,5} \tag{14}$$

2.2.4. WAM

WAM which is a third generation wave model is presented by The Wave Model Development and Implementation Group (WAMDI Group); is the first model that solves the energy balance equation, including non-linear wave interactions [23-25]. Wave forecast with WAM model is proceeded as follows [24]:

Evolution equation for action density *N(k)* is presented by Eq. (15):

$$F(k) = \sigma N(k) \tag{15}$$

where *F(k)* is wave number spectrum, *k* is the wave number and σ is calculated by Eq. (16):

$$\sigma = \sqrt{gk \tanh kD} \tag{16}$$

where *D* is the water depth and *g* is the acceleration of gravity,.

Wave number spectrum is normalized with Eq. (17):

$$\int dkF(k) = \left\langle \eta^2 \right\rangle = m_0 \tag{17}$$

where η is the surface elevation and m_0 is the wave variance.

Significant wave height is calculated by Eq. (18):

$$H_s = 4\sqrt{\left\langle \eta^2 \right\rangle} \tag{18}$$

The frequency spectrum is defined as:

$$F_2(\omega,\theta)d\omega d\theta = F(k)dk = F(k,\theta)kdkd\theta \tag{19}$$

where θ is the wave direction.

The one dimensional frequency spectrum is defined by Eq. (20):

$$F_1(\omega) = \int d\omega F_2(\omega,\theta) \tag{20}$$

For fully developed waves Eq. (21) is used:

$$g^3F(\omega)/U_{10}^5 = f(\omega U_{10}/g) \tag{21}$$

For fetch limited conditions Eq. (22) is used:

$$g^3F(\omega)/U_0^5 = f(\omega U_{10}/g, gF/U_{10}^2) \tag{22}$$

where *F* is the fetch length.

3. Application and Results

Parametric methods SMB, Wilson, CEM and numerical method WAM are used to predict significant wave height for Konyaaltı Coast. While 30 years of hourly wind data provided from TSMS is used for SMB and Wilson method, 13 years of 6 hourly ECMWF wind data is used for WAM and CEM methods. Table 1 indicates the significant wave heights (m/s) corresponding to return period (year) for each method.

Table 1. Significant Wave Heights (m/s)

T_r (year)	5	10	20	50	100
SMB	3,6	4,24	4,86	5,66	6,26
GODA	1,98	2,37	2,74	3,23	3,59
CEM	4,57	5,23	5,86	6,67	7,28
WAM	3,26	3,67	4,06	4,57	4,95

Gumbel distribution for each model is presented in Fig. 2 in order to indicate the comparative results. Gumbel distribution for Konyaaltı Coast (36.75ºN, 30.70°E) obtained from Wind and Deep Water Wave Atlas for Turkish Coast[26] is also presented to investigate the performance of the models (Fig. 2). "q" in Fig. 2 which indicates the non-exceedance probability of significant wave height is calculated by Eq. (23).

$$q = 1 - \frac{1}{T_r} \tag{23}$$

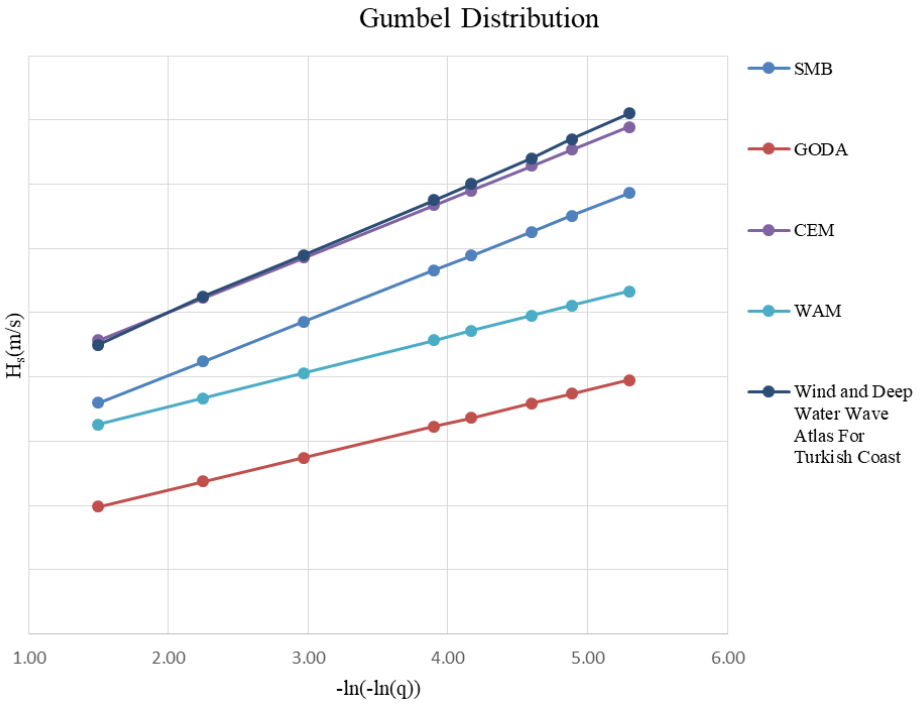

Fig. 2. Gumbel Distribution

The results of CEM method and Wind and Deep Water Wave Atlas for Turkish Coast are closer compare to other methods. It can be easily seen that CEM method provides more consistent result with of Wind and Deep Water Wave Atlas for Turkish Coast for study area.

4. Conclusions

This study indicates the significant wave height prediction results of parametric and numerical methods including SMB, Wilson, CEM, and WAM. After significant wave heights are predicted, extreme value analysis with Gumbel distribution is done for each method. Gumbel distributions are presented in the same graph (Fig. 2) in order to examine similarities between results. Gumbel distribution of Wind and Deep Water Wave Atlas for Turkish Coast for Konyaaltı Coast is given to investigate the performance of methods used. Consequently, CEM method provides more consistent results with Wind and Deep Water Wave Atlas for Turkish Coast for study area as compared to the other significant wave height prediction methods. Also, 13 years of wind data gives higher significant wave height values compared to 30 years of wind data considering the gumbel distributions of these data sets. This situation can be result from climate change.

References

[1] Berbic, J., Ocvirk, E., Carevic, D., Loncar, G., Application of neural networks and support vector machine for significant wave height prediction. *Oceanologia*, 59(3), 331-349, 2017.

[2] Cornejo-Bueno, L., Borge, J.C.N., Alexandre, E., Hessner, K., Salcedo-Sanz, S., Accurate estimation of significant wave height with Support Vector Regression algorithms and marine radar images. *Coastal Engineering*, 114, 233-243, 2016.

[3] Cornejo-Bueno, L., Nieto-Borge, J.C., Garcia-Diaz, P., Rodriguez, G., Salcedo-Sanz, S., Significant wave height and energy flux prediction for marine energy applications: A grouping genetic algorithm - Extreme Learning Machine approach. *Renewable Energy*, 97, 380-389, 2016.

[4] Orimolade, A.P., Haver, S., Gudmestad, O.T., Estimation of extreme significant wave heights and the associated uncertainties: A case study using NORA10 hindcast data for the Barents Sea. *Marine Structures*, 49, 1-17, 2016.

[5] Shukla, R.P., Kinter, J.L., Subseasonal Prediction of Significant Wave Heights over the Western Pacific and Indian Ocean Region. *Weather and Forecasting*, 31(6), 1733-1751, 2016.

[6] Tür, R., Belirgin Dalga Yüksekliğinin (Significant Wave Height=H_s) Bulanık Sinir Ağları (ANFIS) ile Tahmini. *The Journal of Graduate School of Natural and Applied Sciences of Mehmet Akif Ersoy University* 7(2), 175-183, 2016.

[7] Yu, T.T., Xie, W.S., Zhang, S.O., Improved algorithm for estimation of significant wave height from X-band radar image sequences. *Journal of Applied Remote Sensing*, 10, 2016.

[8] Zhang, S., Song, Z.J., Lie, Y., An advanced inversion algorithm for significant wave height estimation based on random field. *Ocean Engineering*, 127, 298-304, 2016.

[9] Altunkaynak, A., Prediction of significant wave height using spatial function. *Ocean Engineering*, 106, 220-226, 2015.

[10] Duan, W.Y., Han, Y., Huang, L.M., Zhao, B.B., Wang, M.H., A hybrid EMD-SVR model for the short-term prediction of significant wave height. *Ocean Engineering*, 124, 54-73, 2016.

[11] Elbisy, M.S., Sea Wave Parameters Prediction by Support Vector Machine Using a Genetic Algorithm. *Journal of Coastal Research*, 314, 892-899, 2015.

[12] Hashim, R., Roy, C., Motamedi, S., Shamshirband, S., Petković, D., Selection of climatic parameters affecting wave height prediction using an enhanced Takagi-Sugeno-based fuzzy methodology. *Renewable and Sustainable Energy Reviews*, 60, 246-257, 2016.

[13] Mahjoobi, J., Etemad-Shahidi, A., An alternative approach for the prediction of significant wave heights based on classification and regression trees. *Applied Ocean Research*, 30(3), 172-177, 2008.

[14] Rusu, E., Raileanu, A., A multi-parameter data-assimilation approach for wave prediction in coastal areas. *Journal of Operational Oceanography*, 9(1), 13-25, 2016.
[15] Wang, Y.-g., Prediction of height and period joint distributions for stochastic ocean waves. *China Ocean Engineering*, 31(3), 291-298, 2017.
[16] Etemad-Shahidi, A., Kzeminezhad, M.H., Mousavi, S.J. On The Prediction of Wave Parameters Using Simplified Methods.*Journal of Coastal Research*, Portugal, 2009.
[17] Akpınar, A., Özger, M., Kömürcü, M.İ., Prediction of wave parameters by using fuzzy inference system and the parametric models along the south coasts of the Black Sea. *Journal of Marine Science and Technology*, 19(1), 1-14, 2014.
[18] Akpinar, A., Özger, M., Bekiroglu, S., Komurcu, M.I., Performance Evaluation of Parametric Models in The Hindcasting of Wave Parameters Along The South Coast of Black Sea. *Indian Journa og Geo-MArine Sciences*, 43(6), 905-920, 2014.
[19] Dubey, R.P., Das, B., Long Term Ocean Wave Forecasting Along Indian Coast *Journal of Indian Water Resources Society*, 33(2), 24-29, 2013.
[20] Balas, L., Numanoğlu Genç, A., İnan, A., Liman yapılarının tasarımı için dalga tahmini. *Dokuz Eylül Üniversitesi Denizcilik Fakültesi Dergisi*, 5(2), 2013.
[21] Yüksel, Y., Özkan Çevik, E., *Kıyı Mühendisliği*, 1 ed, Deniz Mühendisliği Serisi - No12009, İstanbul; Beta basım yayım,2009.
[22] *Shore Protectin Manual (SPM)*1984, U. S. Army Corps of Engineers, Washington, DC: U.S. Army Engineer Waterways Experiment Station, U.S.; U. S. Government Printing Office,1984.
[23] *Coastal Engineering Manual*. U. S. Army Corps of Engineers, U.S., 2006.
[24] Janssen, P., The Wave Model. *Meteorological Training Course Lecture Series*, 2003.
[25] The WAMDI Group, The WAM Model - A third Generation Ocean Wave Prediction Model. *Journal of Physical Oceanography*, 18, 1775-1810, 1988.
[26] Özhan, E., Abdalla S., *Türkiye kıyıları rüzgar ve derin deniz dalga atlası*, MEDCOAST, METU, 445,2002.